ÇUKUROVA UNIVERSITY
INSTITUTE OF NATURAL AND APPLIED SCIENCES

PhD THESIS

Özgür ÇELİK

CONTROLLER DESIGN AND EXPERIMENTAL VERIFICATION OF GRID-CONNECTED MICROINVERTERS FOR PHOTOVOLTAIC APPLICATIONS

DEPARTMENT OF ELECTRICAL AND ELECTRONICS ENGINEERING

ADANA-2019

ÇUKUROVA UNIVERSITY
INSTITUTE OF NATURAL AND APPLIED SCIENCES

CONTROLLER DESIGN AND EXPERIMENTAL VERIFICATION OF GRID-CONNECTED MICROINVERTERS FOR PHOTOVOLTAIC APPLICATIONS

Özgür ÇELİK

PhD THESIS

DEPARTMENT OF ELECTRICAL AND ELECTRONICS ENGINEERING

We certify that the thesis titled above was reviewed and approved for the award of degree of the Doctor of Philosophy by the board of jury on 27/11/2019.

…………………………….	…………..…………………....	…………………….………..........
Assoc. Prof. Dr. Ahmet TEKE	Assoc. Prof. Dr. Turgay İBRİKÇİ	Assoc. Prof. Dr. Lütfü SARIBULUT
SUPERVISOR	MEMBER	MEMBER
…………………………	…………………………………	
Asst. Prof. Dr. Adnan TAN	Asst. Prof. Dr. Necdet Sinan ÖZBEK	
MEMBER	MEMBER	

This PhD Thesis is written at the Department of Electrical and Electronics Engineering of Institute of Natural and Applied Sciences of Çukurova University.
Registration Number:

Prof. Dr. Mustafa GÖK
Director
Institute of Natural and Applied Sciences

This thesis was supported by the Scientific Research Project Unit of Çukurova University (Project Number: FDK-2017-9136). This thesis was also supported by TÜBİTAK (Project Number: EEEAG-118E940).

ABSTRACT

PhD THESIS

CONTROLLER DESIGN AND EXPERIMENTAL VERIFICATION OF GRID-CONNECTED MICROINVERTERS FOR PHOTOVOLTAIC APPLICATIONS

Özgür ÇELİK

ÇUKUROVA UNIVERSITY
INSTITUTE OF NATURAL AND APPLIED SCIENCES
DEPARTMENT OF ELECTRICAL AND ELECTRONICS ENGINEERING

Supervisor : Assoc. Prof. Dr. Ahmet TEKE
Year: 2019, Pages: 167
Jury : Assoc. Prof. Dr. Ahmet TEKE
: Assoc. Prof. Dr. Turgay İBRİKÇİ
: Assoc. Prof. Dr. Lütfü SARIBULUT
: Asst. Prof. Dr. Adnan TAN
: Asst. Prof. Dr. Necdet Sinan ÖZBEK

Micro-inverters are module integrated forms of photovoltaic converters that have attracted much attention in recent years. The design considerations of micro-inverters substantially concentrate on providing performance requirements of photovoltaic converters and grid standards. The key objective of this thesis is to optimize the controller performance of the micro-inverter to ensure better system reliability and promote overall efficiency. Toward this goal, a novel maximum power point tracking method is developed to attain maximum power from the photovoltaic modules under both partial shading conditions and rapidly changing atmospheric conditions. Further, dynamic grid support and anti-islanding detection capabilities are assured through the improved controller structure without the use of any extra hardware. The proposed micro-inverter topology and the control algorithms are designed and analyzed through detailed simulation studies using PSCAD/EMTDC. The developed system is implemented experimentally and its performance is verified with extensive case studies. The obtained results indicate that the proposed system provides a promising performance even in low and rapidly changing load conditions. Consequently, the developed micro-inverter can be a considerable candidate for photovoltaic applications in terms of increased dynamic performance and efficiency, reduced output current distortion, meeting grid requirements, and reasonable cost.

Key Words: Photovoltaic, Micro-Inverter, MPPT, Flyback Converter, Grid-Connected Inverter.

ÖZ

DOKTORA TEZİ

FOTOVOLTAİK UYGULAMALAR İÇİN ŞEBEKE BAĞLANTILI MİKROEVİRİCİLERİN KONTROLCÜ TASARIMI VE DENEYSEL DOĞRULANMASI

Özgür ÇELİK

ÇUKUROVA ÜNİVERSİTESİ
FEN BİLİMLERİ ENSTİTÜSÜ
ELEKTRİK – ELEKTRONİK MÜHENDİSLİĞİ ANABİLİM DALI

Danışman : Doç. Dr. Ahmet TEKE
Yıl: 2019, Sayfa: 167
Jüri : Doç. Dr. Ahmet TEKE
: Doç Dr. Turgay İBRİKÇİ
: Doç. Dr. Lütfü SARIBULUT
: Dr. Öğr. Üyesi Adnan TAN
: Dr. Öğr. Üyesi Necdet Sinan ÖZBEK

Son yıllarda oldukça ilgi çeken mikro-eviriciler, fotovoltaik çevirgeçlerin panel bazlı formudur. Mikro-evirici tasarım hususları temel olarak fotovoltaik sistemlerin performans gereksinimlerini ve şebeke standartlarını sağlamaya odaklanmaktadır. Bu tezin temel amacı, daha fazla güvenilirlik sağlamak ve genel verimliliği artırmak için mikro-eviricilerin kontrolcü performansını optimize etmektir. Bu amaca yönelik olarak, kısmi gölgelenme ve hızla değişen atmosferik koşullar altında fotovoltaik panellerden maksimum güç elde etmek için yeni bir maksimum güç noktası izleyici yöntemi geliştirilmiştir. Ayrıca, dinamik şebeke destekleme ve ada modu tespiti yetenekleri herhangi ilave donanım kullanılmadan geliştirilmiş kontrolcü yapısı ile sağlanmıştır. Önerilen topoloji ve kontrolcü algoritmaları PSCAD/EMTDC kullanılarak yapılan detaylı benzetim çalışmaları ile tasarlanmış ve analiz edilmiştir. Geliştirilen sistem deneysel olarak gerçeklenmiş ve performansı kapsamlı vaka çalışmaları ile doğrulanmıştır. Elde edilen sonuçlar, önerilen sistemin düşük ve hızla değişen yük koşullarında bile yeterli performans sağladığını göstermektedir. Sonuç olarak, geliştirilen mikro-evirici, arttırılan dinamik performans ve verimlilik, azaltılan çıkış akımı harmonik bozunumu, şebeke gereksinimlerini karşılama ve maliyet açısından önemli bir aday olabilir.

Anahtar Kelimeler: Fotovoltaik, Mikro-Evirici, MGNİ, Çapraz Çevirici, Şebeke-Bağlantılı Evirici.

EXTENDED SUMMARY

The employment of energy has become a matter of serious interest in recent years due to the expeditious growth of population and industrialization. Fossil fuels based conventional energy sources are filling the gap in rising energy demand, however the depletion of fossil fuels, rising oil prices, environmental issues caused by customary energy resources, climate changes based on global warming, impact of carbon emissions sourced from fossil fuels combustion, and environmental pollution have been motivated people to seek the sustainable energy sources. In this manner, renewable energy sources are often seen as one of the most viable alternatives to fossil fuels in order to tackle these problems. The prominent features of renewable energy sources can be indicated as being sustainable, plentiful, endless and eco-friendly. Solar energy can be considered as a fundamental renewable energy source of the present and future due to being plentiful and sustainable characteristic of the sun.

In the course of the last decades, photovoltaic (PV) technology has been experienced an accelerated improvement. The global cumulative installed PV system capacity marks a prominent growth depending on the technological developments. In respect of globally installed capacity, solar energy is the third most significant renewable energy source following hydro and wind power. PV plants becoming an alternative way of generating electricity, out-competing conventional power generation plants in several parts of the world. PV systems can be implemented in two ways, which are stand-alone and grid-connected. In order to utilize solar energy more efficient, intensive studies have been in progress on the grid-connected PV systems. The PV power generation plants in Europe mostly connected to the utility grid and few of them used as off-grid. In both of these PV systems, the inverters aroused much interest, owing to inheriting a significant effect on the improvement in efficiency and reliability.

One of the fundamental components of a PV system in grid integration is inverters. Because they operating as a functional conditioner between the PV and the utility grid. Inverters also can be utilized as power quality conditioners at the point of common coupling (PCC). In view of these, there has been a growing concern to achieve effective power injection abilities with reduced controller and topological complexity. The priority of studies in the PV interface can be expressed as reducing cost and increasing grid connection performance. The arrangement of the PV modules and proper sizing of an inverter model related to the electrical specifications of PV modules affect the cost and efficiency of the entire system. The inverters can be categorized in four general ways, namely centralized inverters, string inverters, multi-string inverters and micro-inverter (also named as module integrated converters or AC module) on the basis of the electrical characteristics.

Micro-inverters (MIs) are the compact devices that can be integrated to the individual PV modules. MIs are generally projected for power rating between 50 W and 400 W with weighted efficiency between 90 % and 95 %. These types of inverters present the Plug-N-Play attribution and can be easily mounted on the module frame. MIs can be operated as both grid-connected and stand-alone. Some merits of MIs can be noted as elimination of mismatch losses, limitation of DC power cables, and ensuring the best compatibility between the converter and the PV module in terms of electrical specifications. In addition, maximum power point tracking (MPPT) control for individual PV modules can be assured.

PV MIs include either a single or a two-stage power processing unit. The configuration of the power processing unit primarily affects the control structure of the system. In the single-stage topology, the controller of the inverter is formed to achieve maximum power tracking task and grid connection requirements. It can be said that the inverter should ensure operation on maximum power point (MPP) and injecting current to the utility grid with acceptable power factor and output current distortion by a controller. In a single-stage MI configuration, the decoupling capacitor is inserted to the primary side of the converter. MPPT task and rectified sine current shaping operations are achieved on this capacitor. In this topology, unfolding inverter shapes rectified sine current, where the DC-AC stage is switched at fundamental grid frequency. This topology is also called as MI with pseudo-DC-link. In the two-stage configuration, the DC-DC converter and the DC-AC inverter are operated separately. The DC-DC converter is employed for increasing the DC voltage level and performing the MPPT task. The DC-AC converter is responsible for inverting DC voltage to AC voltage and injecting current to the utility grid in accordance with the grid requirements. This topology is also identified as MI with DC-link. High-frequency (HF) transformers are utilized in most topologies of single-stage and two-stage for providing galvanic isolation. These transformers also fulfill to boost the voltage level to the required values. Single-stage and two-stage MIs have merits and demerits of each other related to being cost-effective, efficient, compact, multifunctional, and have a long lifetime. However, the aforementioned attributes still need to be improved because most of the MIs suffer from short lifespan, high cost, limited efficiency, and limited functionality of the controller.

Most of the commercial MIs suffer from limited lifetime. The main reasons can be stated as the internal temperature stress and the limited lifetime of electrolytic capacitors. In order to deal with these deficiencies, the investigations are focused on decoupling techniques for canceling electrolytic capacitors and using the capacitor that has a long lifetime. Thus, the researches are concentrated on decoupling techniques in order to meet the long life expectancy of MIs. In addition, several modified DC-DC converter topologies are proposed to enhance DC voltage conditioning ability and MPPT capability of the MIs. Also, it is aimed to minimize the number of components and hence the cost. Furthermore, various control structures are proposed to increase efficiency and diminish the implementation complexity. On the other hand, the dynamic grid support and anti-islanding in fault condition properties are expected to satisfy by the MIs controller. The controller should detect the fault in the utility grid and stay connected to the grid during the faults in the permitted limits defined in grid codes. In addition, dynamic grid support capabilities should be provided through the controller to fulfill the reactive power demand, which is fed into the utility-grid during fault transients. The inverter can inject reactive power to the utility grid during the fault so as to carry out voltage recovery. Galvanic isolation is also a crucial necessity to procure safety and limiting the DC current injection by providing electrically and physically isolation.

In this thesis, the controller performance of the MI enhanced to ensure better system reliability and promote overall efficiency. In order to realize these goals, a novel MPPT technique is developed to obtain maximum power from the PV modules under both partially shading conditions and rapidly changing atmospheric conditions. A benchmark study is realized between the proposed and existing MPPT techniques in terms of the control variable, PV module dependency, convergence speed, complexity level, analog or digital implementation, periodic tuning and financial outgoings. A mathematical model, which corresponds to the maximum operating point of the PV module, is derived by using gene expression programming (GEP). The symbolic regression analysis is performed to find the best proper mathematical function. The modeled system is examined with a conventional and proposed MPPT technique under different atmospheric conditions. In order to evaluate the robustness of the proposed MPPT technique, the system is tested in terms of overshoot, convergence speed, tracking accuracy, and the number of oscillations. The performed case studies have demonstrated that convergence speed, dynamic response, and tracking accuracy of the system are substantially improved. The complexity level of the control algorithm is also significantly reduced.

Further, dynamic grid support and anti-islanding detection capabilities are achieved through the improved controller structure without the use of any extra hardware to fulfill grid codes. The presented PV MI system is able to inject reactive current during fault transients with an islanding detection algorithm. The dynamic grid support capability of the developed MI system is tested by changing the desired reactive power amount. According to the grid side demand, the improved inverter topology can provide inductive/capacitive reactive power to the grid during grid faults without the need to decrease the active power. When wide-scale penetration of grid-connected PV systems in the distribution grid is considered, dynamic grid support is a significant requirement especially for the high-power string and central inverters. However, with increased penetration of distributed generations in low voltage grids, dynamic grid support features might be required also for PV-MIs in the future. In light of this, the dynamic grid support capability is ensured to fulfill the grid-connection demands of the PV systems.

The rate of injected harmonics is reduced by incorporating the selective harmonic compensators to the controller. According to the different load conditions injected current harmonic limits are extracted and compensated by the harmonic compensators.

A two-stage PV MI topology is designed and implemented. A detailed design process for PV MI is explained stage by stage.

The proposed MI topology and the control algorithms are designed and analyzed through detailed simulation studies using PSCAD/EMTDC. Moreover, the MATLAB is utilized to determine the controller parameters and test their stabilities. The developed system is implemented experimentally and its performance is verified with extensive case studies. The experimental results are presented in detail and discussed by considering some performance parameters. Realization of high efficiency over a wide range of operations, which is a challenge of MI configuration, is achieved. The obtained results illustrate that the proposed system provides a promising performance even in low and rapidly changing load conditions. Consequently, the developed system can be a considerable candidate for PV MI applications in terms of dynamic performance, weighted efficiency, output current distortion, the fulfillment of grid demands, and reasonable cost.

GENİŞLETİLMİŞ ÖZET

Nüfusun ve sanayileşmenin hızla artması nedeniyle enerji kullanımı son yıllarda ciddi bir ilgi konusu haline gelmiştir. Geleneksel enerji kaynaklarının büyük bölümünü oluşturan fosil yakıtlar, artan enerji talebindeki boşluğu doldurmakta, ancak fosil yakıtların tükenmesi, artan petrol fiyatları, geleneksel enerji kaynaklarının neden olduğu çevresel sorunlar, küresel ısınmaya bağlı iklim değişiklikleri, fosil yakıtların yanmasından kaynaklanan karbon emisyonlarının etkisi ve çevre kirliliği, insanları sürdürülebilir enerji kaynaklarını aramaya itmektedir. Bu bakış açısıyla, yenilenebilir enerji kaynakları genellikle bu sorunların üstesinden gelmek için fosil yakıtlara en uygun alternatiflerden biri olarak görülmektedir. Yenilenebilir enerji kaynaklarının öne çıkan özellikleri sürdürülebilir, bol, sonsuz ve çevre dostu olmaları olarak gösterilebilmektedir. Güneş enerjisi, güneşin bol ve sürdürülebilir bir karakteristiği olması nedeniyle bugünün ve geleceğin temel yenilenebilir enerji kaynağı olarak düşünülmektedir.

Son on yılda, fotovoltaik (FV) teknolojisinde hızlı gelişmeler yaşanmıştır. Teknolojik gelişmelere bağlı olarak küresel toplam kurulu FV sistem kapasitesi, belirgin bir artış göstermiştir. Dünya genelindeki kurulu kapasite bakımından solar enerji, hidroelektrik ve rüzgar enerjisinden sonra en önemli üçüncü yenilenebilir enerji kaynağıdır. FV santralleri, dünyanın çeşitli bölgelerinde elektrik üreten, rakipsiz geleneksel elektrik üretim tesisleri için alternatif bir çözüm haline gelmektedir. FV sistemler şebekeden bağımsız ve şebekeye bağlı olmak üzere iki şekilde kurulabilir. Güneş enerjisini daha verimli kullanmak için şebekeye bağlı FV sistemleri üzerinde yoğun çalışmalar sürdürülmektedir. Avrupa'daki FV enerji üretim tesisleri çoğunlukla şebekeye bağlanmakta ve küçük bir yüzdesi şebekeden bağımsız olarak kullanılmaktadır. Bu FV sistemlerinin her ikisinde de eviriciler, verimlilik ve güvenilirliğin iyileştirilmesi üzerinde önemli bir etkisi olması nedeniyle büyük ilgi görmektedir.

Şebeke entegrasyonunda FV sisteminin temel parçalarından biri eviricilerdir. Çünkü şebeke ve FV panel arasında fonksiyonel arayüz olarak çalışırlar. Eviriciler ayrıca ortak bağlantı noktasındaki (OBN) güç kalitesi sağlayıcıları olarak da kullanılabilmektedirler. Bu bağlamda, azaltılmış kontrolcü ve topoloji karmaşıklığı ile etkili güç transfer yetenekleri sağlamak için eviricilere artan bir ilgi oluşmaktadır. FV evirici çalışmalarının önceliği maliyetleri düşürmek ve şebeke bağlantı performansını arttırmak olarak ifade edilebilir. FV panellerinin dizilimi ve elektriksel özellikleri ile uyumlu bir evirici modeli seçimi, genel sistemin maliyetini ve verimliliğini etkilemektedir. Eviriciler elektriksel karakteristiklerine göre, merkezi eviriciler, dizi eviriciler, çoklu-dizi eviriciler ve mikro-eviriciler (ayrıca modül entegre dönüştürücüler ya da AA modülü olarak da adlandırılır) olarak adlandırılan dört genel şekilde sınıflandırılabilmektedirler.

Mikro-eviriciler her bir FV panele entegre edilebilecek kompakt cihazlardır. Mikro-eviriciler genellikle, 50 W ile 400 W güç aralığı için %90 ile %95 arasında verimlilik hedefi ile dizayn edilmektedir. Bu tip eviriciler, tak-çalıştır özelliği sunmaktadır ve panel çerçevesine kolayca monte edilebilmektedir. Mikro-eviriciler şebekeye bağlı ve şebekeden bağımsız olmak üzere iki şekilde çalışabilmektedir. Mikro-eviricilerin bazı avantajları, uyumsuzluk kayıplarının giderilmesi, DA güç kablolarının azaltılması ve dönüştürücü ile FV panel arasında elektriksel özellikler açısından uygunluğun sağlanması olarak gösterilebilmektedir. Ayrıca, FV panele özgü maksimum güç noktası takibi (MGNİ) kontrolü sağlanabilmektedir.

FV mikro-eviriciler tek-aşamalı veya iki-aşamalı güç işleme birimi içerebilmektedirler. Güç işleme biriminin konfigürasyonu öncelikli olarak sistemin kontrol yapısını etkilemektedir. Tek-aşamalı topolojide, evirici kontrolcüsü maksimum güç noktası takibi ve şebeke bağlantı gereksinimlerinin sağlanması için şekillendirilmektedir. Eviricinin maksimum güç noktasında çalışması ve uygun güç faktörü ile çıkış akım bozunumunda şebekeye akım basması tek kontrolcü ile sağladığı söylenebilmektedir. Tek-aşamalı mikro-evirici konfigürasyonunda dekuplaj kapasitörü çeviricinin birincil tarafına yerleştirilmektedir. MGNİ görevi ve doğrultulmuş sinüs akım şekillendirme bu kapasitör üzerinden yapılmaktadır. Bu topolojide, şebeke frekansında tetiklenen çözümleyici evirici doğrultulmuş sinüs akımını şekillendirir. Bu topoloji aynı zamanda sanal DA bağlayıcılı mikro-evirici olarak da bilinmektedir. İki-aşamalı mikro-evirici konfigürasyonunda, DA-DA çevirici ve DA-AA evirici ayrı çalışmaktadır. DA-DA çevirici DA gerilim seviyesinin yükseltilmesi ve MGNİ görevinin yapılması için kullanılmaktadır. DA-AA DA gerilimin AA gerilime evrilmesinden ve şebeke gereksinimleri sağlanarak şebekeye akım basılmasından sorumludur. Bu konfigürasyon aynı zamanda DA bağlayıcılı mikro evirici olarak da bilinmektedir. Bir çok tek-aşamalı ve iki-aşamalı topolojide yüksek frekanslı trafolar kullanılmaktadır. Bu trafolar aynı zamanda gerilim seviyesinin istenilen değerlere yükseltilmesini sağlarlar. Tek-aşamalı ve iki-aşamalı mikro-eviricilerin bir birlerine göre düşük fiyat, verimlilik, kompakt yapı, fonksiyonellik, ve uzun ömür yönünden avantaj ve dezavantajları bulunmaktadır. Bununla birlikte, yukarıda bahsedilen özelliklerin hala geliştirilmesi gerekmektedir, çünkü mikro-eviricilerin çoğu hala kısa ömür, yüksek maliyet, sınırlı verimlilik ve kontrol cihazının sınırlı işlevselliğinden ötürü problem oluşturmaktadır.

Ticari mikro-eviricilerin çoğu sınırlı bir ömre sahiptir. Temel sebepler iç sıcaklık stresi ve elektrolitik kapasitörlerin ömrünün sınırlı olması olarak gösterilmektedir. Bu eksikliklerin üstesinden gelmek için, araştırmalar elektrolitik kapasitörlerin elimine edilmesi ve uzun ömürlü kapasitörlerin kullanılması için dekuplaj teknikleri üzerine odaklanmaktadır. Bu nedenle, araştırmalar mikro-eviricilerin uzun ömür beklentilerini karşılamak için dekuplaj teknikleri üzerine odaklanmaktadır. Ek olarak, mikro-eviricilerin DA gerilim işleme özelliğini ve MGNİ kapasitesini arttırmak için birkaç modifiye DA-DA çevirici topolojisi önerilmektedir. Ayrıca eleman sayısının ve dolayısıyla maliyetin azaltılması da amaçlanmaktadır. Ayrıca, verimliliği arttırmak ve gerçeklenme karmaşıklığını azaltmak için çeşitli kontrol yapıları önerilmektedir. Öte yandan, dinamik şebeke desteği ve arıza durumunda ada modu özelliklerinin mikro-eviricilerin kontrolcüsü tarafından karşılanması beklenmektedir. Kontrolcü şebekede oluşan hatayı tespit etmeli ve arıza sırasında şebeke kodlarınca tanımlanan izin verilen limitler dahilinde şebekeye bağlı kalmalıdır. Ek olarak, hata geçişleri sırasında şebeke tarafından talep edilen reaktif gücün verilmesi kontrolcü aracılığıyla dinamik şebeke destek yeteneği ile sağlanmalıdır. Evirici şebeke geriliminin tekrar düzelmesini sağlamak için arıza sırasında şebekeye reaktif güç enjekte edebilir. Galvanik izolasyon ise güvenlik sağlamak ve elektriksel-fiziksel izolasyon sağlayarak DA akım enjeksiyonunu sınırlandırmak için önemli bir gerekliliktir.

Bu tezde, arttırılmış sistem güvenilirliği ve genel verimliliği arttırmak için mikro-eviricinin kontrolcü performansı geliştirilmiştir. Bu hedeflerin gerçekleştirilmesi amacıyla, kısmi gölgelenme koşulları altında ve hızla değişen atmosferik koşullar altında FV panellerden maksimum güç çekmek için yeni bir MGNİ yöntemi geliştirilmiştir. Önerilen ve mevcut MGNİ yöntemleri arasında kontrol değişkeni, FV panel bağlılığı, yakınsama hızı, karmaşıklık seviyesi, analog veya dijital, periyodik ayarlama ve finansal giderler açısından kapsamlı bir karşılaştırma yapılmıştır. FV panelin maksimum çalışma noktasını sağlayan matematiksel bir model, gen ifade programlama (GİP) kullanılarak türetilmiştir. Parametrik olmayan regresyon analizi en uygun matematiksel fonksiyonu bulmak için yapılmıştır. Modellenen sistem, farklı atmosferik koşullar altında geleneksel ve önerilen MGNİ tekniği test edilmiştir. Önerilen MPPT tekniğinin performansını değerlendirmek amacıyla aşırı salınım, yakınsama hızı, izleme doğruluğu ve salınım sayısı açısından test edilmiştir. Yapılan durum çalışmaları yakınsama hızının, sistemin dinamik yanıtını ve izleme doğruluğunun önemli ölçüde iyileştirildiğini göstermiştir. Kontrol algoritmasının karmaşıklık seviyesi de önemli ölçüde azaltılmıştır.

Ayrıca, şebeke gereksinimlerini yerine getirmek için dinamik şebeke desteği ve ada modu tespit yetenekleri herhangi bir ekstra donanım kullanılmadan geliştirilmiş denetleyici yapısı vasıtasıyla sağlanmıştır. Sunulan FV evirici sistemi arıza geçişleri sırasında ada modu tespit algoritması bulundurarak reaktif akım enjekte edebildi. Geliştirilen mikro-evirici sisteminin dinamik şebeke destek yeteneği, istenen reaktif güç miktarı değiştirilerek test edilmiştir. Şebeke tarafındaki talebe göre, geliştirilmiş evirici topolojisi, şebeke arızaları sırasında aktif gücü azaltmaya gerek kalmadan şebekeye endüktif/kapasitif reaktif güç sağlayabilmiştir. Şebeke bağlı FV sistemlerinin dağıtım şebekesine geniş çapta bağlantısı göz önüne alındığında, dinamik şebeke desteği, özellikle yüksek güçlü dizi ve merkezi eviriciler için önemli bir konudur. Fakat, dağıtık üretim tesislerinin alçak gerilim şebekesine artan bağlantıları ile dinamik şebeke desteği özelliği gelecekte FV mikro-eviriciler içinde gereklilik olabilecektir. Bu sebeple, dinamik şebeke desteği kabiliyeti FV sistemlerinin şebeke bağlantı talebini yerine getirmek için sağlanmıştır.

Enjekte edilen harmoniklerin oranı kontrolcüye dahil edilen seçici harmonik kompanzatörler aracılığıyla düşürülmüştür. Farklı yük koşullarına göre enjekte edilen akım harmonik limitleri harmonik kompansatörler tarafından tespit edilmiş ve kompanze edilmiştir.

İki aşamalı bir PV MI topolojisi tasarlanmış ve uygulanmıştır. PV MI için ayrıntılı bir tasarım süreci aşama aşama açıklanmıştır.

Önerilen topoloji ve kontrolcü algoritmaları PSCAD/EMTDC kullanılarak yapılan detaylı benzetim çalışmaları ile tasarlanmış ve analiz edilmiştir. Ek olarak control parametrelerinin belirlenmesi ve kararlılık testi için MATLAB kullanılmıştır. Geliştirilen sistem deneysel olarak gerçeklenmiş ve performansı kapsamlı vaka çalışmaları ile doğrulanmıştır. Kurulan sistem benzetimlerle analiz edilip sonrada deneysel olarak gerçeklenmiştir. Deneysel sonuçlar detaylı olarak sunulmuş ve bazı performans parametreleri düşünülerek tartışılmıştır. Mikro-evirici konfigürasyonunda zorlayıcı olan geniş çalışma aralığında yüksek verimlilik elde edilmesi sağlanmıştır. Elde edilen sonuçlar, önerilen sistemin düşük ve hızlı değişen yük koşullarında bile kayda değer bir performans sağladığını göstermektedir. Sonuç olarak, geliştirilen sistem, FV mikro-evirici uygulamaları için dinamik performans, verimlilik, çıkış akımı bozunumu, şebeke taleplerinin karşılanması ve makul maliyet açısından önemli bir aday olabilir.

ACKNOWLEDGEMENTS

First and most of all, I would like to express my deepest gratitude to my supervisor Assoc. Prof. Dr. Ahmet TEKE for his expertise, assistance, complete support, and patience throughout this thesis. His scientific approach has enabled me to accomplish this study.

I owe my deepest gratitude to Asst. Prof. Dr. Adnan TAN for his support, suggestions, encouragement, and guidance in surpass all the challenges. His extensive knowledge and invaluable recommendations have helped me to complete my thesis.

In addition, I would like to extend my sincere gratitude to the members of the jury Assoc. Prof. Dr. Turgay İBRİKÇİ, Assoc. Prof. Dr. Lütfü SARIBULUT, and Asst. Prof. Dr. Necdet Sinan ÖZBEK for many generous and helpful suggestions.

I also would like to acknowledge the financial support of the Scientific and Technological Research Council of Turkey for the research project entitled "Controller Design and Experimental Verification of Grid Connected Two-Stage Micro-Inverters for Photovoltaic Applications" (Project Number: 118E940). Also, the financial support of the Scientific Research Project Unit of Çukurova University (Project Number: FDK-2017-9136) is gratefully acknowledged.

I would also like to thank my roommate Dr. Kasım ZOR for his morals and supports. Special thanks go to Asst. Prof. Dr. Hatice Başak YILDIRIM and Dr. Oğuzhan TİMUR for their supports and friendship that improving my motivation.

The last but certainly not least, I would like to express my gratitude and thanks to my family for their continuous support and love.

CONTENTS **PAGE**

LIST OF TABLES **PAGE**

LIST OF FIGURES **PAGE**

LIST OF ABBREVIATIONS

AC	: Alternating Current
ADC	: Analog to Digital Converter
BCM	: Boundary Conduction Mode
CCM	: Continuous Conduction Mode
CEC	: California Energy Commission
CSI	: Current Source Inverter
DCM	: Discontinuous Conduction Mode
DG	: Distributed Generation
DSP	: Digital Signal Processor
EMC	: Electromagnetic Compatibility
EMI	: Electromagnetic Interference
GEP	: Gene Expression Programming
GW	: Giga Watt
HF	: High Frequency
IC	: Integrated Circuit
IEA	: International Energy Agency
IEC	: International Electrotechnical Commission
IEEE	: Institute of Electrical and Electronic Engineers
INC	: Incremental Conductance
LPF	: Low Pass Filter
LVRT	: Low Voltage Ride Through
MAE	: Mean Absolute Error
MAPE	: Mean Absolute Percentage Error
MCU	: Microcontroller Unit
MI	: Micro-Inverter
MIC	: Module Integrated Converter
MOSFET	: Metal Oxide Semiconductor Field Effect Transistor

MPPT	: Maximum Power Point Tracking
MSE	: Mean Squared Error
P&O	: Perturb & Observe
PCB	: Printed Circuit Board
PCC	: Point Common Coupling
PD	: Proportional Derivative
PI	: Proportional Integral
PID	: Proportional Integral Derivative
PLL	: Phase Locked Loop
PQ	: Power Quality
PR	: Proportional Resonant
PV	: Photovoltaic
PWM	: Pulse Width Modulation
REN	: Renewables Now
RMSE	: Root Mean Squared Error
THD	: Total Harmonic Conduction
VSC	: Voltage Source Converter
VSI	: Voltage Source Inverter

1. INTRODUCTION

The research methodology is introduced in this chapter. Initially, the importance of renewable energy is given, and then a brief review of PV systems and inverters is presented. The importance of design, control, and operation of grid-connected PV inverters are explained in detail. In addition, power quality requirements defined in the grid connection standards and maximum power point tracking demands are investigated. Further, a number of methods in control of PV inverters are addressed. The research objectives, contributions, and the organization of the thesis are ensured in this chapter.

1.1. Background and Motivation

In recent years, increasing electrical power demand with an increment of population and industrialization leads to growing attention in renewable energy sources. Also, the increasing price of fossil fuels, environmental pollution, climate changes related to global warming, and the energy crisis due to a limited source of fossil fuels make utilization of renewable energy sources major priority (Trujillo et al., 2016; Shimizu et al., 2006). The remarkable attributes of renewable energy sources can be stated as being sustainable, plentiful, endless and eco-friendly. Among the sustainable energy sources, solar energy attracts attention as being the promising and prevalent energy source (Çelik et al., 2018). Over the past few decades, installed PV power has been exhibited an accelerated development and the global cumulative installed PV system capacity reaches 505 GW at the end of 2018 as shown in Figure 1.1 (REN, 2019).

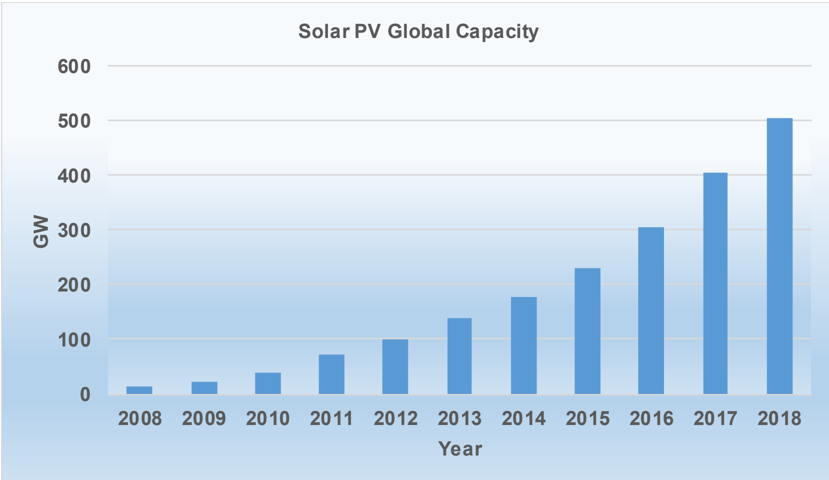

Figure 1.1. Current status of cumulative installed PV power (REN, 2019)

IEA's Renewables 2019 market report reveals that total renewable-based power generation capacity over the world will increase by 50% between 2019 and 2024 (IEA, 2019). Solar PV systems have major expansion potential. They are followed by onshore wind and hydropower as shown in Figure 1.2.

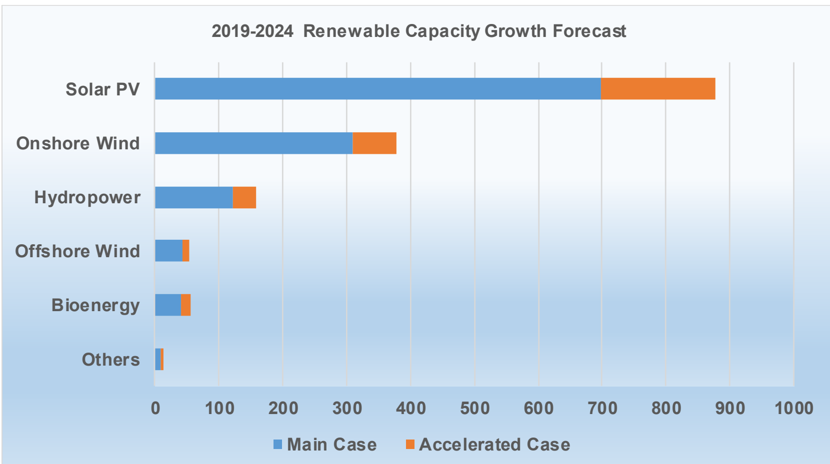

Figure 1.2. 2019-2024 Renewable capacity growth forecast by IEA (IEA, 2019)

The 98.7% of installed cumulative PV power in Europe is directly delivered to the utility grid and the remaining part feeds the local load by operating as an off-grid system (Trujillo et al., 2016; Hasan et al., 2017). In grid-connected PV systems, inverters gained more attention, due to having an important effect on providing power quality demands (Hassaine et al., 2014). Therefore, inverters can be considered as one of the fundamental parts of PV systems. Because they operating as a functional conditioner between the PV and the utility grid as demonstrated in Figure 1.3.

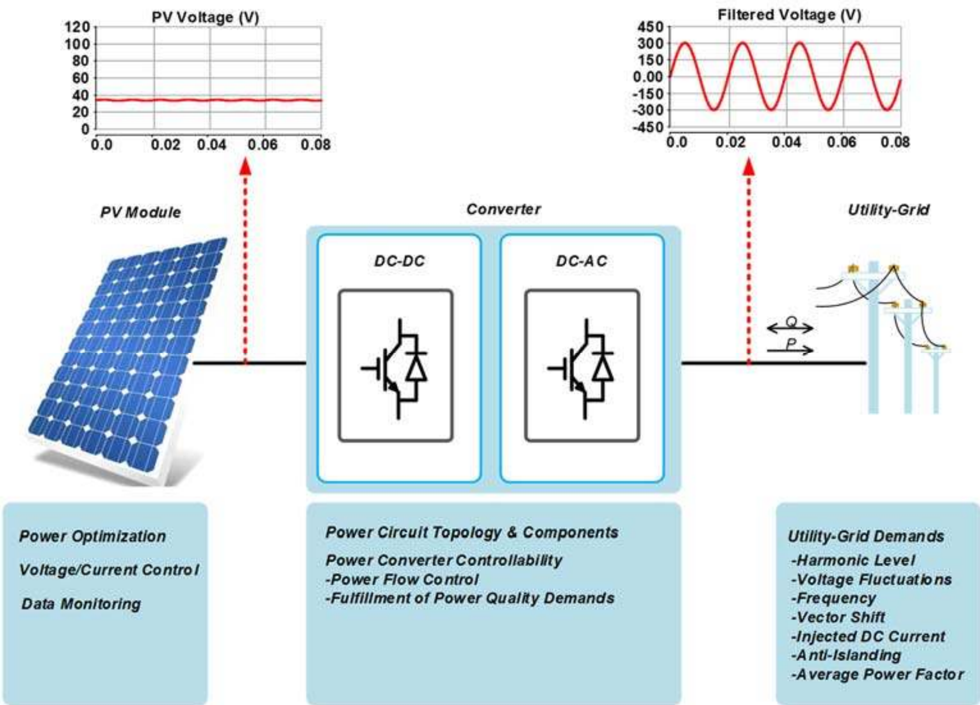

Figure 1.3. Grid-connected PV power conversion systems

Besides the controllability of inverters to provide power quality demands, reasonable efficiency needs to be obtained over a wide range of operations, which is a challenge for inverters.

In view of the foregoing, the researches in the PV interface concentrates on improving controllability and increasing efficiency by reducing controller and topological complexity. It should be noted that communication and monitoring are also crucial features for the PV inverters when smart energy systems are considered. Thus, monitoring and communication features should also be ensured for PV inverters.

PV systems are substantially established by connected to the utility grid. The PV inverters are functional operation devices between PV and grid. PV inverters can be structured in four basic topologies on the basis of different connections of the PV modules and electrical characteristics. These structure topologies can be named as a central inverter, string inverter, multi-string inverter, and micro-inverter (Hassaine et al., 2014; Kjaer et al., 2005).

In central inverter topology, a bulk of PV modules are connected in series to constitute strings. These strings are also paralleled to increase the current. The aim can be stated as boosting input voltage and reach the rated voltage value of the inverter. The constituted strings are paralleled through string diodes to attain high power levels (Zeb et al., 2018). For high power levels the two-level inverter configuration, may not be a feasible solution. Utilization of two-level inverters in high power applications can cause high power losses and high voltage stresses across the power devices (Yang, 2019). Therefore, for high power applications, multilevel inverter configurations can be used. In that case, the output voltage level is increased and thus the output filter requirements are decreased. The decrement in output filter contributes to increased efficiency (Yang et al., 2019). Central inverters suffer from the mismatch and partial shading conditions, which highly affect the overall efficiency.

String inverters can be referred as a power level modified configuration of centralized inverters. It is possible to find two types of string inverters. They can contain either a single-stage or a two-stage power process unit. Most of the string inverters are designed for single-phase connection with the power ratings lower than

10kW. The mismatch and partial shading effects are also decreased in this configuration. It is worth mentioning that the efficiency of the entire system is improved by the value of 1-3% compared to the central inverter (Hassaine et al., 2014; Edwin et al., 2014; Yang et al., 2019).

Multi-string inverters are evolved from the string inverters. Substantially, they are string inverters that have more power input ports. Extra power ports provide to control small strings and simplicity in the alignment of PV modules according to the installation area. It can be seen that in the multi-string inverter configuration, the operation of independent PV panel strings with individual MPPT is provided by connecting each string to a unique inverter (Sher and Addoweesh, 2012). Furthermore, it can reach an increased power level when compared to a string inverter. In this manner, it is possible to make the string inverters more attractive in terms of the price per kW.

MIs can be indicated as the actual PV inverter configuration. Henk Oldenkamp initiated the design of the first this type of inverter in 1991. The basic idea is that inverters will be connected to individual PV modules. They can be placed on the frame of the PV modules. Hence, DC wiring is considerably reduced. The basic ideas that led to the emergence of this topology can be expressed as high DC voltage level, safety problems, cable loss, and risk of fire (Oldenkamp et al., 1995). Thus, the AC module that also termed as micro-inverter technology is aroused to tackle these problems. MIs are particularly well-suited for the utilization in small scale PV systems up to 2 kW. Nowadays, most of the MIs are designed are generally projected for power rating between 50 W and 400 W with weighted efficiency between 90% and 95%. This topology inherent various advantages over the aforementioned inverter configurations. These advantages can be expressed as;

- Independent operation of PV modules,
- Plug-N-Play operation,

- Reduced installation cost,
- Minimization of DC power wiring,
- Extraction of maximum energy from a PV module,
- Reducing shading and soiling effect by providing individual MPPT,
- Elimination of mismatch loss,
- Compact design and smaller volume,
- No need for string diodes.

MIs propose an opportunity for future PV system designs by having numerous advantages as mentioned hereinabove (Hu et al., 2012). However, the technical challenges for MIs such as high manufacturing cost, low lifespan, limited functions for grid requirements, and low efficiency still need to be investigated in detail. In order to alleviate these shortcomings, many circuit topologies with suitable control techniques are highlighted in the literature. To overcome the limited lifespan problem, the investigations are focused on decoupling techniques for eliminating electrolytic capacitors and using the capacitor that has a long lifetime. Thus various decoupling techniques are developed to eliminate electrolytic capacitors by reducing the required capacity and ensure a long lifespan for MIs (Kjaer et al., 2005; Hu et al., 2012; Hu et al., 2013; Harb and Balog, 2013; Hu et al., 2010; Shimizu et al., 2006; Bower et al., 2007; Chiu et al., 2014; Pragallapati and Agarwal, 2014). Also, from the standpoint of ensuring increased efficiency various DC-DC converter topologies are introduced to promote DC voltage conditioning ability and MPPT potential of the MIs (Cha et al., 2016; Patidar and Umarikar, 2015). Furthermore to improve efficiency, overcome the limited functions for grid requirements, and reduce the complexity of controller various control structures are developed (Hu et al., 2012; Jiang et al., 2012; Trujillo et al., 2016; Nayanasiri et al., 2013; Fang and Ma, 2010; Petreuş et al., 2013; Trujillo et al., 2011; Arab et al., 2014; Trujillo et al., 2013; Zhang et al., 2013; Gao et al., 2014; Kim et al., 2014; Meneses et al., 2015;

Lee et al., 2016; Kim et al., 2013). On the other hand, the dynamic grid support and anti-islanding in fault condition properties are expected to meet by the MIs controller. The controller should detects the fault in the utility grid and stay connected to the grid during the faults in the permitted limits defined in grid codes or interrupts the power flow in case of long duration fault conditions (Trujillo et al., 2010; Kwak et al., 2016). The leakage current problem, which emerges in transformerless MIs, forming significant safety problems. Various mitigating techniques are proposed for the leakage current problem (Khan et al., 2017). Galvanic isolation is also a significant requirement to provide safety and limiting the dc current injection by providing electrical and physical isolation (Lai et al., 2016). Besides these attributes, reduction of noise caused by the cooling fans, limited lifespan, and data monitoring can be reported as the notable features of the MIs that need to be improved.

1.2. Research Objectives

MIs still suffer from high manufacturing costs, constrained energy conversion efficiency rates, and poor power quality conditioning capabilities in comparison with other inverters types. Thus, it is essential for an MI topology to enhance the efficiency of power circuits that including DC-DC and DC-AC converters. Also, the extracted power from the PV modules should be enhanced by using robust MPPT methods. Furthermore, with the growing market share of grid-connected MI, the penetration of PV systems using MIs will grow as well, leading to new phenomena, which may eventually result in grid instabilities. From the standpoint of grid instabilities, MIs' controller structure should be improved for grid demands and fault conditions.

In view of the foregoing, the objectives of the presented research are determined to overcome the aforementioned shortcomings and implement the expected improvements.

The objectives are given as follows:

- Investigation of the characteristics, design and control parameters of MI configurations include single and two processing stages.
- Detailed investigation of DC-DC power circuit topologies and their control structures and proposing the circuit topology with the best result.
- Proposing novel soft computing methods or numerical methods based on maximum power point tracking techniques to attain maximum power from the PV module.
- It is aimed to carry out a comprehensive comparison between the proposed and existing maximum power point tracking techniques in terms of the control variable, PV array dependency, convergence speed, complexity level, analog or digital, periodic tuning and financial outgoings.
- It is aimed to analyze the robustness of the maximum power point tracking techniques under both rapidly changing atmospheric conditions and partial shading conditions.
- Investigation of the control structure of the DC-AC part of micro-inverter and developing a novel control method for meeting grid demands and compensating fault conditions, which cause grid instabilities.
- It is aimed to achieve an experimental verification to validate the performance of the proposed controller structure.
- Presenting a detailed design approach based on theoretical analysis and simulation studies for PV MI.
- Construction of a 0.25 kW experimental prototype to verify the overall system.
- Developing a control structure for the MI in order to supply reactive power to the grid.

1.3. Contribution of the Thesis

The original contributions of the present research can be summarized as follows:

- The controller performance of the MI enhanced to provide better system reliability and promote overall efficiency.
- A novel MPPT method is proposed to obtain maximum power from the PV modules under both partially shading conditions and rapidly changing atmospheric conditions.
- A benchmark study is conducted between the proposed and existing MPPT methods with regard to the control variable, PV array dependency, convergence speed, complexity level, analog or digital, periodic tuning and financial outgoings.
- Dynamic grid support and anti-islanding detection capabilities are provided through the improved controller structure without the use of any extra hardware to fulfill grid codes.
- The rate of injected harmonics is reduced by incorporating the selective harmonic compensators to the controller.
- A detailed design approach based on theoretical analysis and simulation studies for MI is presented.
- The improved MI topology and its controller are experimentally implemented.
- The experimental set-up can be a considerable candidate to be a commercial product in Turkey.

1.4. The Organization of the Thesis

This thesis is organized as follows:

Chapter 1: Introduction

A brief introduction to the thesis with clarified designs is presented by stating background and motivation, research objectives and contributions and organization of the thesis.

Chapter 2: Fundamentals of PV Systems and Inverters

An overview of PV systems and inverters is introduced by providing a summary of related literature including Ph.D. theses and publications.

Chapter 3: State-Of-The-Art MI Technologies

In this chapter, the state-of-the-art MI technologies are investigated meticulously. Designed topologies for grid-connected MIs and their controllers are explained rigorously. Commercially available MIs are examined and their technical details are tabulated in detail.

Chapter 4: Design and Implementation of Developed PV MI

Circuit description and operation principles of developed PV MI are explained. The proposed control strategy of the designed MI expressed in detail with the help of an explanatory flowchart. The experimental design procedure of a laboratory prototype of developed PV MI and preliminaries are given in Chapter 4. The design of the power circuit and control system are presented with some mathematical equations. Schematic designs and PCB layout of the overall system is also presented in this chapter.

Chapter 5: Simulation Model of Grid-Connected PV MI

In this chapter, the presented PV MI is verified through simulations by conducting different case studies.

Chapter 6: Experimental Results and Discussion

The experimental results of the PV MI prototype are provided by conducting various case studies. The developed controller and design approach of the PV MI is verified with experimental results.

Chapter 7: Conclusion and Future Work

Chapter 7 gives some concluding remarks, summarizes the main contributions, and discusses future directions of the thesis.

The organization of the thesis is demonstrated in Figure 1.4.

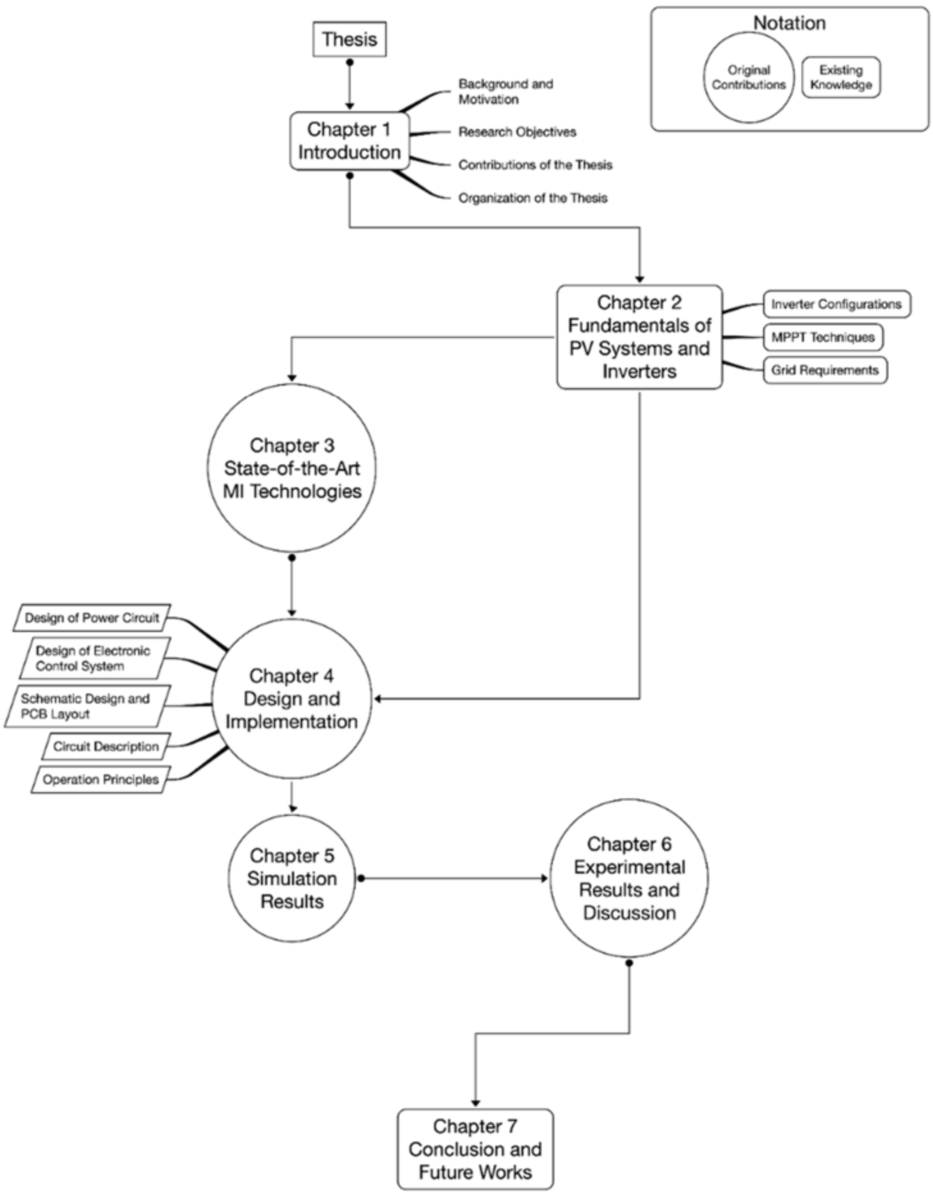

Figure 1.4. Organization of the thesis

1.5. Summary

In the introduction part, the motivation and background of this thesis are introduced. Then the research objectives of this research are explained in detail and the main contributions are meticulously addressed. Finally, the organization of the thesis is presented.

2. FUNDAMENTALS OF PV SYSTEMS AND INVERTERS

This section investigates the fundamentals of PV systems and inverters by providing a summary of related literature including publications. PV module characteristics, MPPT techniques, inverters configurations, PV system connection forms, and grid connection standards are explained rigorously.

2.1. PV Systems and PV Module Characteristic

A PV system can be introduced as a system consists of PV modules coupled with an inverter and other electrical and mechanical components. PV cells, which is a specialized semiconductor diode, can be expressed as a fundamental component of this system. The direct current is generated from light owing to the photoelectric effect on this material. PV systems including many benefits such as being silent, eco-friendly, inexhaustible, sustainable, and having low maintenance costs. However, they suffer from high initial purchasing and installing costs, which negatively affect the payback time. It is worth to emphasize that the PV module prices decrease by about 29% in 2018, to a global average of 22.4 cents per watt (REN, 2019). However, the most efficient PV modules on the market today have efficiency ratings between 20-23%, whereas the majority of modules efficiency range varies from 15% to 17%. Although prevalent studies have been realized by enhancing PV module efficiency, improvement rates have still not reached the expected level. It is worth to point out that, improving power converter technology and its MPPT capability can be a competitive candidate when power generation capacities of the PV systems are considered (Çelik, 2015).

PV systems can be implemented in two ways, which can be stated as stand-alone and grid-connected form. It should be noted that most of PV systems are designed to operate in grid integrated mode. These systems can be more economical due to not requiring battery storage systems. The elimination of battery storage systems also contributes to reducing the amortization period of the PV system.

Edmund Becquerel realized that the electrical currents eventuate from the specific light level based chemical reactions in 1839. In 1883 Charles Fritts produced the first solid-state PV cell. These PV cells are formed from the junctions produced by layering the semiconductor selenium with a thin layer of gold (Chaar et al., 2011). Subsequently, the handy cells were demonstrated at Bell laboratories. These practical PV cells are not proper for commercial utilization due to their high manufacturing cost. Up to now, the studies have focused on PV materials and structure in order to make them more cost-effective and efficient. Because these materials should be promoted for commercial utilization (Razykof et al., 2011; Chaar et al., 2011). The accelerated expansion of the PV market started in the 1980s and the application of high power capacity PV plants become possible over the world. In this manner, the market expansion is achieved and PV systems become a promising candidate for the energy generation plants (Maycock, 2015).

In traditional PV cell generation technology, silicon material is commonly utilized. In the later stage, amorphous silicon and non-silicon materials are begun to utilize for the production of PV cells. These production technologies can be assumed as the basis of a second-generation PV cell. Intensive studies continue to improve PV cell material. Solar dyes, conductive organic polymers, and organic solar ink-based PV cells, which considered to third-generation PV cells, are developed to generate electricity from certain level light (NREL, 2015). These leading kind of PV cells have advantages and disadvantages in comparison to each other. The main comparison parameters are efficiency, raw material cost, and effective lifespan. The efficiency comparison of some PV technologies is given in Figure 2.1.

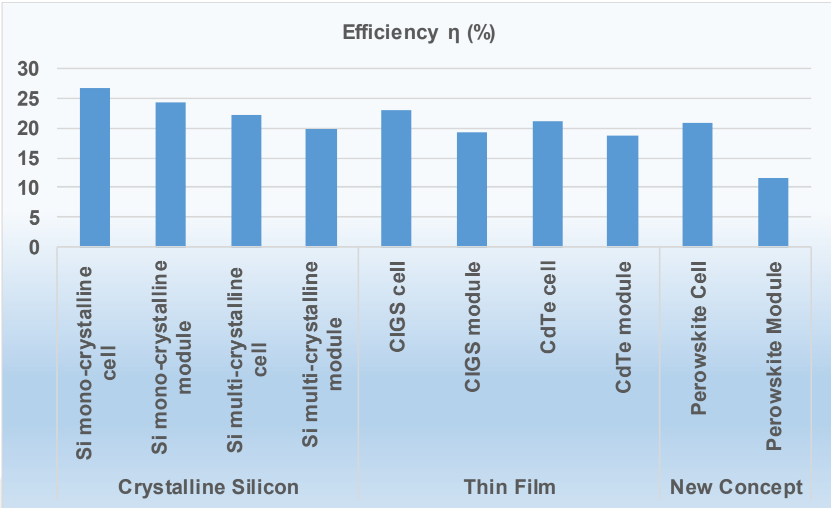

Figure 2.1. Efficiency comparison of PV technologies (Fraunhofer, 2019)

A PV cell is generated from the light-sensitive silicon material based p-n junctions. They can be modeled by a diode parallel with a current source as shown in Figure 2.2 (Celik and Acikgoz, 2007).

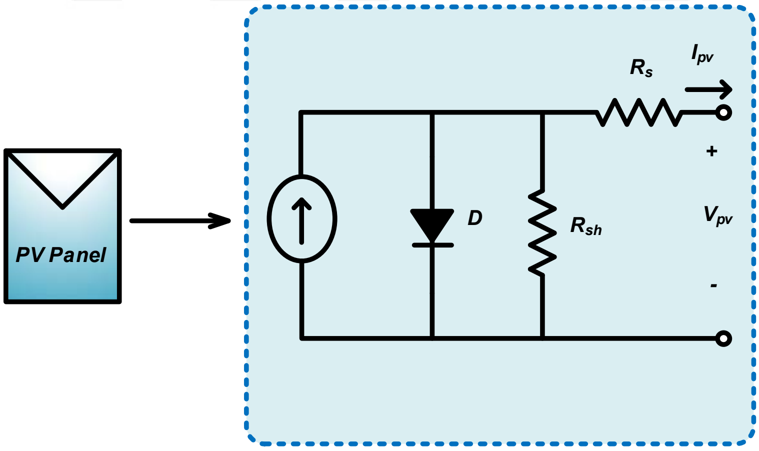

Figure 2.2. The equivalent circuit of a single diode PV cell

A PV module is formed from the series or parallel connected set of cells. The variety of series and parallel connected cells is determined by the expected electrical specifications. PV array's output characteristic, which is dependent on atmospheric conditions. The I/V and P/V characteristic of a simulated PV module is given in Figure 2.3.

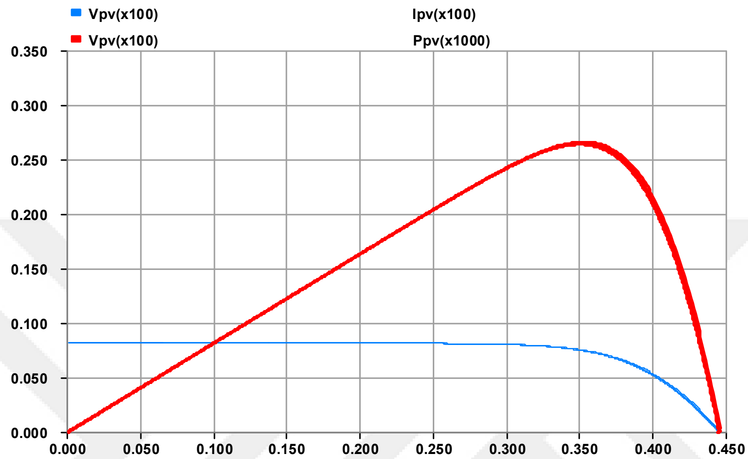

Figure 2.3. I/V and P/V characteristic of a PV module

2.1.1. Maximum Power Point Tracking Techniques

The modest fluctuation of temperature and radiation constitutes visible variations in operating current and voltage of PV modules. These variations affect the output power of the module negatively due to the confusing operating point of the module. There are various MPPT techniques presented in the literature that can realize the task of mitigating the impacts of changes in temperature and radiation. These MPPT techniques commonly utilize the measured voltage and current values of the PV module. The power is calculated by using the measured current and voltage of the PV module. The variation in PV output power is utilized to adjust the duty cycle of the converter for tracking MPP. It can be concluded that the MPPT controller is in charge of the operation of the PV module at MPP independent of atmospheric conditions. MPPT techniques are designed to realize the same objective however they have differences in terms of some performance parameters. These performance parameters can be stated as the complexity level of algorithm, number of oscillations, convergence speed, hardware requirements, and number of sensors related to required control parameters. Besides these parameters, the most important performance criteria of MPPT techniques are operating under partial shading and rapidly changing irradiation conditions. In light of these, MPPT control can be indicated as a strong candidate for improving the PV module power generation capacity (Reisi et al., 2013; Çelik and Teke, 2017). There are many MPPT techniques, which can be categorized into three categories: namely online, offline, and hybrid methods as shown in Table 2.1 (Verma et al., 2016; Ahmad et al., 2019; Belhachat and Larbes, 2019; Motahhir et al., 2019).

Table 2.1. Commonly used MPPT Techniques

Offline MPPT Techniques	**Online MPPT Techniques**	**Hybrid MPPT Techniques**
OCV	P&O	P&O and ANN
SCC	INC	P&O and FL
Lookup Table	Differentiation Based MPPT	P&O and OCV
Curve Fitting	Voltage & Current Feedback MPPT	Neuro-Fuzzy Based MPPT
Numerical Calculation Based on MPP	Incremental Resistance	P&O and Particle Swarm Optimization
Temperature Based Analytic Calculation	Power Feedback MPPT	Genetic Algorithm and FL
FL	Parasitic Capacitance	INC and FL
ANN	Search Algorithms	INC and Neuro-Fuzzy

Many MPPT techniques have been developed to ensure the continuous operation of PV modules on MPP. P&O and INC are widely employed techniques to achieve maximum power point tracking. Also, it is possible to see the implementations of these techniques in commercially available inverters. They can be indicated as the frequently used MPPT techniques for implementations of commercial inverters.

2.1.1.1. Short Circuit and Open Circuit MPPT

One of the widely known offline MPPT techniques in literature is the short circuit current (SCC) (Noguchi et al., 2002). The other one is namely open-circuit voltage (OCV) techniques (Enslin et al., 1997). OCV method employs the approximate linear correlation between V_{OC} and V_{MPP}. The linear equations of OCV and SCC are provided as shown below.

$$V_{MPP} = k_v * V_{OC}$$

$$I_{MPP} = k_i * I_{SC}$$

where, k_v and k_i are constants. These constants are empirically extracted in regard to the measurement of the V_{OC}, V_{MPP}, I_{SC} and I_{MPP} under different atmospheric conditions (Reisi et al., 2013). Due to depending on the type of PV cell, it is a challenging task to determine an optimal value for the constant k_*. Furthermore, the measurement of the VOC and ISC constitute problems because of momentarily disconnecting the DC-DC converter from the PV module. This disconnection is repeated depending on the sampling time and causes significant output power reduction. It is proposed to measure V_{OC} and I_{SC} by utilizing a pilot cell in order to avoid power losses. It is worth to point out that the employment of a pilot cell is not an effective solution because special attention has to be given to determine this pilot cell that has the identical characteristics as the PV module (Salameh et al., 1991; Enrique et al., 2010). Despite these issues, being cost-effective and relatively easy implementation property makes these techniques attractive.

2.1.1.2. Perturb and Observation

P&O can be addressed as the commonly utilized simple MPPT technique. P&O MPPT technique functions on the basis of enforcing small-scaled constant perturbations to the reference voltage by taking the output power of the PV module into account. Here the voltage and current of the PV module are iteratively measured in a specific sampling time interval for the purpose of adjusting the reference value. The perturbation of the reference value is performed according to power alteration. The flowchart of the P&O MPPT technique is depicted in Figure 2.4.

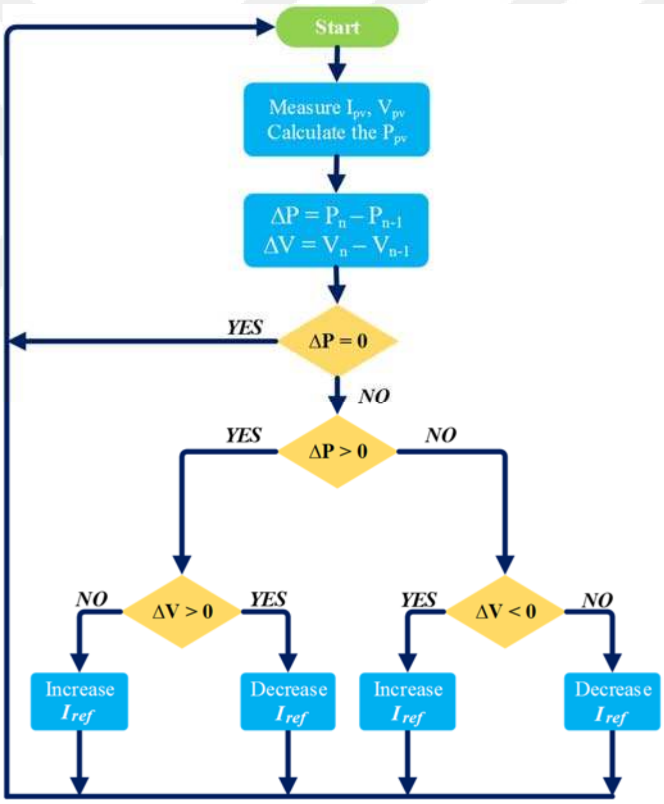

Figure 2.4. The operation principles of the P&O MPPT (Kavurucu, 2014)

Assume that the reference value is perturbed in a direction and $P_k - P_{k-1} > 0$ condition is obtained, the perturbation continues in the same direction continues.

If $P_k - P_{k-1} < 0$ condition is obtained, the direction of perturbation is reversed. Thereby operating voltage reaches the MPP and oscillates on account of the plus and minus reference increments (Ahmed and Salam, 2015; Subudhi and Pradhan, 2013). This can be said as the basic drawback of the P&O technique. Also, this technique can fail to track in the proper direction, away from the MPP, under rapidly changing atmospheric conditions. In addition, rapidly changing conditions cause major deviations in PV module power and the reference value cannot determine the proper perturbation direction in a short time. Despite these disadvantages, easy implementation and being independent of the PV module characteristic make the P&O algorithm popular (Enrique et al., 2010).

2.1.1.3. Incremental Conductance

INC technique also can be stated as a commonly utilized simple MPPT technique. This technique is improved to cope with the shortcomings of the P&O technique. INC technique is even more remarkable in respect to the P&O technique with regard to the reduced number of oscillations and tracking accuracy. However, being more complicated and delicate against the measurement noises makes INC disadvantageous. This technique operates on the basis of the derivative of the module output power with respect to operating voltage as shown below (Safari and Mekhilef, 2011).

$$\frac{dP}{dV} = 0$$

$$\frac{d(IV)}{dV} = I + V\frac{dI}{dV} \cong I + V\frac{\Delta I}{\Delta V}$$

By using the equation given above, the location of MPP can be determined as below.

At MPP: $\frac{\Delta I}{\Delta V} = -\frac{I}{V}$

Left of MPP: $\frac{\Delta I}{\Delta V} > -\frac{I}{V}$

Right of MPP: $\frac{\Delta I}{\Delta V} < -\frac{I}{V}$

The INC algorithm abolishes the oscillation of reference value around MPP, which causes notable power losses. When the control parameter reaches the MPP where $\frac{dP}{dV} = 0$, the perturbation in the control parameter is stopped (Nema and Bhatnagar, 2013). However, failing to track MPP under rapidly changing atmospheric conditions can be expressed as a major shortcoming of the INC technique.

2.1.1.4. MPPT Techniques for MI Applications

A comprehensive literature review of MPPT techniques for MI applications is performed in this section. The most commonly used MPPT techniques for MI applications are P&O and INC, which are basically mentioned above. In addition, SCC and OCV techniques also have a wide application area owing to relatively easy implementation attribution. Petreuş et al., developed a low-cost single-stage MI with the P&O MPPT technique for grid-connected applications (Petreuş et al., 2013). Trujillo et al., explained modeling and control of a push-pull converter for a PV MI. The input voltage of the push-pull converter is manipulated by utilizing a reference constituted by two components. A P&O MPPT technique is utilized to generate one component of the reference signal (Trujillo et al., 2011). Furthermore, in (Chiu et al., 2014; Trujillo et al., 2016; Fang and Ma, 2010; Trujillo et al., 2013; Trujillo et al., 2010; Pragallapati et al., 2015; Ahmed et al., 2013; Liao et al., 2017) performed P&O MTPPT technique for the designed MIs. In these studies, a reference signal is generated by the MPPT block and compared with the actual measured signal. The error between the reference signal and the actual signal is processed through a PI controller in order to obtain a control signal. Jiang et al., highlighted a variable step size MPPT technique for the boost-half-bridge PV MI system. The variable step-size MPPT allows the system to operate correctly and reliably by means of ramp-changed PV voltage. The MPPT method is verified through the experimental setup. The characteristic I/V and P/V curves of the PV module divided into three zones and different perturbation sizes are applied for tracking the MPP according to the operating zones. Gao et al., presented an MPPT technique based on the mathematical model and verified the presented MPPT experimentally. The output current of the developed current-source PV MI is directly controlled by a current reference signal generated by the MPPT block (Gao et al., 2014). Chiu et al., proposed a modified P&O technique to attain high accuracy. The modification is focused on the determination of perturbation size. The perturbation rate ΔV is specified according to the max. and min. rates of the instantaneous PV output power (Chiu et al., 2013). Zhang et al., proposed a center points iteration MPPT algorithm, which is implemented experimentally. The developed MPPT technique applied to an LLC resonant converter. The promising aspects of the developed MPPT technique are stated as elimination of oscillation under steady-state condition, being independent of atmospheric parameters, cope with local maximum points, inheriting fast tracking capability, and simple application. Sahu et al., presented a sliding mode control based analog MPPT for a two-stage single-phase grid-connected PV MI (Sahu et al., 2015). A variable step size INC method is utilized to control the sepic converter based MI (George and Shafeeq, 2014). Rambo et al., proposed a modified P&O MPPT technique. The developed technique based on the employment of derivation of PV power and derivation of PV voltage. It is reported that the dynamic response of the system is improved and steady-state error is reduced. Several MPPT methods are also compared in the literature in terms of the performance criteria. The important performance parameters can be concluded as complexity level, convergence speed, accuracy, requiring periodic tuning, control parameters, and the number of oscillations (Liu et al., 2016; Ahmed and Salam, 2015). The performance of the MPPT techniques must be evaluated under rapidly changing and partial shading conditions, which constitute challenging situations for PV systems. After performing a comprehensive review, it's concluded that soft computing techniques able to cope with partial shading and rapidly changing conditions. It is worth to point out that the complexity level of these techniques is high. Therefore, the implementations of these methods should take into consideration. It should be noted that the commonly utilized MPPT techniques can deal with the rapidly changing atmospheric conditions by performing some modifications. In Table 2.2, a detailed comparison of MPPT techniques is realized with regards to various performance parameters that mentioned above (Mirza et al., 2019; Dhimish, 2019).

Table 2.2. Comparison of MPPT Techniques

MPPT Methods	D/A	Complexity Level	Convergence Speed	Periodic Tuning	Control Parameter	Number of Oscillations
P&O	D/A	Low	Low	No	I, V	High
Adaptive P&O	D/A	Medium	Medium	No	I, V	High
INC	D	Medium	Medium	No	I, V	Medium
Adaptive INC	D	High	Medium-High	No	I, V	Low-Medium
OCV	D/A	Low	Low	No	V	High
SCC	D/A	Low	Low	No	I	High
ANN	D	High	Fast	Yes	Depends	Low
FL	D	High	Fast	Yes	Depends	Low
GA	D	High	Fast	Depends	Depends	Low
PSO	D	High	Fast	Depends	Depends	Low

2.1.2. Classification of PV Inverters

The state-of-the-art PV converter technologies reveal that four basic configurations named as the module converter, string inverter, and central inverter technologies are utilized in grid integration of PV modules as demonstrated in Figure 2.5 (Yang and Blaabjerg, 2015).

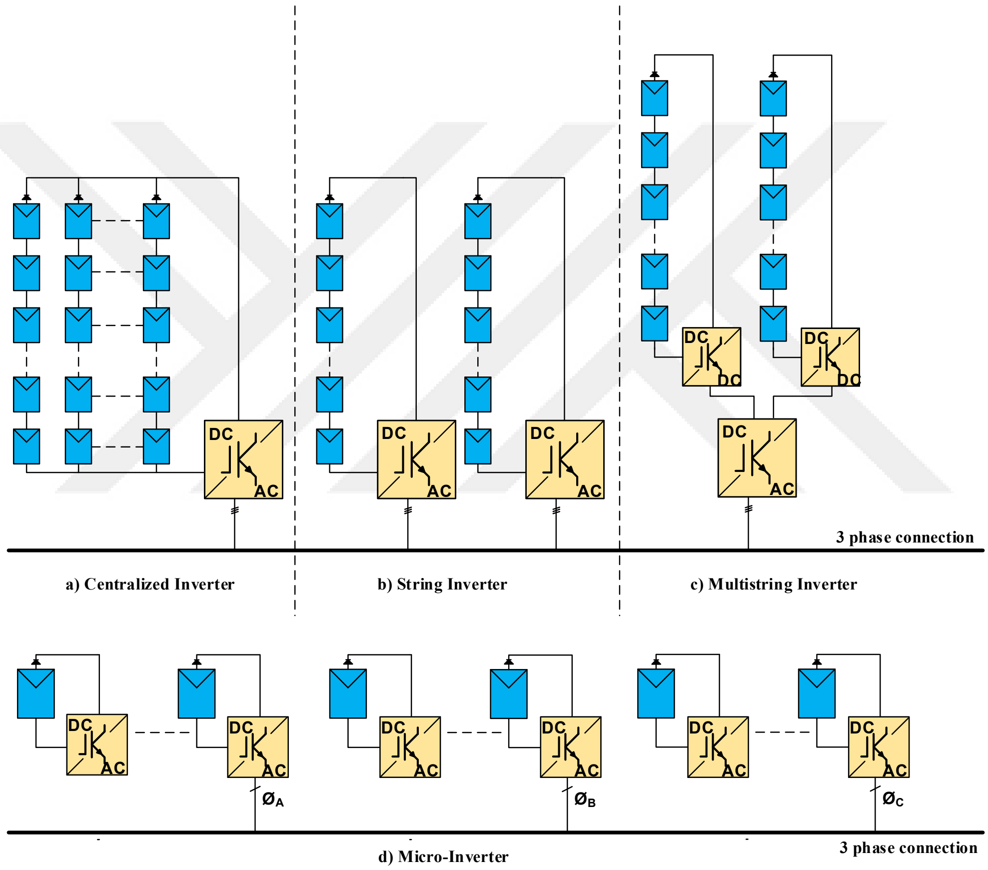

Figure 2.5. Main inverter configurations

These configurations have several advantages and disadvantages to each other. The most considered attributes are the price per watt, efficiency rate, and reliability. In this manner, the market shares of central inverters and string inverters can be said close to each other. They have an extensive range of applications in terms of residential to large scale grid-connected PV plants. However, the MIs propose an opportunity for future PV system designs by having numerous advantages. In the following, the general properties of the main power converter topologies are discussed.

2.1.2.1. Micro-Inverters

MIs can be shown as the latest PV inverter configuration. The majority of MIs, also named as ac module or module integrated converter (MIC), is formed to have power rating from 50 to 400 W. Also they have power conversion efficiencies from 90 to 95%. It can be easily located on the back of a PV module due to consist of a small box. The module-based characteristic of MIs achieves the parallel configuration and the independent plug-N-play functioning of PV modules (Harb et al., 2013). This topology is crucial from the standpoint of providing a solution to module mismatches and partial shading effects. MIs present an opportunity for future PV system designs by inheriting numerous advantages such as improved energy harvesting by proposing module-level MPPT and conversion efficiency, reduced installation cost by proposing Plug-N-Play operation and augmented flexibility (Kjaer et al., 2002). However, the technical challenges for MIs include high manufacturing cost, low lifespan, limited functions for grid requirements, and low efficiency still need to be addressed. In order to cope with these challenges, many circuit topologies with suitable control techniques are proposed in the literature. A detailed review of existing MI topologies will be provided in Chapter 3.

2.1.2.2. String Inverters

String inverters can be addressed as a scaled-down version of centralized inverters. They can be designed as single-stage converters and two-stage converters, which connected to the PV string. It should be noted that medium power applications of PV systems can be installed on a roof and can be placed on a non-regular area. Due to the shape of the installation area, PV modules can not be positioned in planned alignment. In addition, the modules subject to various shading conditions over the day time (Harb et al., 2013; Islam et al., 2015; Schimpf and Norum, 2008). Therefore, string inverter configuration can be a solution for such applications due to dealing with only one string. In this manner, the power loss arising from module mismatches and partial shading can be reduced. Furthermore, conduction and switching losses are also minimized with reduced voltage and current ratings. The widely used string inverter is designed by using the single-phase H-bridge converter. Moreover, transformerless inverter topologies are also utilized for designing string inverters.

Transformerless inverter types have been popular for these inverter configurations. Transformerless topology has two major drawbacks. One of them is the leakage current and the other one being the lack of reactive power injection (Yang et al., 2019). In order to be used in smart PV systems, reactive power injection should be provided through the controller to fulfill the reactive power demand be fed into the utility-grid during fault transients.

2.1.2.3. Multi-String Inverters

In this configuration, each string possesses an individual DC-DC converter. In this manner, MPPT operation can be available for each string for increasing power generation capability. In addition, it is possible to provide flexibility to the system in terms of forming strings with a different number of PV modules and their alignments. Moreover, increased power levels can be obtained by string inverters. Price per watt attribution can be enhanced by increasing the power level. Moreover, reliability can be improved by extended input voltage operation range owing to operating at low irradiance level.

2.1.2.4. Central Inverters

Central inverters' power rating is remarkably high when compared to other inverter configurations. In most of the central inverter topologies, the DC-DC stage is eliminated for the sake of obtaining increased efficiency and reduced cost. Central inverters are generally designed three-phase and connected to the medium-voltage grid through an output filter and transformer. In some configurations instead of the two-level inverter topology, multi-level inverter topologies are utilized to increase the power level. Increased level of the output voltage contributes to the reduction of total harmonic distortion at the output current. In addition, the size of the output filter and voltage stress on power electronic components is reduced. For the purpose of providing the operation of PV modules at a maximum power point, the operation point should be adjusted continuously with respect to atmospheric conditions. However, in centralized inverters, it is not possible to achieve module-level MPPT. Therefore, a power loss occurs due to a power mismatch between PV modules and partial shading conditions (Yang and Blaabjerg, 2015).

2.2. Types of PV Systems

Renewable technologies are an absolutely indispensable opportunity for the whole world. Among the renewable sources, PV technology offers a key solution due to its unique features as mentioned in previous chapters. PV technology can be utilized for a broad range of applications, from small scale stand-alone systems to large scale utility grid-tied systems. Therefore it can be said that there are two fundamental system configurations namely stand-alone and grid-connected. Moreover, it is possible to see hybrid solar power systems applications.

2.2.1. Stand-Alone PV Systems

The stand-alone PV system operates independently of the utility grid. These systems are used to supply electricity to a connected load. These systems also consist of storage banks (e.g. battery banks) to provide electricity during the times of poor irradiance levels or also in the times without irradiance (Salas et al., 2006). Due to operating independently of other sources, these systems can be referred to as autonomous systems. The block diagram of a stand-alone PV system is demonstrated in Figure 2.6.

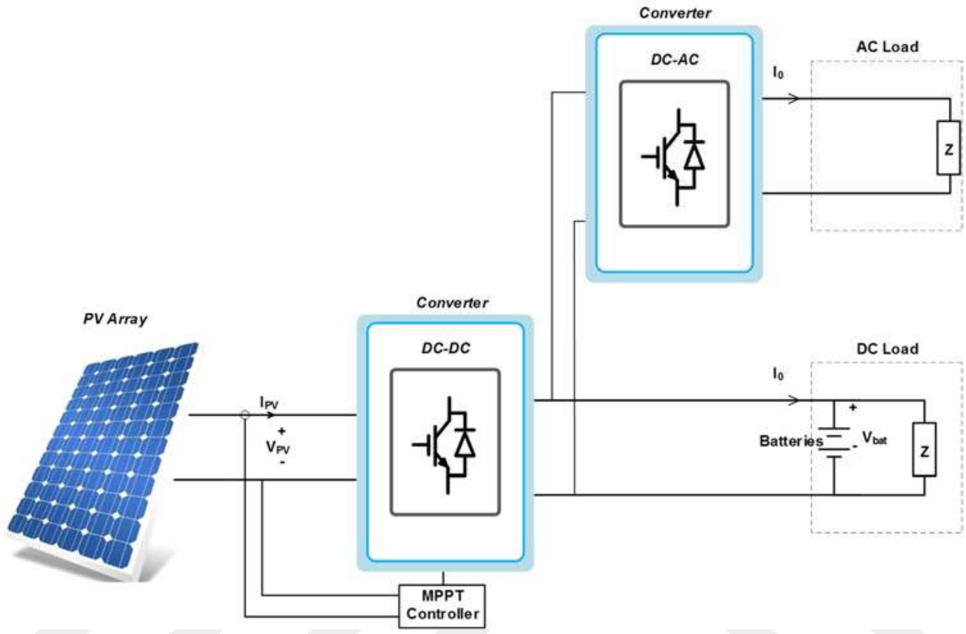

Figure 2.6. The block diagram of a stand-alone PV system

Due to operating independent of the grid, stand-alone systems can be indicated as autonomous systems. It is worth to point out that stand-alone PV systems fill the gap for people living in remote regions who do not have access to electricity. However, 1.3% of installed cumulative PV power in Europe is used to feeds the local load by operating as an off-grid system (Trujillo et al., 2016; Hasan et al., 2017).

2.2.2. Grid-Connected PV Systems

The grid-connected PV system is formed to operate in parallel with the electricity distribution system. They are mainly designed to provide electricity to the utility grid via a suitable inverter. Moreover, they can provide energy to power loads which can also be taken energy from the grid as demonstrated in Figure 2.7.

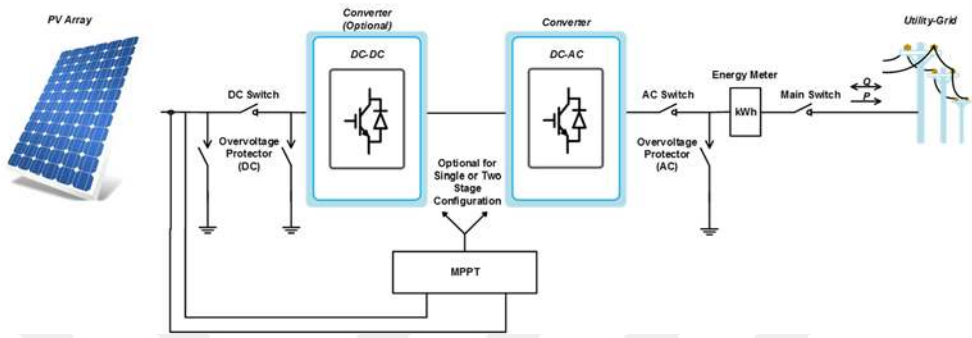

Figure 2.7. The block diagram of a grid-connected PV system

The popularity of grid-connected PV systems becoming higher over stand-alone PV systems. It is important to note that 98.7% of installed cumulative PV power in Europe is used to feeds the local load by operating as an off-grid system (Trujillo et al., 2016; Hasan et al., 2017). The cumulative installed capacity of grid-connected PV systems increasing day by day. However, the integration of PV systems into the electricity distribution system should be considered in detail (Foster et al., 2010). The growing integration of PV systems into the utility grid leading to new phenomena, which may eventually result in grid instabilities. From a technical point of view, inverters' controller structure should be improved for grid connection standards and codes which are determined by international standards organizations. Technical challenges aroused by the inherent nature of PV systems can be figured out by implementing various control functionalities that stated in the standards (Yang and Blaabjerg, 2019).

2.2.2.1. Grid Connection Standards and Codes

As discussed above, the integration of PV systems into the utility grid is increasing. Furthermore, development and technological innovation in PV systems make them more competitive in terms of installation costs. In this manner, technical challenges aroused in the utility grid by the inherent nature of PV systems will become more prominent in the future. The main issues in solar penetration in the distribution system are overvoltage during PV peak power generation, frequency deviation, and voltage fluctuation due to instantaneous power production decrement.

The specifications of the grid connection that have to meet the requirements according to being grid-interactive, stand-alone, or multiple mode inverters, stated in the standards defined by major international standardization organizations given below.

- IEC 61727 that determines the characteristics of the utility interface covers flicker, DC injection, harmonics and waveform distortion, Power factor, loss of utility voltage, over/under voltage and frequency, islanding protection and response to utility recovery.
- IEEE 1547 Standard for interconnection and interoperability of distributed energy resources with associated electric power systems interfaces,
- EN 50438 which, is the specific technical prescriptions regarding power-generating plants operating in parallel to the high-voltage or low-voltage distribution network with a maximum power ≤ 10 kVA,
- IEC 62109-1 that used in PV systems where a uniform technical level with respect to safety is necessary,
- IEC 62109-2 covers the particular safety requirements relevant to inverter products (This regulation must be used jointly with IEC 62109-1),
- EN 61000-6-1 for EMC immunity requirements applies to electrical and electronic equipment intended for use in residential, commercial, public and light-industrial locations,

- EN 61000-6-2 for EMC immunity requirements applies to electrical and electronic equipment intended for use in industrial locations,
- EN 61000-6-3 for EMC emission requirements applies to electrical and electronic equipment intended for use in residential, commercial and light-industrial environments,
- EN 61000-6-4 for EMC emission requirements applies to electrical and electronic equipment intended for use within the environment existing at industrial locations,
- EN 61000-3-2 deals with the limitation of harmonic currents injected into the public supply system. Limits for harmonic current emissions (equipment input current ≤16 A per phase),
- EN 61000-3-3 is concerned with the limitation of voltage fluctuations and flicker impressed on the public low-voltage system. Limits for voltage changes, voltage fluctuations and flicker in public low-voltage supply systems, for equipment with rated current ≤16 A per phase and not subject to conditional connection,
- IEC 62116 provides a test procedure to evaluate the performance of islanding prevention measures used with utility-interconnected PV systems.

Over/Under Voltage: The inverter has to operate between the voltages limits defined in the standards. When the grid voltage experienced fluctuations over/under the specified voltage limits the inverter must cease operating in determined maximum trip time as stated in Table 2.3 (IEEE1547, 2018; IEC61727, 2004).

Table 2.3. Over/Under voltage limits

Voltage	**Maximum trip time (sec)**
V < 0.5 x $V_{nominal}$	0.1
50% ≤ V < 85%	2.0
85% ≤ V < 110%	Unlimited operation
110% < V < 135%	2.0
135% ≤ V	0.05

Over/Under Frequency: The inverters have to operate between the grid frequency limits, which defined as the range of ±1 Hz in the standards. When the grid frequency experienced fluctuations over/under the specified frequency limits the inverter must be disconnected from the grid within 0.2 seconds (IEEE1547, 2018; IEC61727, 2004).

Current Harmonics: Harmonics distortions limits of currents and voltages defined in the standards. The maximum odd and even harmonic content limits of the inverter output current are specified in the standards. The limits for individual harmonics and THD are given in Table 2.4 (IEEE1547, 2018; IEC61727, 2004).

Table 2.4. Harmonic limits

Individual odd harmonic order h	**Percent (%)**
h < 11	4.0
11≤ h < 17	2.0
17 ≤ h < 23	1.5
23 ≤ h < 35	0.6
35 ≤h <50	0.3
THD	5.0

*Even harmonics are limited to 25 % of the odd harmonic limits above.

Power Factor: The lagging average power factor limit is determined to be higher than 0.9 for $P_{out} \geq P_{nominal} * 0.5$.

Reconnection after Trip: After a disconnection caused by abnormal conditions, the inverter can only reconnect when the normal voltage and frequency operation standards are provided.

2.3. Summary

Fundamentals of PV systems and inverters are introduced by providing a summary of related literature. The characteristic of PV modules and mostly known MPPT techniques are addressed in this chapter. The most important requirements for MPPT control of MIs are explained in detail. Moreover, MPPT techniques utilized in MI applications are explained by giving a review of related literature. The state-of-the-art PV converter technologies are highlighted. The main configurations of PV converters are categorized in four general headings and each configuration is clarified in detail. Furthermore, the PV system connection forms are provided. The requirements of the grid connection of PV systems stated in the standards defined by major international standardization organizations are provided in this chapter. The codes determined by the international standardization organizations are also explained in detail.

3. STATE-OF-THE-ART MI TECHNOLOGIES

This section presents the overview of MI technologies by providing a summary of related literature including Ph.D. theses and publications. MI configurations and control techniques are explained meticulously.

3.1. Topologies for Grid-Connected MIs

PV MIs consist of either single or two-power conditioning stages that predominantly influence the control structure and size of the decoupling capacitor. Single-stage power conditioning topology is designed to realize the MPPT task and grid connection requirements via a controller. In this topology, the DC-DC converter with a high capacity decoupling capacitor is cascaded with an unfolding H-Bridge inverter. H bridge inverter is responsible only for unfolding the rectified sine signal. Two-stage power conditioning topology differs from single-stage topology by operating principle and controller structure. The DC-DC converter is employed to achieve MPPT tasks and boosting the input PV voltage, while the DC-AC converter is utilized to transform output power to utility-grid by providing grid connection demands defined in regulations. Single-stage MIs are also named as MIs with pseudo DC-Link. The main reason for naming this way is originated from the placement of the decoupling capacitor. In this topology, a bulk decoupling capacitor is placed on the PV side and needed to realize both MPPT and the rectified sine based peak current control tasks. In two-stage topology, the DC link decoupling is utilized to injecting energy taken from DC-DC converter connected PV modules via an H-Bridge inverter. This topology is commonly known by the name as MIs with DC-link. It is possible to find extensive studies on single-stage and two-stage MIs in the literature. The results of these studies are published to show promising aspects of proposed power circuit topologies and controller structures. It can be concluded that the mentioned single-stage and two-stage MIs inherit merits and demerits of each other in terms of implementation cost, weighted efficiency, lifespan, controller functionality. These properties still required to be investigated in detail (Hu et al., 2012; Kavurucu, 2014).

3.1.1. Single-Stage MI Topologies

In single-stage topology, the main objectives are addressed to increase efficiency by modifying the operation principle and simplify the controller structure. The block diagram of single-stage MI is given in Figure 3.1. As can be seen from the block diagram MPPT task and peak current control process are achieved in one stage. The DC-DC converter is cascaded with an unfolding H-Bridge inverter that performs rectified current shaping operation.

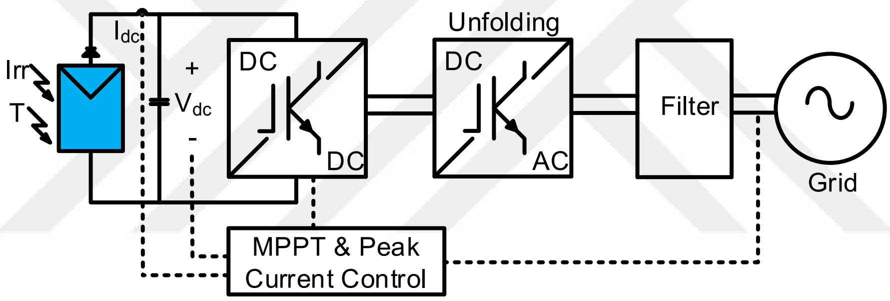

Figure 3.1. Block diagram of single-stage MI

Besides having various advantages particularly having a simple controller structure, the single-stage suffers from some drawbacks. The first drawback can be indicated as requiring a bulk decoupling capacitor that substantially affects the lifespan of the MI. Another one can be stated as the capacity of the decoupling capacitor that utilized at the input side of the converter. The main reasons for requiring bulk capacity are processing a rectified sine in grid frequency and low input voltage. Hence the studies in the literature are focused on proposing decoupling techniques to eliminate the utilization of bulk capacity capacitors (Hu et al., 2010; Hu et al., 2011). Moreover, the utilization of HF transformers to increase the input voltage to utility grid operating voltage magnitude constitutes issues such as power losses due to leakage inductance, large size, and high cost (Petreuş et al., 2013). Especially the leakage inductance based losses and resonance problems should be investigated in detail. In Table 3.1 a comparison of experimentally implemented single-stage MIs is presented by taking various performance parameters into account.

Table 3.1. Comparison of experimentally implemented single-stage MIs

Source	**Topology**	**Power Rate**	**Input Voltage**	**THD**	**Efficiency**
Hu et al., 2012	Three-port flyback	100W	60V	<1.7%	90.6%
Nayanasiri et al., 2013	Half-Wave Cycloconverter	100W	40V	-	-
Surapaneni and Rathore, 2015	CCM zeta converter	220W	30-48V	3.05%	93%
Fang and Ma, 2010	Coupled-inductor double-boost converter	260W	34.8V	<3%	>97.5%
Petreuş et al., 2013	Dual buck-boost converter	150W	100V	4.7%	93%
Zhang et al., 2013	Interleaved flyback converter	200W	36-60V	<5%	90.5-93.9%
Gao et al., 2014	Interleaved flyback converter	200W	36V	2.45%	>93%
Kim et al., 2014	Interleaved flyback converter	250W	22.7-33.3V	-	>95%

Table 3.1. Continue

Meneses et al., 2015	Multicore forward converter	120W	48.2V	<5%	92.4%
Hu et al., 2013	Flyback converter	100W	60V	<1.9%	>90%
Lai, 2014	Interleaved flyback converter	230W	29.67V	<5%	93%
Nanakos et al., 2015	Flyback converter	205W	31-40V	3.77%	>92%
Mazumder and Mehrnami, 2012	Cuk converter	-	-	-	>95%
Tsai et al., 2013	Full Bridge converter	350W	-	-	≈90%
Zhang et al., 2011	Flyback converter	120W	25-50V	<5.2%	83-94%
Edwin et al., 2014	Interleaved flyback converter	200W	-	<4%	95.7%
Morais et al., 2019	Cuk converter with switched-inductor	180W	30V	3.73%	92%

Hu et al. proposed an integrated three-port flyback topology as demonstrated in Figure 3.2. This topology is developed by adding a parallel switch to the conventional flyback converter. The main objective is to enhance the power decoupling capability of the converter. One port is assigned for the power decoupling, in this way the size of the decoupling capacitor is reduced. Key design considerations are determined as a predictive control strategy, and the DC voltage balance control across. A 100 W MI prototype is implemented. The peak efficiency of the system is obtained as 90.6% with THD <1.7% (Hu et al., 2012).

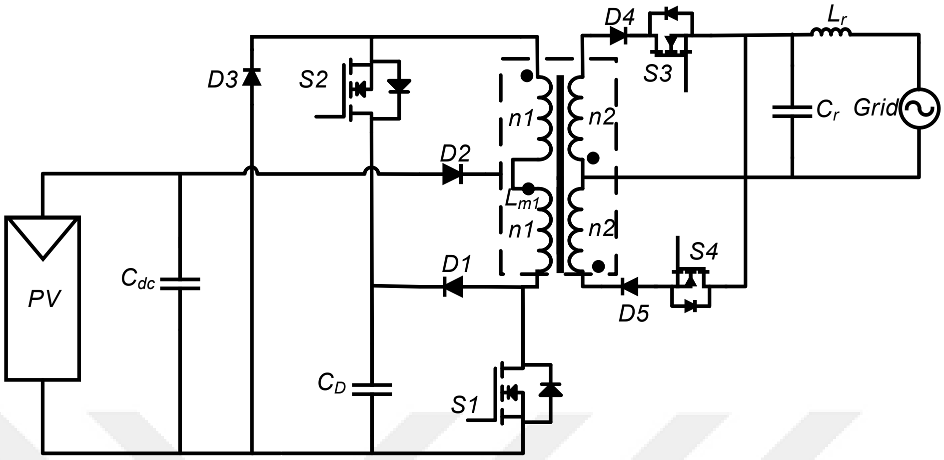

Figure 3.2. A three-port flyback for PV MI applications (Hu et al., 2012)

Nayanasiri et al. proposed a modified half-wave cyclo converter based MI with a decreased number of power conversion stages and a number of passive components as given in Figure 3.3. The switches are switched at zero voltage crossing in order to reduce switching losses. The output power of the inverter is controlled by using the phase shift modulation technique. The experimental implementation of the proposed topology is conducted by constructing a 100 W prototype (Nayanasiri et al., 2013).

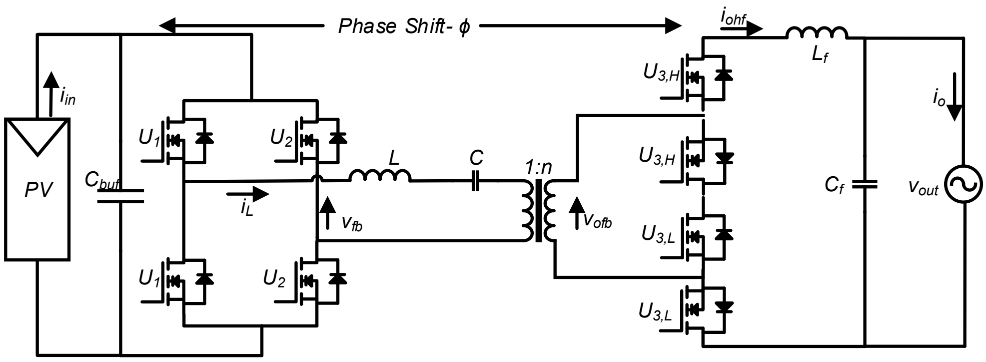

Figure 3.3. Half-Wave Cycloconverter-Based PV MI (Nayanasiri et al., 2013)

A single-stage zeta MI, which operates in CCM for a wide load range by Surapaneni and Rathore as shown in Figure 3.4. The proposed topology inherits promising aspects such as high efficiency, reduced current stress, and components' rating. An unfolding bridge whose switches operate at line frequency utilized for the secondary side of the converter. Also to verify the topology a 220 W laboratory prototype is implemented. Peak efficiency of 93% with THD 3.05% is obtained (Surapaneni and Rathore, 2015).

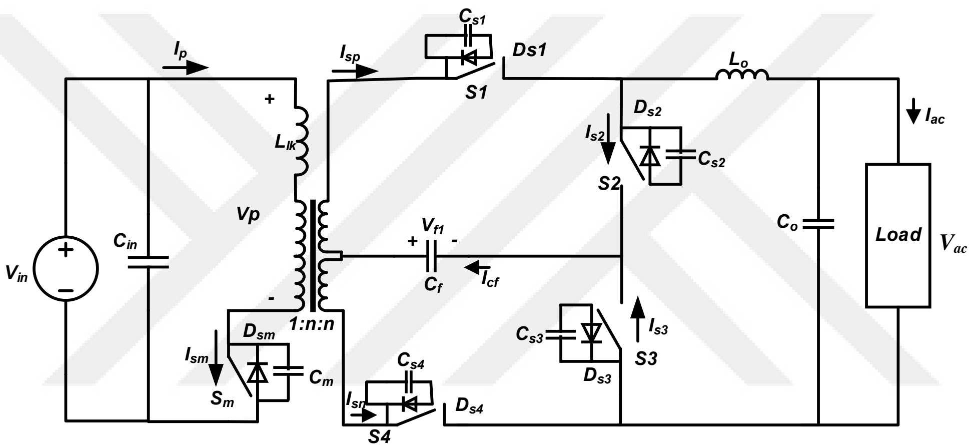

Figure 3.4. Single-Stage CCM Zeta MI (Surapaneni and Rathore, 2015)

Fang and Ma developed a coupled-inductor double-boost inverter for PV MI systems as shown in Figure 3.5. The developed converter has a high gain in order to generate output voltage larger than the input voltage. The gain of the system can be adjusted by the instantaneous duty cycle and turns ratio of the coupled inductor. A 220 W laboratory prototype is also designed to verify the performance of the developed converter. It is reported that the efficiency of the system is greater than 97.5%, THD is less than 3%, and a PF close to unity (Fang and Ma, 2010).

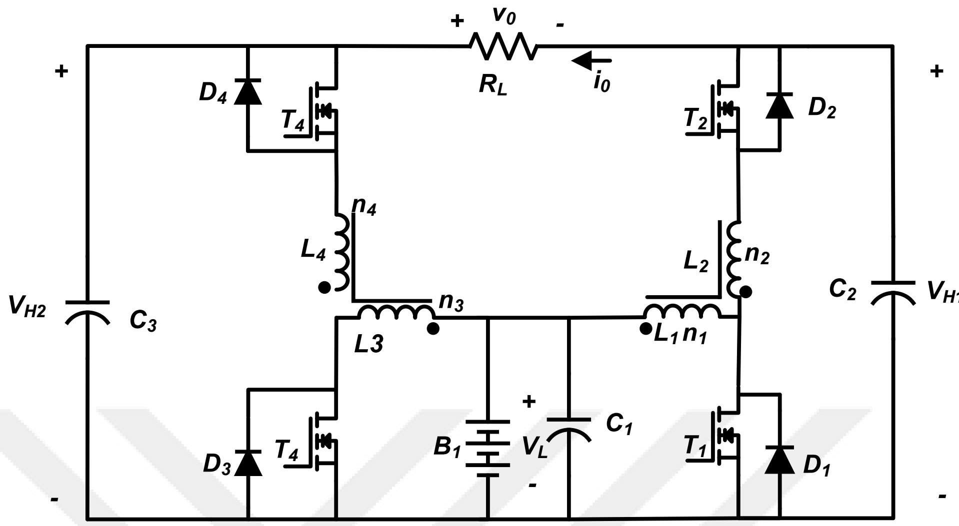

Figure 3.5. PV MI with Coupled Inductors and Double-Boost Topology (Fang and Ma, 2010)

Petreuş et al. applied a novel control and modulation technique dual buck-boost converter based single-stage MI. The developed control method can be a promising candidate for transformerless MIs. It is reported that the efficiency of the system is greater than 93%, THD is 4.7%, and a PF is 0.98 (Petreuş et al., 2013). Zhang et al. proposed a novel hybrid optimal control method for PV MIs. The main objective is to obtain remarkable efficiency in a wide load range. The BCM and DCM control strategies are also analytically investigated in order to perform a loss analysis. An experimental prototype is constructed to validate the proposed control method. The power of the constructed system is 200 W. The efficiency of the system varied from 90.5% to 93.9% with THD less than 5% (Zhang et al., 2013). Gao et al. investigated the operating mode of the flyback converter. The operating modes are analyzed in terms of power level, complexity level, efficiency, and switching frequency bandwidth. It is concluded that BCM is more powerful with regard to DCM and CCM with regard to having a higher power level, higher efficiency, and wide switching frequency bandwidth. It is also reported that the efficiency between 93-94% and THD is 2.45% for a 200 W implemented prototype (Gao et al., 2014).

Kim et al. proposed a control method to increase the weighted efficiency of an interleaved flyback inverter. The main contribution of synchronous rectifier is categorized in respect of the voltage spike across the main switch in order to control the operation of the active clamp circuit. It is reported that the efficiency of the system is greater than 95% for a 250 W prototype (Kim et al., 2014). Meneses et al. developed a primary-parallel secondary series multicore forward PV MI. The proposed MI topology is operated in DCM with off-time boundary mode control. It is reported that the efficiency of the system is greater than 92.4% with THD less than 5% for a 120 W prototype (Meneses et al., 2015). Hu et al. proposed a novel topology for PV MIs by detaching the decoupling capacitor thanks to an additional switch. In this way, the capacity of the power decoupling capacitor is reduced. Thus utilization of film capacitors is provided in order to expand the lifespan of MIs. Also to verify the topology a 100 W laboratory prototype is implemented. Peak efficiency of 91.5% with THD 1.09% is obtained (Hu et al., 2013). Lai presented an interleaved flyback converter based single-stage MI. A 250 W MI prototype is implemented. The maximum conversion efficiency of the system is obtained as 93% with the THD <5% (Lai, 2014). Nanakos et al. presented a flyback converter based MI operating in improved boundary conduction mode (BCM). The analytical equations are derived for BCM operated flyback MI. Experimental verification of the presented model is conducted. The European efficiency of about 91.5% with THD of the output current 3.77% is obtained for a 205 W prototype (Nanakos et al., 2015). Mazumder and Mehrnami perform the design and analysis of two isolated Cuk converters operating differentially to constitute a sinusoidal output. The cost and size of the PV MI are reduced (Mazumder and Mehrnami, 2012). Tsai et al. developed a symmetric phase-shift modulation technique with the aim of realizing the zero voltage switching function. A PV MI topology based on a full-bridge converter with a resonant tank is designed. A 350 W prototype is constructed and the overall system efficiency is about 90% is obtained (Tsai et al., 2013). Zhang et al. analyzed the effect of the boundary conduction mode control and switching frequency on the efficiency. A 120

W experimental setup constructed. It is concluded that the efficiency of the system can be increased by 2~5% compared with the constant switching in DCM (Zhang et al., 2011). Edwin et al. focused on the control issues of interleaved flyback converter based PV MI systems operating in CCM. They performed a detailed dynamic analysis for modeling and control of interleaved flyback based PV MI. In this manner, a two-step controller design methodology is developed for interleaved flyback converter based PV MI systems operating in CCM. A 200 W prototype is implemented. The peak efficiency of 95.7% is obtained. The measured current THD values are less than 4% (Edwin et al., 2014). Morais et al. proposed a high static gain DC-DC converter. The proposed converter is performed by the combination of the Cuk converter with the switched-inductor technique. The DCM and CCM operation of the proposed converter is analyzed. A 180 W MI prototype is implemented. The efficiency of the system is achieved as 92% with the THD value of 3.73% (Morais et al., 2019)

3.1.2. Two-stage MI topologies

Two-stage MI topologies are constituted by utilizing a DC-DC converter integrated with a DC-AC inverter as depicted in Figure 3.6. Two-stage MIs presents more flexible control when the demands of smart PV systems considered. However, the control complexity of these systems constitutes challenges.

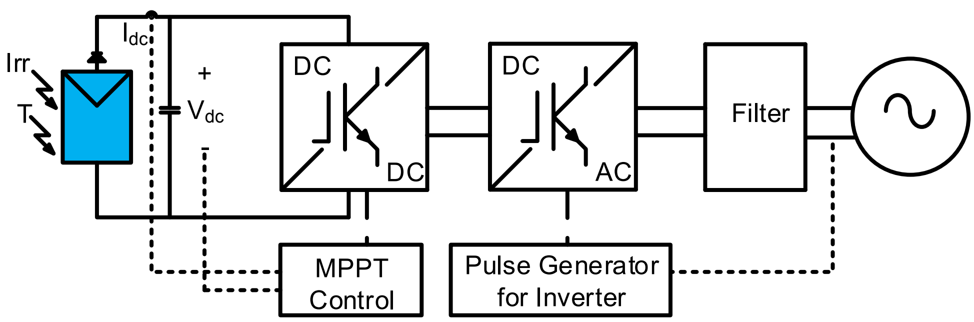

Figure 3.6. Block diagram of two-stage MI

The control of this topology can be thought of as two separate structures. The control of the DC-DC stage is in charge of performing the MPPT task. Moreover, the DC-DC converter fulfills the increment of input PV voltage. On the other side, the control of the DC-AC stage mainly deals with providing the grid requirements such as compensation of harmonic content, low voltage ride through, dynamic grid support, and anti-islanding. Due to having high voltage level across the DC link capacitor, reduces the capacity of decoupling capacitor (Hasan et al., 2017; Celik et al., 2018). The wide input operating voltage range could be indicated as a significant advantage of the two-stage MIs. Enhancing lifespan, reducing implementation cost, efficiency rate, and control flexibility are also expressed as the main technical challenges of the two-stage MIs. In view of these, researchers explored different power circuit topologies and control structures to overcome the main technical challenges. A comprehensive review of related literature including publications is conducted and the comparison of experimentally implemented two-stage MI is presented in Table 3.2.

Table 3.2. Comparison of the experimentally implemented two-stage MIs

Source	Topology	Power Rate	Input Voltage	THD	Efficiency
Jiang et al., 2012	A boost-half-bridge DC-DC converter cascaded with full-bridge inverter	210W	30-50V	2.87%	97.0–98.2%
Trujillo et al., 2016	A push-pull converter cascaded with full-bridge inverter	200W	21-36.5V	-	-
Zhang et al., 2014	LLC converter cascaded with an inverter	300W	31.25V	-	-
Ahmed et al., 2013	Inductor boost converter cascaded with full-bridge inverter	120W	30V	-	>90%
Hasan and Mekhilef, 2017	Flyback converter cascaded with a resonant full-bridge inverter	250W	40-60V	3.71%	95.9%
Arshadi et al., 2016	A single-switch high step-up Converter cascaded with half-bridge inverter	150W	25-55V	<3.5%	94.6%
Surapaneni et al., 2016	Cyclo-converter based double-ended MI	250W	30-48V	-	>93%
Evran, 2017	A high step-up converter cascade with full-bridge inverter	300W	25-32V	1.25%	94.6%
Roy et al., 2019	Three-phase EDR boost cascaded with doubly grounded voltage swing inverter	300W	35V	-	94.09%
Kan et al., 2019	Flexible DC-DC converter cascaded with full-bridge inverter	300W	36V	<1.5%	93.33-93.58%

Jiang et al. presented a PV MI topology that composed of a boost half-bridge DC-DC converter with a conventional H-bridge inverter as exhibited in Figure 3.7.

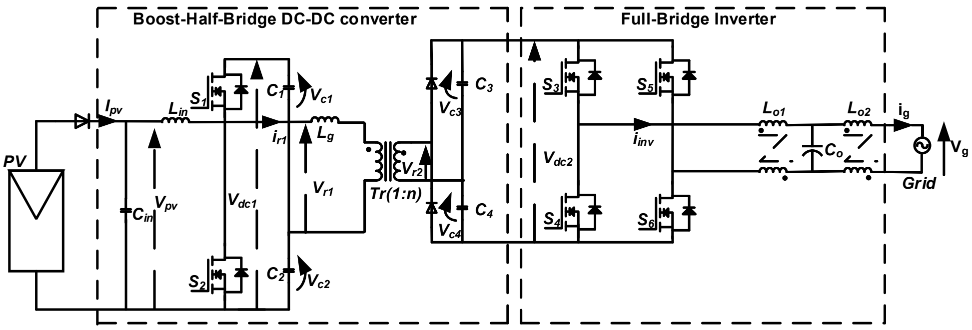

Figure 3.7. A boost half-bridge DC-DC converter with a conventional full-bridge inverter (Jiang et al., 2012)

A plug-in repetitive current controller based on a fourth-order linear phase IIR filter is developed to control the injected grid current. The promising aspects of the proposed controller can be expressed as ensuring a high power factor with reduced THD, fast dynamic response, and operating within a wide range of load conditions. Experimental results of the 210 W setup shows that power factor higher than 0.99, THD from 0.9% to 2.87%, and efficiency between 97.0% and 98.2% are achieved (Jiang et al., 2012). Trujillo et al. presented the characteristics, design and control parameters of a PV MI consists of a push-pull converter cascaded with a full-bridge inverter as shown in Figure 3.8. An average current controller is utilized to control the current injected to the grid. The presented PV MI system is implemented experimentally by constructing a 200W prototype (Trujillo et al., 2016).

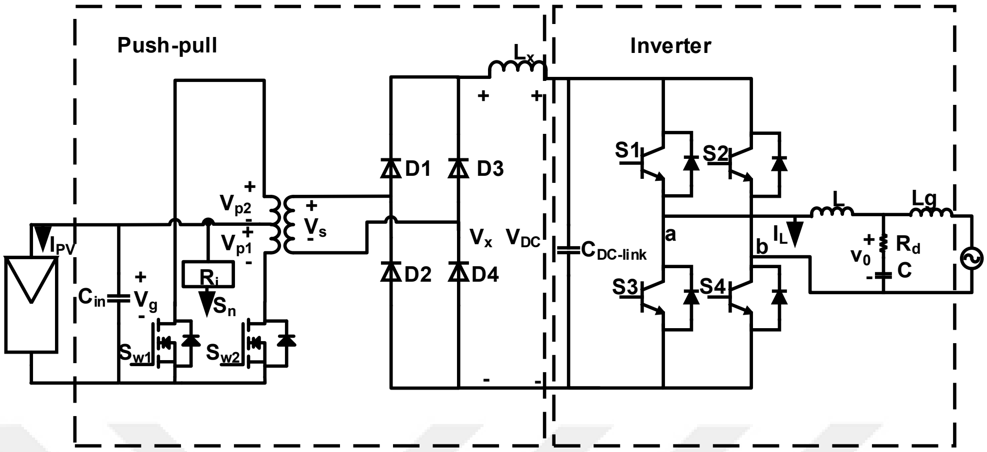

Figure 3.8. A push-pull converter cascaded with a full-bridge inverter (Trujillo et al., 2016)

Trujillo et al. also presented the modeling and control of a push-pull converter based two-stage PV MI operating in island mode by conducting a simulation study. The simulated system does not require additional storage battery banks. A modified control structure that regulates input and output voltages simultaneously in order to provide islanding mode (Trujillo et al., 2011). Zhang et al. proposed a novel center point MPPT technique for a two-stage PV MI. The presented two-stage MI consists of an LLC converter and a full-bridge inverter as shown in Figure 3.9. The presented PV MI system with the proposed MPPT technique is verified thanks to a constructed 300 W prototype (Zhang et al., 2014).

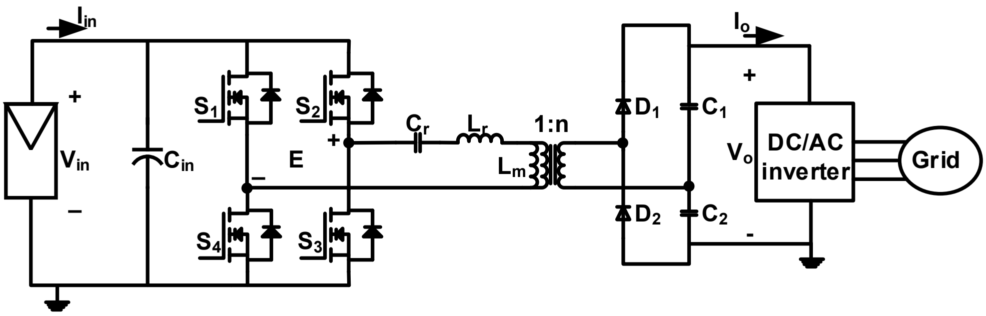

Figure 3.9. An LLC converter cascaded with a full-bridge inverter (Zhang et al., 2014)

Ahmed et al. proposed a novel two-stage PV MI topology composed of a high gain-switched inductor boost with a current shaping circuit connected to a full-bridge inverter. The developed system demonstrates promising features such as high boosting gain, lower switching losses, and reduced ground leakage current. A 120 W prototype is constructed to validate the system. Experimental results revealed that the efficiency of the system is higher than 90%. Hasan and Mekhilef proposed a high efficient two-stage PV MI that comprises a flyback converter with an active clamp circuit and a resonant full-bridge inverter. The switching losses are minimized by zero voltage switch turn on and turn-off of main switches. Hence, the efficiency of the system is increased reasonably. An experimental setup is implemented. It is reported that the CEC efficiency of the system is 95.9% and THD is 3.71% for a 250 W prototype (Hasan and Mekhilef, 2017). Arshadi et al. proposed a novel topology for two-stage PV MI applications. The proposed topology composed of the single-switch high step-up converter and conventional half-bridge inverter. Negative grounding of the PV module provides a remarkable reduction of ground leakage current. The leakage inductance energy is reutilized with the help of a passive regenerative clamp circuit. The zero current switch turn on ensured to increase efficiency. In addition, the proposed topology draw attention with the features of simple structure, reduced number of switches, easy control, and increased efficiency. Also, an experimental set is implemented to validate the features of the proposed topology. The maximum efficiency is 94.6% and THD is below 3.5% for the constructed 150 W prototype (Arshadi et al., 2016). Surapaneni et al. proposed a novel half-bridge cycloconverter configuration for two-stage PV MI applications. The double-ended configurations are designed without any dc link. Conventional full-bridge converter, half-bridge converter, and push-pull converter employed to constitute primary stage, where a half-bridge cyclo-converter operating at line frequency is used in the secondary side. The main advantages can be expressed as a reduced number of components and switching losses. The performance of the developed configuration is validated through an experimental setup. The efficiency of the system is reported as greater than 93% for a 250 W system. Evran presented a PV MI system composed of a high step-up Z-source-based converter and full-bridge inverter. A plug-in repetitive controller is proposed to obtain reduced THD. The performance of the developed system is evaluated through a 300 W prototype. The efficiency of the system is obtained as 95.3% at full load. The THD between 1.25% and 2.65% with a power factor greater than 0.9 are obtained (Evran, 2017). Roy et al. proposed a transformerless converter topology for two-stage PV MI applications. The proposed topology comprises a high-gain converter and a doubly grounded dynamic dc-link inverter. Three main features of the developed system including high-gain of the converter, reduced common-mode leakage current and decreased the capacity of power decoupling capacitor are crucial. The proposed system is evaluated by constructing a 300W prototype. The efficiency of the system is measured as 94.09% (Roy et al., 2019). Kan et al. proposed a novel power circuit topology for PV MI topologies. The proposed topology is composed of a pre stage-flexible DC-DC converter and standard full-bridge inverter. The pre-stage DC-DC converter composed of a full-bridge converter, a buffering inductance, a high-frequency transformer, and a full-wave rectifier. The developed converter behaves like a current source and can be connected to a single flexible converter without requiring extra equipment. A 300 W prototype is implemented. The CEC efficiency from 93.33 to 93.58% is obtained. The measured current THD values are less than 1.5% (Kan et al., 2019).

3.2. DC-DC Converter Topologies for MIs

In this part, the mostly employed converter types in two-stage PV MI applications are reviewed. The basic design considerations of these converters are also provided by giving the equations. The power processing capability of the converter will directly affect the efficiency of the overall system. In addition, the size and implementation cost of the system will demonstrate differences according to the utilized converter type. Moreover, the MPPT technique is essential to extract maximum power from the PV module. Therefore DC-DC converter and the MPPT as its control algorithm will directly contribute to the efficiency of the PV MI. It is worth to point out that some researches revealed that the MPPT technique should be compatible with the utilized DC-DC converter. In this manner, Zhang et al. proposed a center point iteration MPPT that inherits the property of variable perturbs in frequency. The proposed MPPT technique able to cope with the variable frequency modulation for resonant converters (Zhang et al., 2014). On the other hand, decoupling capacitors are constituted crucial issues in terms of MIs' lifespan. The decoupling capacitor capacity can be reduced by modifying the circuit topology of the converters. It can be concluded that parameters such as galvanic isolation, power capacity, gain interval, and the number of components is crucial to choose a proper topology for the PV MI systems (Choi, 2013; Khosrogorji et al., 2016). With this background, an overview of DC-DC converters commonly utilized in PV MI applications is carried out by providing a summary of technical properties.

3.2.1. Flyback DC-DC Converter

Flyback converter can be shown as the mostly utilized converter topology for the PV MI applications. This converter can be stated as the modified version of a buck-boost converter. A transformer that behaves like an inductor is utilized instead of the inductor. In this manner, the voltage gain of the converter can be increased when compared to the buck-boost converter. Also including only one switch that driven with respect ground provides easy implementation features. In PV MI applications flyback converters are utilized as the front end converter to increase the input voltage, providing MPPT operation, and ensuring galvanic isolation. Hence, the flyback converter attracts the most attention for PV MI applications by additional features such as a minimized number of components and flexible power range. It is crucial to point out that the flyback converters need modifications in order to deal with high switching loss and switching stress resulting from the leakage inductance of the transformer (Kazimierczuk, 2008; Nanakos et al., 2015). An interleaved flyback converter based PV MI is demonstrated in Figure 3.10.

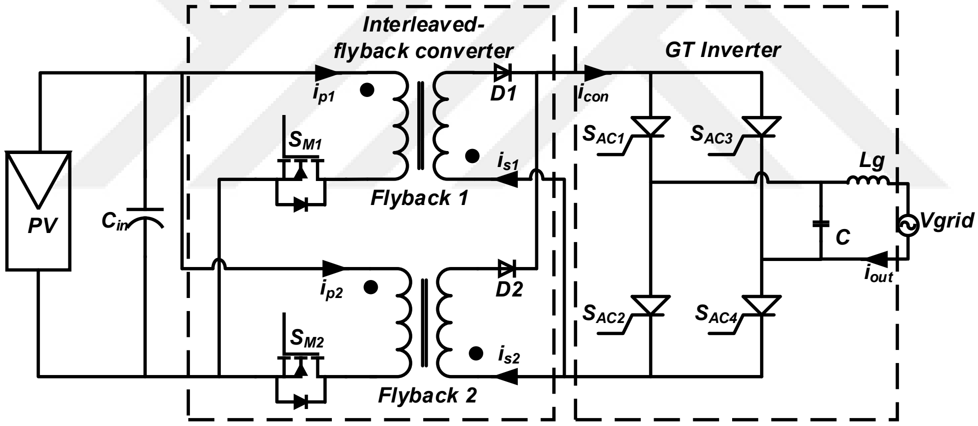

Figure 3.10. An interleaved flyback converter based PV MI (Gao et al., 2014)

The voltage gain of the converter can be derived as follows

$$\frac{V_o}{V_i} = n\frac{D}{(1-D)}$$

where V_o, V_i, D, and n indicate the output voltage, input voltage, duty cycle and turn ratio of the transformer, respectively.

The magnetizing inductance of the converter can be found through

$$L_m = \frac{n^2 V_o (1-D_{min})^2}{2 f_s I_{omin}}$$

where L_m, f_s, and I_o are the switching frequency, magnetizing inductance, and output current, sequentially.

The output capacitor of the converter for filtering can be calculated as

$$C_{min} = \frac{D_{max} V_o}{f_s R_{min} \Delta V_o}$$

where ΔV_o is the maximum permitted ripple rate of output voltage and R_{min} is the output load.

In order to reduce the I^2R loss and increase the power range of the converter interleaved topology can be utilized. In addition to these advantages EMI, the leakage inductance of the transformer can be reduced, and ripples on the current can be also reduced. In this topology, the switches are switched with a 180° phase shift relative to each other (Edwin et al., 2014; Lai, 2014).

3.2.2. Push-Pull DC-DC Converter

Push-pull converter, which demonstrated in Figure 3.8 can be considered a modified version of the buck converter. This type of converter also inheriting the easy implementation feature by utilizing two switches with respect to the ground. This converter differs from the flyback converter due to being employable for higher power levels. The push-pull converter shows reasonable properties in terms of reduced input current ripples for the medium power applications that required galvanic isolation (Trujillo et al., 2016). When the full-bridge converters are considered, the push-pull converter shows the advantage of the reduced number of switching components. Furthermore, the push-pull converter does not require a capacitive input voltage divider that carrying high RMS currents when compared to the half-bridge converter (Trujillo et al., 2011). On the other hand, high voltage stress of switches, risk of core saturation due to dc current flow in primary of the transformer should be taken into account (Kazimierczuk, 2008). It should be noted that the switches of the push-pull converter are triggered 180° out of phase with respect to each other. The duty cycle of the converter should be under 0.5.

The voltage gain of the converter can be derived as follows

$$V_o = \frac{V_i 2D}{n}$$

where V_o, V_i, D, and n indicate the output voltage, input voltage, duty cycle and turn ratio of the transformer, respectively.

The minimum magnetizing inductance of the converter in CCM can be found through

$$L_{min} = \frac{R_{Lmax}(0.5-D_{min})}{2f_s}$$

where L_m, f_s, and R_{Lmax} are the switching frequency, magnetizing inductance, and maximum output load, sequentially.

The output capacitor of the converter for filtering can be calculated as

$$C_{min} = \frac{D_{max}}{2f_s r_c}$$

where r_c is a series resistance of the capacitor.

3.2.3. LLC DC-DC Converter

LLC resonant converters, which demonstrated in Figure 3.9 can be expressed as the commonly utilized resonant converter structure. They are also recognized with the name of the series-parallel resonant converter. A capacitor, an inductor, and transformer magnetizing inductance are utilized to form the resonant tank (Chen at al., 2014; Zhang et al., 2014). The LLC resonant converter draws attention due to having a wide input voltage operating range, the reduced voltage stress on the output diodes, and reduced switching loss. When the converter topologies given above considered the leakage problem constitutes a crucial problem. However, LLC resonant converter topology inherently employs the leakage inductance as a resonant element. Hence, the switching losses are significantly reduced. Moreover, the utilization of the series capacitor provides DC current blocking, which causes the transformer core saturation. The relation between the input voltage and switching frequency should be carefully adjusted in terms of the voltage gain controllability. Besides having the advantages, LLC resonant converters demonstrate various drawbacks in the sense of design complexity. It is hard to provide a balance between the load and voltage gain. Moreover, it is complicated to derive an exact operation analysis due to having various characteristics in a switching cycle. The correlation between the input voltage and frequency is nonlinear. The variation of frequency in a broad range makes these resonant converters more complex. The design of the resonant tank's inductor and capacitor should be considered carefully due to being possible to find a range with the existing methods (Fang et al., 2013).

The basic design equations are given as the following

The input voltage V_{in}, output voltage V_o, output current I_o, resonant frequency f_r, efficiency η, hold uptime T_h and the output capacitor C_o are determined as marked values. An initial value is specified as resonant factor "m".

$$m = \frac{L_m + L_r}{L_m}$$

where m, L_m, and L_r express resonant factor, magnetizing inductance, and resonant inductance, respectively.

The input power and minimum input can be calculated as

$$P_{in} = \frac{V_o I_o}{\eta}$$

$$V_{in\_min} = \sqrt{V_{in\_nom}^2 - \frac{2P_{in}T_h}{C_o}}$$

where the output voltage is V_o, the output current is I_o, the resonant frequency is f_r, efficiency is η, hold up time is T_h and the output capacitor is C_o.

The maximum voltage gain can be found as

$$M_{max} = \frac{V_{in\_nom}}{V_{in\_max}} M_{nom}$$

where the nominal voltage gain M_{nom}=1, M_{max} is the voltage gain.

Transformer ratio is defined as

$$n = \frac{V_{in\_nom}}{2(V_o + V_f)} M_{nom}$$

where V_f is the voltage drop of the secondary side.

The load factor of the LLC converter can be derived by using

$$Q = \frac{\sqrt{L_r/C_r}}{R_{eff}}$$

The effective value of the load factor can provide the required peak gain. Then, we can calculate the C_r, L_r and L_p as follows

$$C_r = \frac{1}{2\pi Q f_r R_{eff}}$$

$$L_r = \frac{1}{(2\pi f_r)^2 C_r}$$

$$L_p = mL_r$$

3.3. Control Modes of DC-DC Converters

The PV MIs must be formed to attain maximum power from the modules. Operation at low power levels constitutes the efficiency problems when the parts of the overall system are considered. Therefore, the DC-DC converters take on an important task with MPPT control techniques with regard to efficiency. For the purpose of realizing this task DC-DC converters are maintained to operate by driving a reference current or voltage value determined by the MPPT technique. The voltage and current values on the PV side are measured and filtered out via filters with the purpose of suppressing the noises on the measured signals. The reference signal created by the MPPT algorithm is compared with the measured value on the PV side and the resulting error signal is passed through a controller to carry the operating point of the module to that optimal value. To realize the operation at maximum value and reduce the error between the actual and reference value, the switch of the converter is triggered in the specified switching frequency. The DC-DC converters can be controlled in two main control modes namely current-mode control and voltage-mode control. These control modes present various advantages and disadvantages in terms of transient response, stable modulation, and noise tolerance. The pros and cons of these control modes are discussed below.

3.3.1. Current Mode Control

The current-mode control in other saying current-injected control which demonstrated in Figure 3.11 composed of an inner current loop and an outer voltage loop (Kazimierczuk, 2008). The current-mode control can be stated as the revised form of the voltage-mode control and operates as a sample-and-hold circuit.

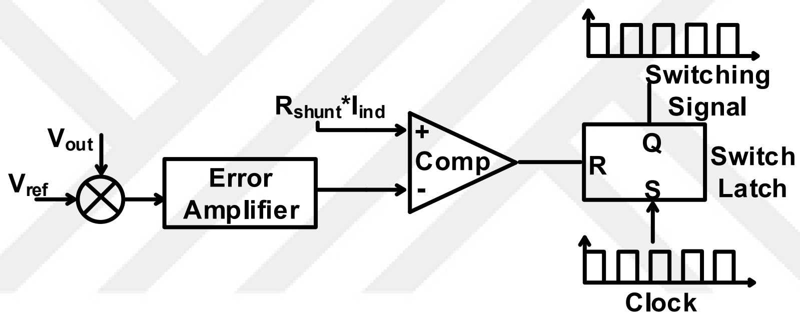

Figure 3.11. Current mode control

The inner control loop is in charge of the adjustment of the duty cycle while the outer voltage loop produces a reference value for the current loop. The current mode control presents various advantages such as high bandwidth, fast dynamic response, and stable operation of feedback. Moreover, this control mode presents the over-current protection inherently. On the other hand, separate voltage and current feedback loops render the control circuit complex (Mammano, 1995).

3.3.2. Voltage Mode Control

The voltage mode control responsible for the adjustment of the duty cycle to obtain the desired voltage value through a single loop as demonstrated in Figure 3.12.

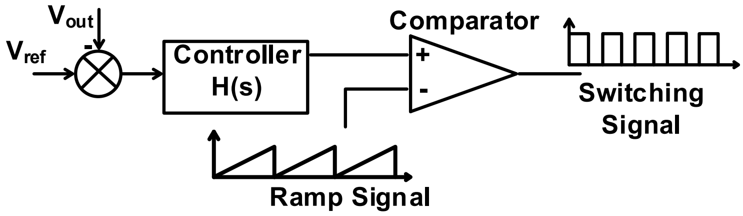

Figure 3.12. Voltage mode control

It can be indicated as the basic form of the control mode. It should be noted that this control mode has an extensive utilization area in PV converter applications. The complexity level of the voltage-mode control is low and makes the analysis of the circuitry easier when compared to current-mode control. In addition, providing stable modulation and high noise tolerance can be shown as the promising aspects of this control mode. However, the dynamic response of this control mode is slow when compared to current-mode control (Mammano, 1995).

3.4. Commercial MI Topologies

A brief summary of the technical specifications of commercially available MIs is provided in Table 3.3. These technical specs are derived from the datasheets provided by the manufacturers. It can be concluded that the operating voltage range of the MIs is mostly varied between 25 V and 45 V with the DC power range from 200 W to 300 W. Efficiencies of the commercially available MIs are also higher than 92%. Most of them do not inherit the dynamic grid support property. When considering the state-of-the-art, there is no requirement of dynamic grid support for the low voltage level. However, the dynamic grid support in low voltage grids becomes necessary, when the high penetration of distributed generation to the low voltage grid is considered.

Table 3.3. The technical specifications of commercially available MIs

	Max. DC Power	Max. Input Voltage	MPP Voltage Range	Power Factor	Efficiency	Dynamic Grid Support
SMA SB240-10	245W	45V	23-32V	1	95.9%	No
AEConversion INV250-45	250W	45V	20-40V	> 0.99	93.5%	No
ABB Micro-0.25-I-OUTD	300W	65V	25-60V	0.95	96.5%	No
Enphase S230	230W	48V	27-37V	1	97.2%	Yes(0.7 leading right through to 0.7 lagging)
Sparq 190W	240W	65V	32-50V	0.99	95%	No
Darfon MIG280VD00	280W	60V	-	0.95	95.5 %	Reactive power control through web monitoring
CP-250-60-208/240-MC4	250W	40V	22-37V	-	96.6%	No
Zhejiang Envertech EVT 248	248W	54V	24-42V	0.99	95.6%	No
YC250-NA	310W	55V	22-45V	0.99	95.5 %	No
WVC - 300	300W	50V	22-50V	0.96	92.3%	No
SOFAR MICRO250	250W	60V	27-45V	0.99	96.2%	No
Shinewise220W	240W	60V	25-45V	0.97	97.5%	No
Suncon SC-MAC250A	260W	50V	24-40V	0.99	95.2%	No
Omniksol-M300	310W	60V	27-48V	0.99	96.3%	Yes
LS250-AU	250W	60V	27-45V	0.99	96.2%	No
RSMI-250L	260W	55V	22-45V	0.99	95.5%	No
Invo250	250W	50V	28-40V	0.99	95.8%	No
SBT-250 WF	270W	60V	20-50V	0.99	94.3%	No
MAC250A - Europe	260W	50V	24-40V	0.99	95.2%	-
MKPV-N200	200W	60V	30-54V	0.99	95%	-

3.5. Summary

In this chapter, the state-of-the-art MI technologies are investigated meticulously. Designed topologies for grid-connected MIs and their controllers are explained rigorously. A detailed literature survey of MIs is conducted by providing a summary of related literature including Ph.D. theses and publications. Commercially available MIs are examined and their technical details are tabulated.

4. DESIGN AND IMPLEMENTATION OF DEVELOPED PV MI

This section introduces the design and implementation of designed MI by providing information about the utilized power circuit and control strategy. The proposed MPPT technique and improved closed-loop control structure are explained in detail. Furthermore, the experimental design procedure and PCB design of the overall system are provided rigorously. The selection of ICs for control system design and their simulations, which performed by using an analog electronic simulation program, is explained meticulously.

4.1. Circuit Description and Operation Principles of Developed PV MI

A two-stage conversion topology is selected to construct MI. The selected power circuit topology includes a quasi-resonant interleaved flyback converter operated in discontinuous conduction mode (DCM) and a full-bridge inverter. The block diagram of the constructed two-stage grid-connected PV-MI system is demonstrated in Figure 4.1. In the first stage, the interleaved flyback converter is employed to achieve the MPPT task and boost the input PV voltage. The power from the PV module (260 W @ 35 V) is transferred to the DC-AC converter with an increased voltage value. The losses of the flyback converter are minimized by switching at zero voltage crossing.

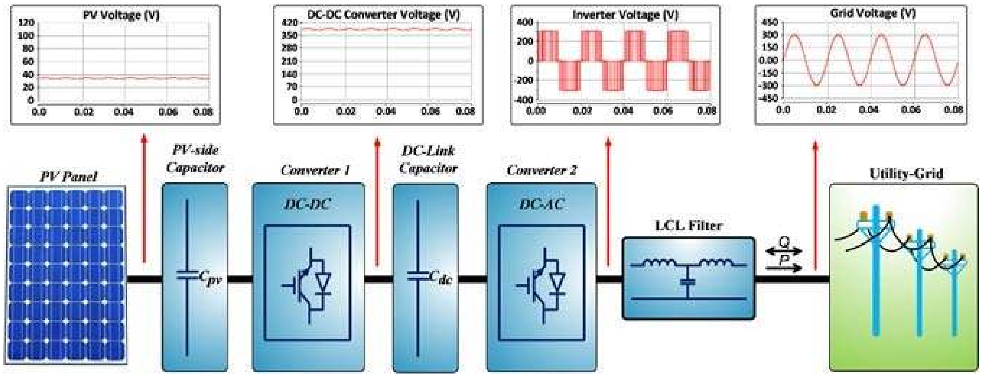

Figure 4.1. Block diagram of the two-stage grid-connected PV-MI system

It is worth noting that the determination of operation mode is a significant criterion for the design procedure of the flyback converter as it affects transformer size, switching stress, efficiency, and power quality parameters (Çelik et al., 2018). Operation in DCM can ensure a high-efficiency rate when compared to operation in boundary conduction mode (BCM) (Zhang et al., 2013). The transformer size becomes smaller due to requiring a smaller inductance value. From the standpoint of the peak value of the magnetizing current, it potentiates the switching stress of the switch that causes push up in the switching loss, copper loss, and transformer winding loss. Nevertheless, DCM operation puts forward the advantage of zero current turn-offs of output diodes, which abolishes the reverse recovery problems of output diodes. It is important to emphasize that the DCM operation eliminates the right half-plane (RHP) zero that poses a problem in the stabilization of the control loop for a wide range of operation voltage (Neshaastegaran and Kashenas, 2013; Nanakos 2015). On the other hand, the favorable design of the flyback transformer will precisely exert an influence overall design of the converter. The flyback transformer essentially behaves as an energy storage component. From the perspective of the operating logic of the flyback converter, energy is stored in the air gap of the core when the main switch is on, whereas the stored energy is transferred to the outputs when the main switch is off. In the flyback configuration, the current does not go through the transformer windings at the same time. This is the main reason why the transformer is considered as an inductor (Adams, 2001). High power flyback transformers require a large air gap, which results in the reduction of permeability and magnetizing inductance with the increased primary magnetizing current. It should be noted that a large air gap causes more leakage flux that raises the electromagnetic interference (EMI) (Hurley and Wölfle, 2013). Interleaved flyback topology can be an efficient solution for the high power applications in terms of the elimination of the aforementioned problems. The control of the converter for PV applications can be realized by using the MPPT technique to attain maximum power from PV modules regardless of atmospheric conditions (Salam et al., 2013). A controller with a proportional gain and an integrator is utilized to provide the appropriate switching signal for tracking the reference value generated by the MPPT block. An approximate parameter region is derived by observations to satisfy the required closed-loop control performance (Çelik and Teke, 2017).

4.2. Implementation of DC-DC Converter

The interleaved quasi-resonant flyback converters, which comprises two flyback converter in parallel, are utilized. Two high-frequency power switches, two high-frequency transformers, two secondary fast recovery diodes, and an input capacitor are utilized for implementation. The analysis of the converter is realized for one switching period. The DCM operation mode is selected for presenting the salient features such as the elimination of RHP zero that causing challenges to stabilizing the control loop, fast dynamic response, alleviation of diode reverse recovery problem, and reduction of switching loss (no turn-on loss). With this motivation, the flyback converter operated in DCM mode is designed by using the following analytical expressions.

4.2.1. Selection of Magnetizing Inductance

The operation mode of the converter directly has an influence on the selection of the magnetizing inductance of the converter (Kazimierczuk, 2008). The condition given in the Eq. 1 should be ensured for operation in DCM

$$t_{off-max} \leq T_s - t_{on-max} \tag{1}$$

where $t_{off-max}$ is the switch-off time, t_{on-max} is the switch on time, and T_s is the switch cycle time. The primary and secondary current waveforms of DCM flyback converter is shown in Figure 4.2.

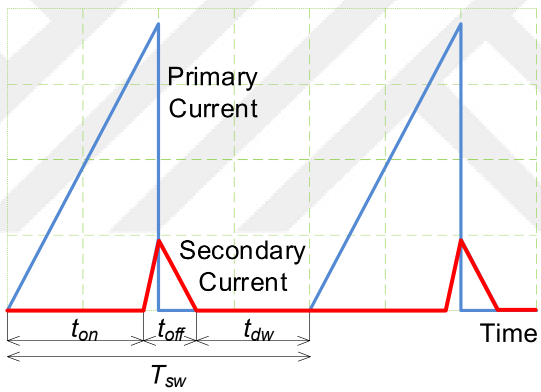

Figure 4.2. The primary and secondary current waveforms of DCM flyback converter

During the on-time, the main switch is closed and the output diode is off. The current pass through the secondary diode is equal to zero. The voltage across the magnetizing inductance is

$$V_{LM} = V_{in} = L_m \frac{dI_{LM}(t)}{dt}, I_{LM}(0) = 0 \tag{2}$$

where V_{in} is the input voltage, I_{LM} magnetizing inductance current, and V_{LM} is the voltage across the magnetizing inductance.

The magnetizing inductance current shows a linear increase as shown below.

$$I_{LM} = \frac{1}{L_m}\int_0^t V_{in}dt = \frac{V_{in}}{L_m}t \tag{3}$$

Thus, the magnetizing current that also equals to the peak value of the current pass through the switch can be stated as

$$I_{LM} = \frac{V_{in}d}{f_s L_m} \tag{4}$$

The on-time of the switch also can be expressed as

$$t_{on} = d_{pk}\frac{1}{fs} \tag{5}$$

where t_{on} is the on-time of the switch, d_{pk} is the peak duty cycle, and fs is the switching frequency. By using the equations given above, magnetizing inductance current can be attained as

$$I_{LM-pk} = I_{LM}(t_{on}) = \frac{V_{in}d_{pk}T}{L_m} = \frac{V_{in}d_{pk}}{L_m fs} \tag{6}$$

The voltage across the diode, V_d is

$$V_d = -\left(\frac{V_{in}}{n} + V_{out}\right) \tag{7}$$

During the off-time, the current passing through the main switch becomes to zero and output diode allows current through it. The voltage across the magnetizing inductance is

$$V_{LM} = -nV_{out} = L_m \frac{dI_{LM}(t)}{dt} \tag{8}$$

where V_{out} is the output voltage and n represents the turn ratio of the transformer.

$$n = \frac{V_{out}(1-d_{pk}-d_{dw})}{V_{in}d_{pk}} \tag{9}$$

where d_{dw} represents the duty ratio of the dwell time. Hence, the equation giving the current passing through the magnetizing inductance can be rearranged as

$$I_{LM} = \frac{1}{L_m}\int_{d_{pk}T}^{t} -nV_{out}dt + I_{LM}(d_{pk}T) = -\frac{nV_{out}}{L_m}(t - d_{pk}T) + \frac{V_{in}d_{pk}T}{L_m} \tag{10}$$

The current passing through the secondary winding of the transformer can be derived as

$$i_2 = -nI_{LM} = -\frac{n^2V_{out}}{L_m}(t - d_{pk}T) + \frac{nV_{in}d_{pk}}{L_m f_s} \tag{11}$$

During the dwell time t_{dw}, the main switch and the output diode are off. Thus the primary winding current, secondary winding current, and output diode current equal to zero.

The magnetizing inductance of the transformer can be derived from the combination of the parameters calculated above. The power capacity can be determined as shown below.

$$P = Exf = \frac{1}{2}L_m(I_{LM})^2 f_s \tag{12}$$

where E indicates the stored energy. The Eq. 12 can be reformed by utilizing the Eq. 6 as shown below.

$$P = \frac{{V_{in}}^2 {d_{pk}}^2}{2L_m fs} \tag{13}$$

Hence, the magnetizing inductance, which is a significant parameter in terms of storing sufficient energy to be fed to the load, can be calculated by utilizing the equation given below.

$$L_m = \frac{{V_{in}}^2 {d_{pk}}^2 \eta}{2P_{out} fs} \tag{14}$$

where η is the expected efficiency and P_{out} is the output power. The magnetizing inductance of the designed quasi-resonant flyback converter is calculated as $16.16\ \mu H$. By taking into account the 10% inductor tolerance and 5% safety margin, the new value of the magnetizing inductance is found as $13.73\ \mu H \cong 14\ \mu H$.

The selection of magnetizing inductance is verified by using the relationship between the peak duty cycle and selected turn ratio as shown in Figure 4.3.

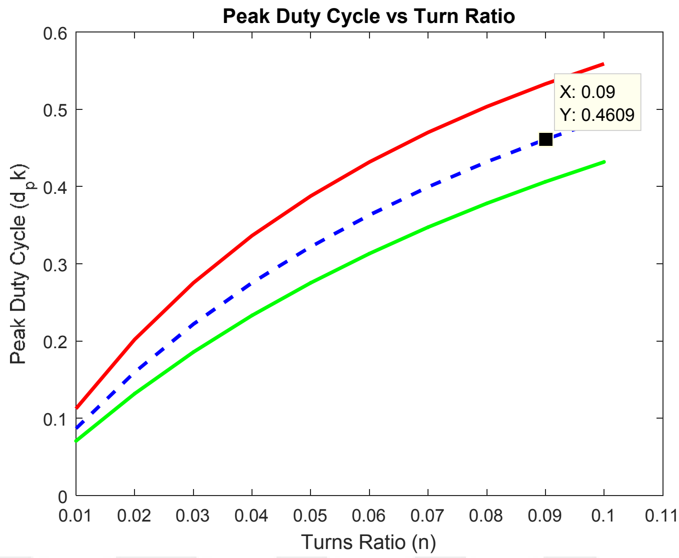

Figure 4.3. The relationship between the peak duty cycle and selected turn ratio

Also, the correlation between the peak duty cycle and total conduction time is analyzed as shown in Figure 4.4.

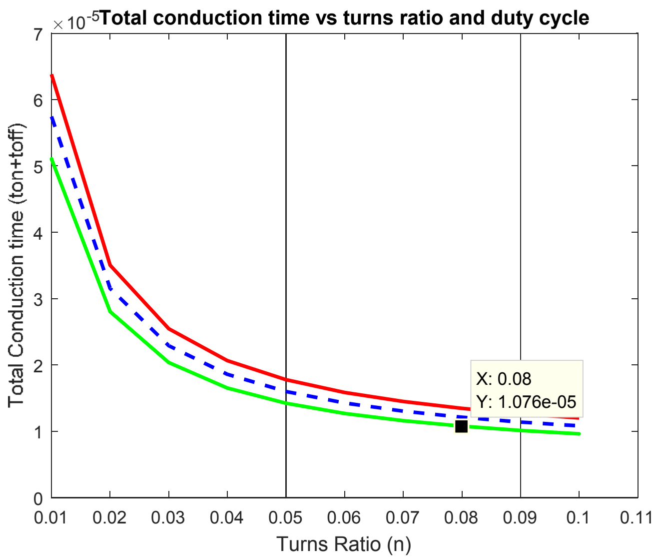

Figure 4.4. The correlation between the peak duty cycle and total conduction time

In Figure 4.5, the correlation of the magnetizing inductance with various values of duty cycle and input PV voltage is investigated.

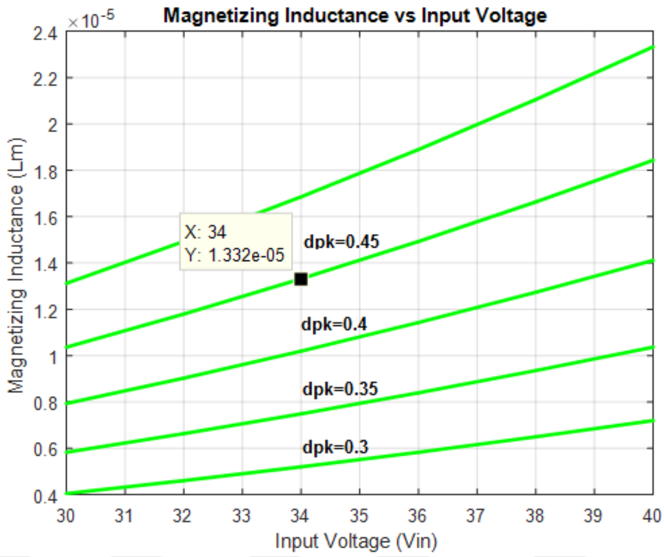

Figure 4.5. The correlation of the magnetizing inductance with different values of duty cycle and input PV voltage

4.2.2. Design of Flyback Transformer

In order to perform an efficient design of the flyback converter, the accurate design of the HF transformer is crucial. The flyback transformer functions as an inductor with two windings. The primary winding is used to store the energy during the switching device conduction interval, and the secondary is used to transfer the stored energy to the load during the diode conduction interval. The transformer design can be considered as an iterative process. Turn ratio of transformer and duty cycle of the converter determine each other. In order to obtain an optimum HF flyback transformer, reduced leakage inductance and length of air gap should be carefully adjusted. The flyback transformer design is conducted by using the parameters given in Table 4.1.

Table 4.1. Design parameters for a DCM flyback converter

Input Voltage Range, V_{in}	30-50 V
Output Voltage, V_o	380 V
Switching Frequency, f_{sw}	50 kHz
Peak Duty Cycle, d_{pk}	0.45
Output Power, P_o	125 W

The transformer magnetic core and turns ratio is determined by using the following equations.

The peak primary current is calculated as $I_{pk,pri} = 19$ A by using the Eq. 15.

$$I_{pk,pri} = \sqrt{\frac{2*P_{out}}{2*f_{sw}*\eta}} \tag{15}$$

It should be noted that the turn ratio and duty cycle effects each other. The peak duty cycle and peak current occur at the minimum input voltage. In this manner turns ratio of the transformer is calculated as 12.75 by using the Eq. 16.

$$n = \frac{(V_o+V_d)(1-d_{pk})}{(V_{in,min}*d_{pk})} \tag{16}$$

In order to determine the proper magnetic core, the energy handling capability of the core in watt-seconds should be specified by using the equation given below.

$$E = \frac{1}{2}A_L(I_{max})^2 \tag{17}$$

I_{max} can be calculated by using the

$$I_{max} = \frac{B_{max}A_e}{A_L} \tag{18}$$

where B_{max} is the peak flux density, A_e is the effective area of the core, and A_L is the inductance factor and depends on the air gap length. These values can be taken from the core datasheets.

By taking the Eq. 17 and 18 into consideration the power rating of the core can be derived as shown below.

$$P = Exf = \frac{1}{2} f_s \frac{{B_{max}}^2 {A_e}^2}{A_L} \tag{19}$$

Hence, E 42/21/15 type ferrite core is utilized to construct the designed transformer. The air gap is adjusted to be in the range of 0.5-0.7 mm.

The minimum number of primary turns is specified as $N_p \cong 8$ by using the Eq. 20.

$$N_p \geq \frac{L_m * I_{pk,pri}}{B_{max} * A_e} \tag{20}$$

The minimum number of secondary turns is specified as $N_s \cong 102$. To calculate the wire diameter on the primary and secondary side, root mean square (RMS) value of current on primary and secondary winding is defined by using the Eq. 21 and Eq. 22, respectively.

$$I_{rms,pri} = I_{pk,pri} \sqrt{\frac{D_{max}}{3}} \tag{21}$$

$$I_{rms,sec} = I_{pk,sec} \sqrt{\frac{1-D_{max}}{3}} \tag{22}$$

By utilizing the equations, RMS values are calculated as $I_{rms,pri} = 7.35$ A and $I_{rms,sec} = 1.48$ A, then Litz wire, which has the average current density of 4 A/mm^2, we need cross-sections of 0.764 mm^2 and 0.34 mm^2 on primary and secondary windings. The wire diameters of primary and secondary windings are 1.528 mm and 0.68 mm, respectively. The designed transformer parameters are given in Table 4.2.

Table 4.2. Transformer parameter

Core and bobbin	E 42/21/15
Primary magnetizing inductance	14 μH
Primary turns	2 * 4
Secondary turns	102
Primary wire cross-sections	1.885 mm^2
Secondary wire cross-sections	0.628 mm^2

4.3. Implementation of DC-AC Converter

A widely known implementation of a single-phase H-Bridge inverter employing two isolated gate drivers achieved as demonstrated in Figure 4.6. The system consists of isolated gate drivers for power MOSFETs (Metal Oxide Semiconductor Field Effect Transistor), and the single-phase inverter consists of a DC bus voltage sensing circuit, grid voltage & current sensing circuit, and MOSFET protection (like overload protection, and so on) circuit.

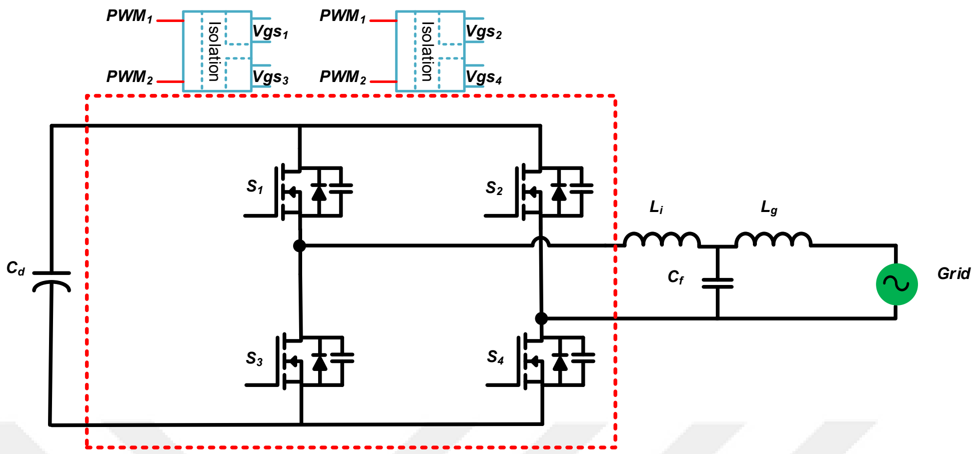

Figure 4.6. Single-Phase H-Bridge inverter with isolated gate drivers

Table 4.3 lists the key specifications for the design of a single-phase full-bridge inverter.

Table 4.3. The key specifications for this design

Input voltage	Typical 380 V DC, max 400 V DC
Output voltage	220 V_{rms}
Output Current	Max I_{rms} , 3.5 A
Appeared Power, VA	350 VA
Output Current THD	<3% for greater than 40% rated load
Switching Frequency	20 kHz

4.3.1. Sizing of DC-Link Capacitor

The required capacity of the DC-link capacitor is calculated by considering the percentage of dc bus ripple tolerable, minimum bus voltage value, and apparent power of the system. The DC-link capacitor is chosen as 470 µF for voltage ripple rate ΔV that not exceed 2%, with the minimum equivalent series resistor (ESR) and equivalent series inductance (ESL) values. The selection of low ESR and ESL is crucial in terms of attaining high efficiency and suppressing noise and stabilize operations in a circuit that operates at a high frequency.

4.3.2. Design of Output Filter

A high order LCL filter has been utilized to smooth the output current of voltage source inverter. A higher harmonic attenuation can be achieved by using small inductances, which improves the transient behavior and enhances the operation range of the inverter. The model of the plant can be represented as shown in Figure 4.7.

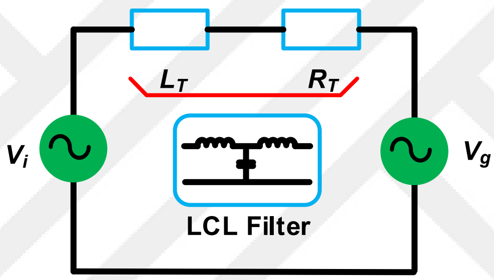

Figure 4.7. The model of the plant

To obtain the transfer function of the plant, the current flowing through the filter is derived as given in Eq. 23.

$$i_{Li} - i_C - i_{Lg} = 0 \tag{23}$$

The voltages can be given as (in “s” domain)

$$V_i = i_{Li} L_i s + V_c$$

$$V_g = -i_{Lg} L_g s + V_c$$

$$V_c = i_c(\frac{1}{C_f s} + R_d) \tag{24}$$

The equations are given in Eq. 24 can be rearranged as shown below.

$$i_{Li} = \frac{1}{L_i s}(V_i - V_c), i_{Lg} = \frac{1}{L_g s}(V_c - V_g) \tag{25}$$

The voltages can be rearranged as

$$V_i = \left(L_i s + \frac{1}{C_f s} + R_d\right) i_{Li} - \left(\frac{1}{C_f s} + R_d\right) i_{Lg}$$

$$V_g = \left(\frac{1}{C_f s} + R_d\right) i_{Li} - \left(L_g s + \frac{1}{C_f s} + R_d\right) i_{Lg} \tag{26}$$

The transfer function of the plant is $H(s)$ obtained as by assuming that $V_g = 0$

$$H(s) = \frac{i_{Lg}}{V_i} = \frac{R_d C_f s + 1}{(L_i L_g C_f)s^3 + \left(L_g R_d C_f + L_i R_d C_f\right)s^2 + (L_i + L_g)s} \tag{27}$$

The resonant frequency of the filter is determined to be around 5 kHz. Ripple tolerance of the filter is also taken as 10%. Thus, the filter parameters are selected as demonstrated in Table 4.4.

Table 4.4. Filter Parameters

L_i	L_g	C_f	R_d
$4\ mH$	$1\ mH$	$1\ \mu H$	$8\ \Omega$

The (a) bode plot and (b) pole-zero map of the designed filter with the determined parameters are given in Figure 4.8.

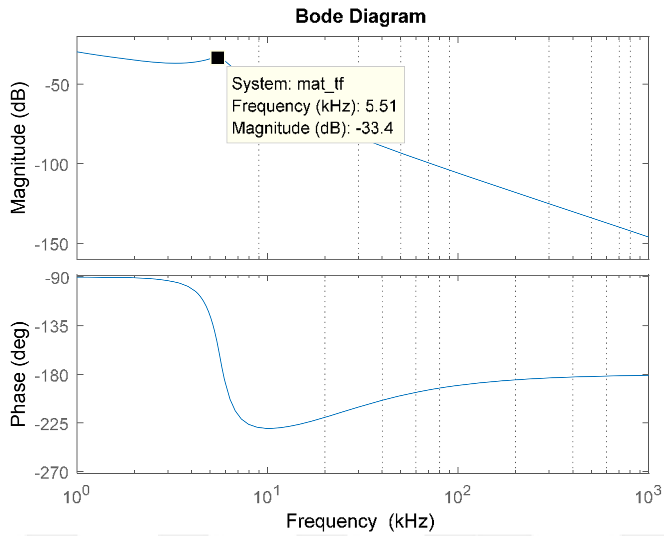

(a)

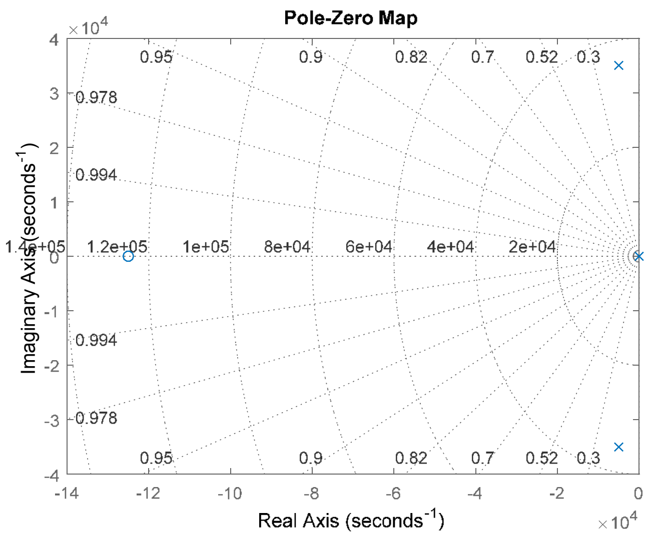

(b)

Figure 4.8. The (a) bode plot and (b) pole-zero map of the designed filter

4.4. Control Strategy of Developed PV MI

Control strategy of developed PV MI mainly covers the solutions of problems related to technical challenges in connecting PV sources to the utility grid and satisfies the MPPT performance criteria such as accuracy, precision, speed, robustness and handling the rapidly changing atmospheric conditions. The increasing integration of PV systems into the utility grid, create challenges in various technical aspects such as power quality, reliability, and protection. Hence, the grid connection requirements are the key specifications that can be used as a guide for the design and performances of the PV inverter.

It is possible to foresee expanded integration of grid-connected PV systems in low voltage grids, so dynamic grid support features might be required also for PV-MIs in the future. Moreover, the rate of the injected current harmonics arouses potential problems for the low voltage utility grid. In addition, the controller of the MI should cope with the frequency fluctuations, and voltage flickers due to power fluctuations from PV for the sake of achieving the grid's stability.

In this manner, the designed PV MI provides the features of smart PV systems and becomes more competitive in various aspects.

4.4.1. Proposed Maximum Power Point Technique

A mathematical model, which provides a maximum operating point of the PV module, is derived by using GEP. GEP is an improved methodology, which belongs to the class of the Genetic Algorithm (Ferreira, 2011). GEP utilizes populations of individuals, select the individuals according to fitness value and introduce genetic variation utilizing one or more genetic operators. Gene expression programming algorithm is provided in Figure 4. 9. Due to eliminating the shortcomings of GA, being universal, and presenting a favorable correlation between predictor variables and the target value, GEP is chosen to extract a mathematical model that ensures the maximum operating point of the PV module.

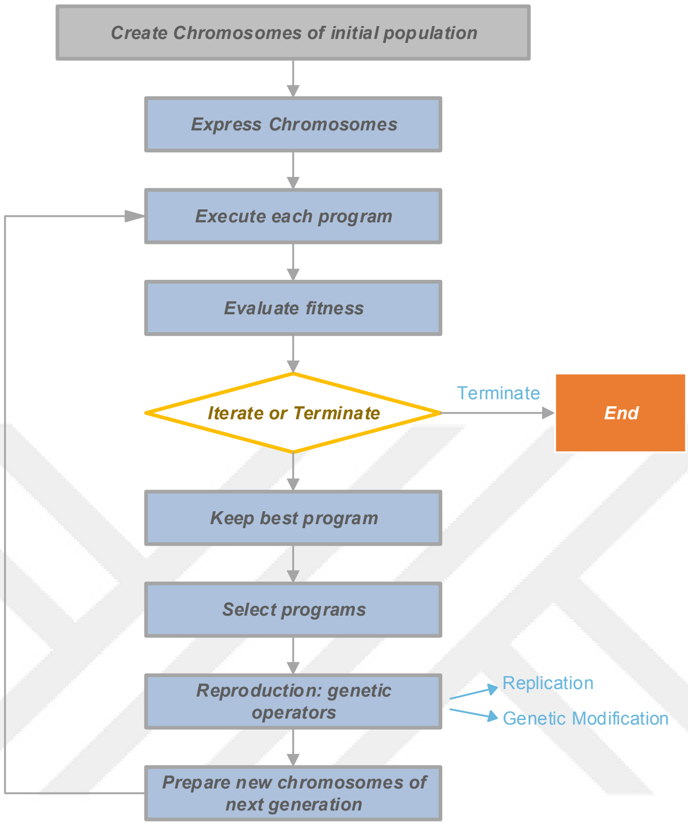

Figure 4.9. Gene expression programming algorithm (Ferreira, 2011)

GEP includes function set, terminal set, fitness function, control parameters, and termination. Symbolic regression is a commonly utilized method to attain a mathematical equation for a target output related to the input variable for a data set. Each sample of data contains input variables and target variable that can be represented as

$$\{x_{i,1}, x_{i,2}, \dots, x_{i,n}, y_{i,1}, y_{i,2}, \dots, y_{i,m}\} \quad (28)$$

where n indicates the number of input variables and m indicates the number of target variables. The symbolic regression aims to obtain optimal τ^* which minimizes the error for the data set.

$$\tau^* = arg_\tau min f(\tau) \tag{29}$$

where τ is the quality parameter of the derived equation, $f(\tau)$ is the fitting error of τ (Zhong et al., 2017). To perform the error analysis of the model, statistical error estimation methods, namely root mean square error (RMSE), mean squared error (MSE), mean absolute error (MAE), and mean absolute percentage error (MAPE) are widely used.

The symbolic regression analysis is employed to find the best suitable mathematical function. The combined expression of the equation is given in Figure 4.10.

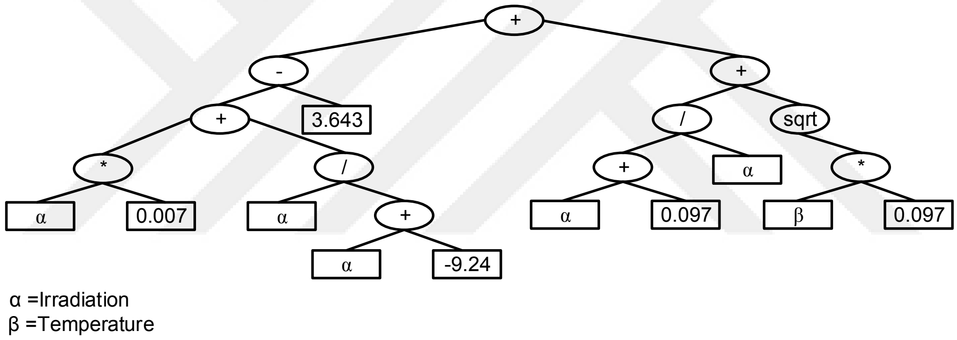

Figure 4.10. The combined expression of the obtained equation.

The extracted mathematical equation is

$$y = \left(\left((0.00766 * I) + \left(\frac{I}{I + (-9.2429929)} \right) \right) - 3.6435974 \right) + (0.0970357 * T)^2 + \left(\frac{I}{I + (-9.2430242)} \right) \tag{30}$$

where I represents the irradiation level, T corresponds to the temperature and y is the voltage reference value.

A number of the model parameters employed during the process stage are adjusted as population size is 50, number of maximum tries for initial population is 10000, genes per chromosome is 4, number of maximum generations is 2,000, number of generations without improvement is 1,000, stop for the best chromosome's fitness score is 1. MSE is used as a fitness function and hit tolerance is determined as 1%. It is allowed to perform algebraic simplification. Allowed processes are addition, subtraction, multiplication, division, and square root. The generation required to train the model is 1,918. The number of evaluations of the fitness function is 110,250. The complexity of the model is reduced from 58 to 22 after the simplification process. Generations required for simplification is 3. Nonlinear regression improved the accuracy of the model.

The coefficient of determination between the actual and predicted value is 0.9993 and the obtained MAPE value is 0.8123 for the training data. Hence, the statistical analysis methods approved the prediction accuracy of the model. Results of the GEP model given in Table 4.5.

Table 4.5. Results of the GEP model

	R^2 (%)	CV (%)	MAE	RMSE	MAPE (%)
GEP	99.937	1.165	0.033	0.055	0.812

The performance of modeled PV MI is evaluated with a conventional and proposed MPPT method under different atmospheric conditions. In order to indicate the robustness of the proposed MPPT method a number of tests are applied to the overall system. The system is tested in terms of overshoot, convergence speed, tracking accuracy, and the number of oscillations. The performed case studies have demonstrated that convergence speed, dynamic response of the system, and tracking accuracy are substantially improved especially for the rapidly changing atmospheric conditions. The complexity level of the control algorithm is also significantly reduced.

The MPPT control is achieved utilizing an outer voltage loop and inner current loop. I_{pvref} is sensed before the input capacitance that is connected to the PV in parallel. Owing to the uncontrolled output voltage of the converter, the voltage feedback is mapped to the internal comparator to prevent the excessive voltage rising. The control diagram of the MPPT operation is demonstrated in Figure 4.11.

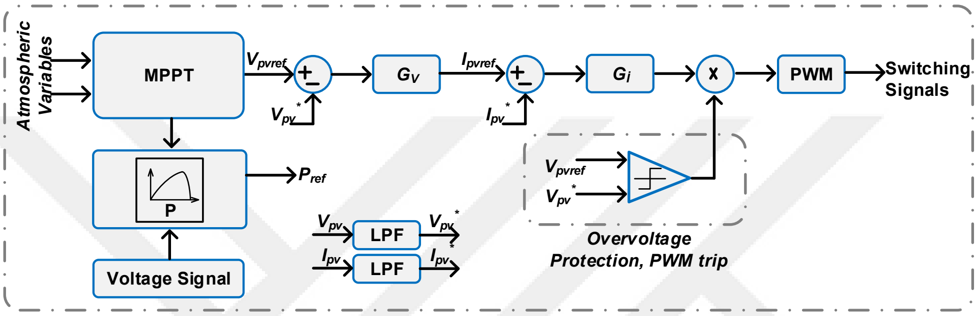

Figure 4.11. The control diagram of the MPPT operation

The main function of the MPPT block can be indicated as the determination of the accurate reference signal corresponding to operation at the maximum point. The generated reference signal is compared with the actual measured signal and the resulting error signal is passed through the PI controller in order to adjust the operating point of the PV module. The adjustment of the operating point is realized by sending the switching signals to the DC-DC converter. In this way, the control diagram given in Fig. 4.11 realizes the control of the DC-DC converter.

4.4.2. Improved Closed Loop Voltage Oriented Control

The growing installation of single-phase grid-connected PV systems, raising new issues in various technical aspects such as power quality, reliability, and protection. In view of the fact that some smart functionalities are expected for all of the inverters in the near future (Yang et al., 2013). It is possible to foresee expanded penetration of PV MI systems in low voltage grids, so ancillary services such as dynamic grid support and low-voltage ride-through features might be required also for PV MIs in the future. The grid connection requirements are the key specifications that can be used as a guide for the design and performances of the PV inverter.

Moreover, the rate of the injected current harmonics arouses potential problems for the low voltage utility grid. Therefore, the controller of the PV MI should compensate the injected current harmonics to the grid. In addition, the controller of the MI should cope with the frequency fluctuations, and voltage flickers due to power fluctuations from PV in order to maintain the grid’s stability. On the other hand, to achieve the islanding detection voltage and frequency of the grid should be monitored. In the case of over/under voltage or over/under frequency, the inverter must cease supplying power to the utility grid. Thus islanding detection methods can be utilized to detect islanding owing to voltage and frequency variations (Teodorescu et al., 2011). In passive islanding detection methods, the harmonics level in the voltage also can be used due to demonstrating the abnormal increasing.

In light of the aforementioned objective, to control the inverter PQ closed-loop voltage oriented control configuration based on the stationary αβ frame is utilized (Yang et al., 2014). This control system can contribute to improving system reliability with mitigating challenges related to complexity. In addition, the control structure is improved by integrating hybrid passive islanding detection property and selective harmonic compensator as shown in Figure 4.12. Detection of over/under frequency and over/under voltage protection fails to detect islanding due to the decreased amount of power mismatch at the PCC. Therefore the harmonics level in the voltage is also determined to detect the islanding.

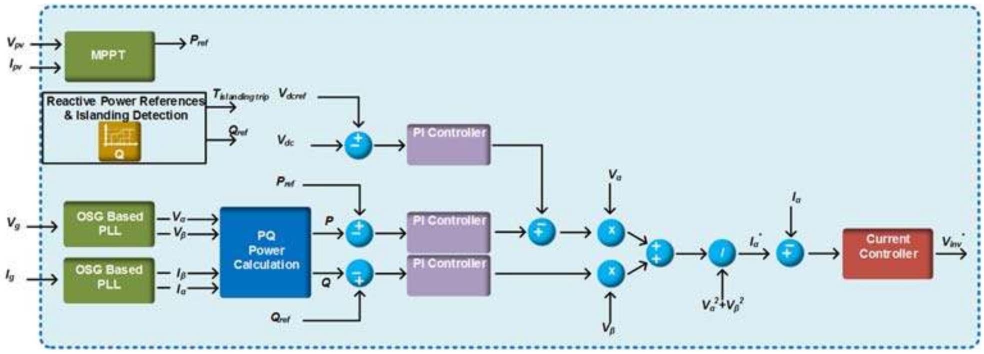

Figure 4.12. The control diagram of the inverter

The realization of this control is based on the instantaneous power theory (Akagi et al., 2007). According to the instantaneous power theory, the single-phase instantaneous active and reactive powers resulting from

$$\left.\begin{aligned} P &= \frac{1}{2}\left(v_\alpha i_\alpha + v_\beta i_\beta\right) \\ Q &= \frac{1}{2}\left(v_\beta i_\alpha - v_\alpha i_\beta\right) \end{aligned}\right\rangle \tag{31}$$

where α and β components of grid current and voltage are generated by the orthogonal signal generator (OSG) part of SOGI as shown in Figure 4.13 (Ciobotaru et al., 2006).

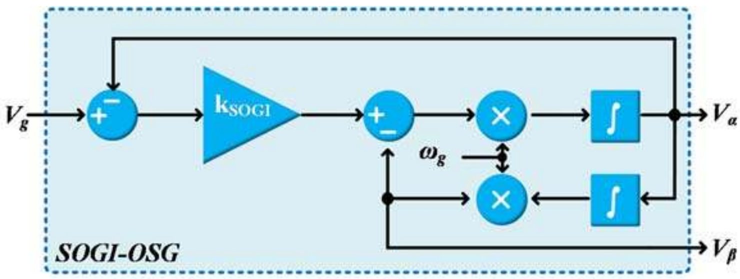

Figure 4.13. OSG generation part of SOGI (Ciobotaru et al., 2006).

The error signals, which attained from the difference between the actual and reference power values, are fed to the PI controller. After that, the current reference can be realized as

$$\begin{bmatrix} i_\alpha{}^* \\ i_\beta{}^* \end{bmatrix} = \frac{2}{v_\alpha{}^2+v_\beta{}^2}\begin{bmatrix} v_\alpha & v_\beta \\ v_\beta & -v_\alpha \end{bmatrix}\begin{bmatrix} P^* \\ Q^* \end{bmatrix} \quad (32)$$

The outer and inner control loop of the power converter with the control block diagram of the inner control loop is provided in Figure 4.14.

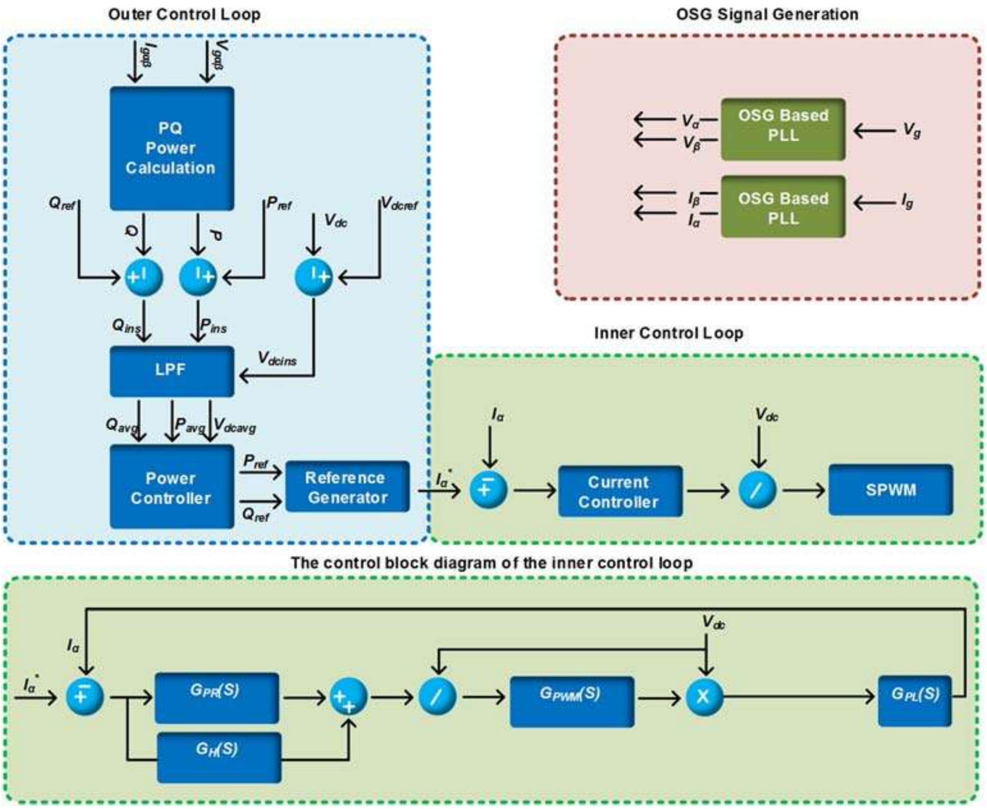

Figure 4.14. The outer and inner control loop of the power converter with the control block diagram of the inner control loop

$G_{PWM}(s)$ represent the processing and PWM delay of the microcontroller that is equal to 1.5 times of one sample T_s and represented as

$$G_{PWM}(s) = \frac{1}{1+1.5T_s s} \tag{33}$$

$G_{PL}(s)$ represent the transfer function of the plant as given below.

$$G_{PL}(s) = \frac{R_d C_f s+1}{(L_i L_g C_f)s^3+(L_g R_d C_f+L_i R_d C_f)s^2+(L_i+L_g)s} \tag{34}$$

The current controller is designed on the stationary reference frame using the proportional resonant (PR) controllers to achieve zero steady-state error. The resonant controller is tuned to the fundamental frequency and 3th and 5th harmonic frequencies in order to attain high power quality at the output. In the controllers, the non-ideal type resonant controllers are chosen to limit the high controller gain in the tuned resonance frequencies. The PR current controller is represented as (Teodorescu et al., 2006).

$$G_{PR}(s) = K_P + K_I \frac{2K_c(hw_1)s}{s^2+2K_c(hw_1)s+(hw_1)^2} \tag{35}$$

From Figure 4.14 the open-loop transfer function of the system is attained as

$$G_o(s) = G_{PR}(s)G_{PWM}(s)G_{PL}(s) \tag{36}$$

The closed-loop transfer function of the system is obtained as

$$G(s) = \frac{G_{PR}(s)G_{PWM}(s)G_{PL}(s)}{1+G_{PR}(s)G_{PWM}(s)G_{PL}(s)} \tag{37}$$

The corresponding frequency response of the overall system for open-loop and the closed-loop system is shown in Figure 4.15. K_P, K_I, and K_c values are determined according to the system performance. It can be seen that the system control is stable.

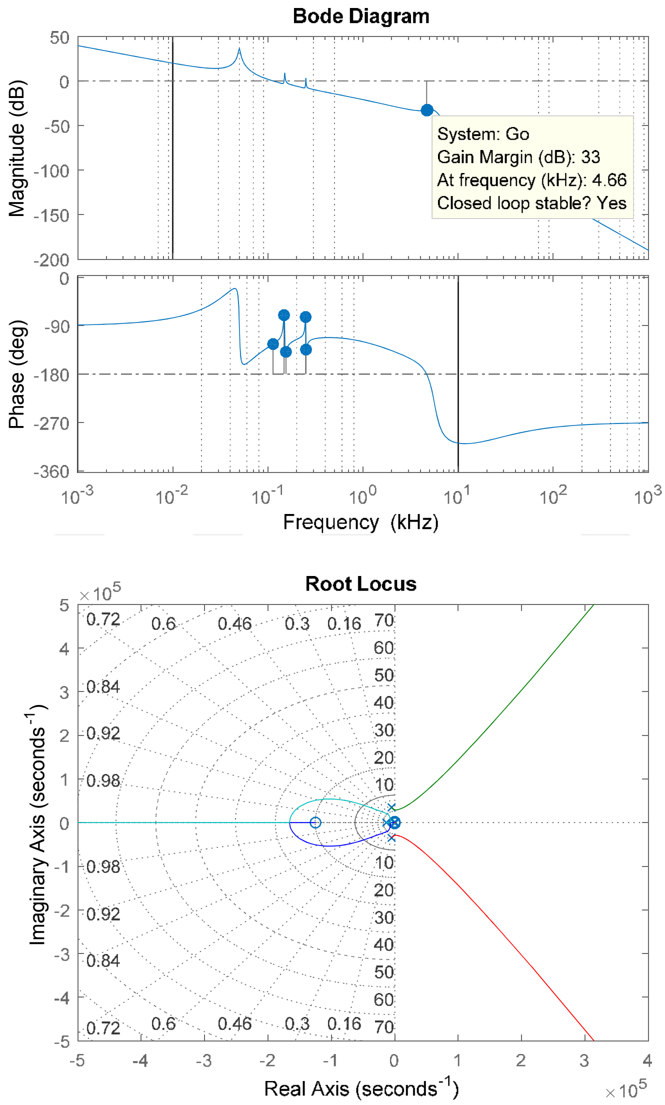

Figure 4.15. The frequency response of the overall system for the obtained open-loop transfer function

The open-loop transfer function for obtaining the root locus diagram is considered. To do this, the poles and zeros are located on the complex plane. The main goal is to sketch the root locus diagram for the gain variation from zero to infinity. It is known that for the zero gain the root locus starts from the poles of the system then moves towards zeros of the system at infinity gain. In our system, there are ten poles and seven zeros. Actually, we will take the three zeros at infinity into consideration to sketch the root locus. Then we determined the real part of the root locus. According to the system, the pole at origin and the pole at $-1.33e^4$ point moves towards each other. At the 6.2 gain value, the system has a break out point at $-6.67e^3$. It can be seen from the root locus diagram. The other real part of the root locus is between the zero at $-1.25e^5$ and zero at infinity. So we have a break in point in this region. The break-in point is found at $-1.66e^5$. The complex conjugate poles at ($-5e^3 + 3.5e^4i$) and ($-5e^3 - 3.5e^4i$) move towards the zeros at infinity through the asymptotes. So the critical point is the determination of the gain for stability. The critical gain value is obtained as 43.9 for providing stability.

The controller structure of the inverter is formed with functionalities such as harmonic compensation, low-voltage ride through, and dynamic grid support capability. Constant average active power control is performed as a reactive power injection strategy in order to extract maximum power from PV modules even in a fault condition. The voltage sag/swell rate is determined by using a block that determines the rate as per unit. The normal operation within the dead band is maintained until the voltage variation exceeds the determined values. The rate of droop sets the amount of the required reactive power. It is worth to point out that the allowable maximum output current value should be adjusted carefully according to the defined reactive power limit. The determined output current limit will directly affect the design process of the inverter. Moreover, the analog protection circuit is adjusted to prevent the inverter from the overcurrent shutdown due to the reactive power injection (Yang et al., 2014). The apparent power rating, S_n should be taken into consideration in order to limit the amount of reactive power as shown below.

$$|Q| \leq \sqrt{{S_n}^2 - P^2} \tag{38}$$

It should be noted that sufficient reactive power can be injected into the utility-grid during low voltage ride through (LVRT) without the need to reduce the active power. When wide-scale integration of PV systems to the distribution grid is considered, dynamic grid support is a significant feature especially for the high-power string and central inverters. However, with increased penetration of DGs in low voltage grids, dynamic grid support features might be required also for PV MIs in the future. The first requirement is to stay connected to the grid in case of under-voltage and the further requirement is supporting the grid by injecting reactive power. In light of this, the dynamic grid support capability is ensured to fulfill the grid-connection demands of the PV systems.

4.5. Design of Control System and Power Circuit

In the scope of this thesis work, an experimental prototype of grid-connected single-phase PV MI is designed and implemented. The implementation studies of the PV MI prototype are achieved in the Research Laboratory of Çukurova University Electrical and Electronics Engineering Department.

The simulation model constructed in an electromagnetic transient software environment, PSCAD/EMTDC, supports the theoretical design studies of PV MI. Moreover, the MATLAB is utilized to determine the controller parameters and test their stabilities. The design specifications of the grid-connected single-phase PV MI prototype are specified and validated by utilizing the results of the simulation study.

PV MI system is principally considered as two parts namely power circuit and control system. In the subsequent sections, the design procedures of the power circuit, the selection of power components, the design of the control system, and the selection of appropriate integrated circuits (ICs) are introduced.

4.5.1. General Design Considerations of PV MI

The main objective of this PV MI prototype can be indicated as a functional micro inverter with a reduced system cost and compact design. Moreover, the major considerations are focused on enabling high performance with safe operation. Hence, the essential voltage and current signals to control the PV MI must be measured in high accuracy. In addition, the gate signals must be produced in high resolution to achieve effective control and efficiency performance. Isolated amplifiers are used to realize high bandwidth and sensing accuracy. The input of the isolated amplifiers is directly connected to the resistors (voltage divider resistor, shunt resistor) for use in high-resolution measurement applications. The output of the isolated amplifiers is combined with the operational amplifier in order to carry out differential to single-ended output. The utilized isolated amplifiers use the 8-pin package, which reduces board size (Texas Instrument, 2018). Furthermore, isolated dual-channel gate drivers are utilized to drive power MOSFETs. The utilized isolated dual-channel gate drivers use the 16-pin package. The block diagram of the PV MI prototype's including the control system and power circuit is shown in Figure 4.16.

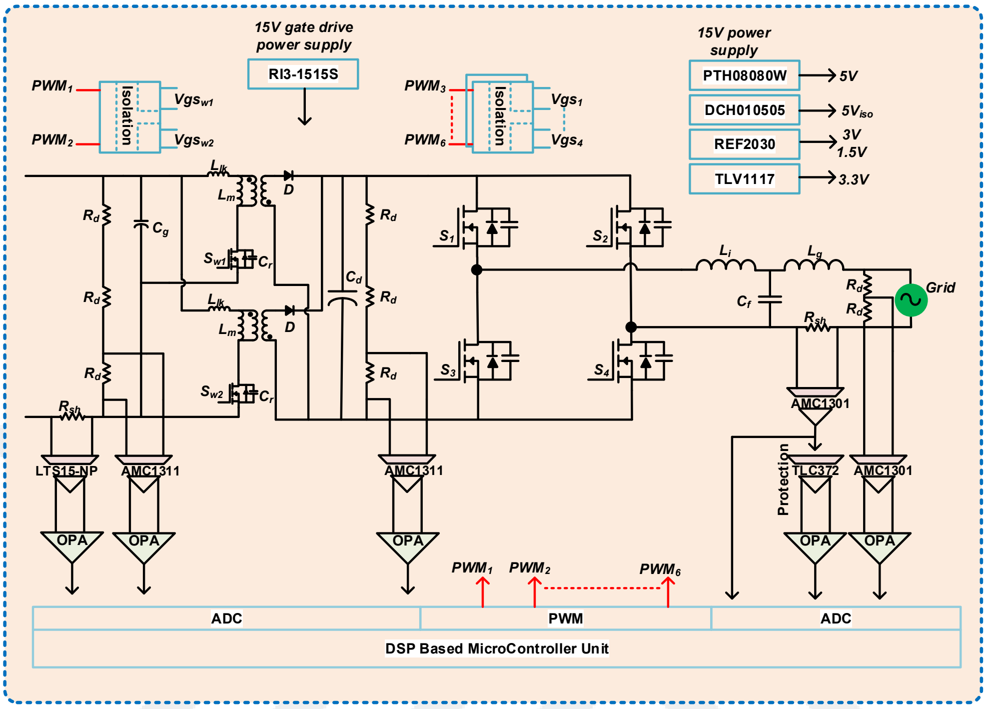

Figure 4.16. The block diagram of the PV MI prototype

The system generally composed of two fundamental parts namely the power circuit and the control system. The power circuit consists of a quasi-resonant interleaved flyback converter and a full-bridge inverter. The major parts of the control system are digital signal processor (DSP) based microcontroller unit (MCU), measurement circuits, analog protection, fault detection circuit, and gate driver circuits.

The DSP based MCU can be accepted as the brain of the control system. In spite of the fact that single DSPs show higher performance than DSP based MCUs, DSP based MCUs propose superiority in the facilitation of control system design with their peripherals named as an analog to digital converter (ADC) and pulse with modulation (PWM) units.

There are five signals measured by the control system of the PV MI prototype. The measured signals are including a DC-link voltage, a grid voltage, a grid current, a PV input voltage, and a PV input current. The measurement circuits carry out signal conditioning of the measured signals for ADC of MCU. The measurement circuits should be performed with high accuracy for increasing the performance of the PV MI prototype.

An analog protection circuit is implemented for additional protection of the PV MI prototype besides the software protection. A trip signal is generated and sent to the disable pin of gate drivers to stop the operation of the system.

The switching signals and fault signals are directly transferred to power MOSFET drivers. The chosen power MOSFET drivers have -0.3 V to input bias pin supply voltage +0.3 V logic voltage level range so voltage level transition circuits are not required.

The details of the power circuit and control system are introduced in the following sections.

4.5.2. Design of Power Circuit

The design of the power circuit is considered as two parts. The first part is the design of a quasi-resonant interleaved flyback converter and the other part is the design of full-bridge inverter. The implementation of the DC-DC converter is mentioned in section 4.2. The selection of power MOSFETs is realized by using simulation results and the equation given below.

$$V_{DS} = V_{in} + nV_{out} + V_{lk} \tag{39}$$

where V_{DS} is the drain-source voltage of MOSFET and V_{lk} is the leakage voltage resulting from the leakage inductance. V_{lk} is practically taken as 30% of the input voltage. With this background power, MOSFET STF100N10F7 from STMicroelectronics has been selected due to having the lower cost and lower $R_{DS,on}$

resistance than the other switching components. The technical specifications of STF100N10F7 are provided in Table 4.6.

Table 4.6. Technical specifications of STF100N10F7

V_{DS}	I_D	$R_{DS,on}$	V_{GS}	Q_g
$100\ V$	$45\ A$	$8\ m\Omega$	$\pm\ 20\ V$	$61\ nC$

The power diodes of the DC-DC converters MUR1560 from ON Semiconductor has been selected because of the lower cost and proper electrical specifications. Technical specifications of the MUR1560 power diode are provided in Table 4.7.

Table 4.7. Technical specifications of MUR1560

DC Blocking Voltage	Rectified Forward Current	Reverse Recovery Time	Voltage - Forward	Current - Reverse Leakage
$600\ V$	$15\ A$	$60\ ns$	$1.5\ V$	$10\ \mu A$

Selecting of the input capacitor is performed by using the basic capacitor current equation as shown follow

$$\left.\begin{aligned} i_c &= \frac{dV}{dt} \\ C\frac{\Delta V}{t_{on}} &= i_{pv}d_{pk} \\ C\frac{\Delta V}{t_{off}} &= i_{pv}(1-d_{pk}) \\ t_{on} &= d_{pk}T_s \end{aligned}\right\rangle \tag{40}$$

When the peak duty cycle d_{pk} is taken as 0.4 the capacity of the input PV capacitor can be calculated as

$$C = \frac{1.2 i_{pv}}{5 f_s \Delta V} \quad (41)$$

where f_s is the switching frequency. In light of this, the input capacitor R60EW61005000K from KEMET has been selected. It is a film capacitor with a $100\ V$ DC voltage rating and a 100 µF capacity rating.

The implementation of the full-bridge converter is mentioned in part 4.3. The selection of the DC-link capacitor is also mentioned. The minimum DC-link voltage value is also determined as 380 V. In light of this, the input capacitor ESMQ451VSN471MA40S from United Chemi-Con has been selected because of the lower cost and proper electrical specifications. The detailed specifications of the DC link capacitor can be found in the datasheet provided by the manufacturer.

The minimum drain-source voltage and drain current of H Bridge inverter's power MOSFETs should be 400 V and 5 A with respect to theoretical calculations and simulation results. In view of this, power MOSFET IPA65R190CFDXKSA1 from Infineon Technologies determined to utilize for the lower cost and lower $R_{DS,on}$ resistance when compared to other proper switching components. The technical specifications of IPA65R190CFDXKSA1 are provided in Table 4.8.

Table 4.8. Technical specifications of IPA65R190CFDXKSA1

V_{DS}	I_D	$R_{DS,on}$	V_{GS}	Q_g
$650\ V$	$17.5\ A$	$190\ m\Omega$	$\pm 20\ V$	$68\ nC$

4.5.3. Selection of Digital Signal Processor Based Microcontroller Unit

TMS320F28335 DSP card that employe the DIMM 100 connection interface is selected to use in the control system of the PV MI prototype. The TMS320F38335 includes auxiliary circuitries for peripheral modules, boot options, and emulator connections. The design and operation stages of the control system are facilitated by using the control card TMS320F38335.

The selection process of DSP based MCU that employed in the control system of the PV MI prototype includes some criteria as introduced following

- The operating cycle rate of MCU should be lower than $100\ \mu s$ for achieving the operation of the ADC conversion process, control algorithm, protection software, and PWM signal generation,
- The technical specifications of ADC and PWM modules should provide the real-time operation of MCU,
- The hardware mathematical calculation units should be ensured by the MCU to limit the time spend for the operating cycle of calculations,
- The real-time debugging specifications with emulators should be provided in order to monitor the control process,
- Enough memory for the control software and data should be supplied.

The selection of the control card TMS320F28335 is performed by taking the criteria given above into account. The technical specifications of the TMS320F28335 are given in Table 4.9 (Texas Instrument, 2015).

Table 4.9. The technical specifications of TMS320F28335

CPU Specifications	
Clock Frequency	≥ 100 MHz
Cycle Time	≤ 10 ns
Floating Point Unit	Yes
Memory Specifications	
RAM	≥ 32 KB
Flash Memory	≥ 128 KB
ADC Specifications	
Channel Number	≥ 10
Resolution	≥ 10 bit
Sample Rate	≥ 10 MSPS
Conversion Time	≤ 100 ns
PWM Specifications	
Channel Number	≥ 6
Resolution	≥ 12 bit
Number Of Pins	
GPIO Pins	Up to 88
PWM Outputs	Up to 18
ADC Channels/Resolution	16 Channel / 12 Bits

4.5.4. Design of Measurement Circuits

The control system of the PV MI prototype measures five signals, which are DC-link voltage, a grid voltage, a grid current, a PV input voltage, and a PV input current.

The PV input voltage and DC-link voltages are measured by the AMC1311 isolated amplifier from Texas Instrument. The AMC1311 is a high-impedance input isolated amplifier with an output isolated from the input circuitry by an isolation barrier that is highly resistant to magnetic interference. The DC voltage sensing circuit utilizes a high impedance voltage divider circuit. Thanks to the voltage divider circuit, the voltage level is scaled down. This high impedance source signal is measured by using AMC1311 with high accuracy. Due to having a very high input impedance that causes gain error and offset error, makes the effect of source impedance negligible (Texas Instrument, 2018). The technical specifications of the AMC1311 are summarized in Table 4.10.

Table 4.10. Technical specifications of the AMC1311

AMC1311	
Input Voltage Range	0-2 V
Offset Error and Drift	$\pm 1.6\ mV\ at\ 25\ C^{\circ}, 21\ \mu V/C^{\circ}$
Fixed Gain	1
Gain Error and Drift	$\pm 0.3\%\ at\ 25\ C^{\circ}, \pm\ 60\ ppm/C^{\circ}$
Nonlinearity and Drift	$\pm 0.05\%, 1\ ppm/C^{\circ}$

Differential amplifier gain of OPA320 is adjusted to 1.5 V/V. The voltage drop across the sensing resistor must not exceed 2 V and the AMC1311 provides 0-2 V output with the fixed gain ratio as 1. The measured voltage signal is adjusted with an operational amplifier to 0-3 V ADC input range of the selected MCU. The power supplies of the AMC1311 are decoupled by using the capacitors. These decoupling capacitors should be positioned close to the supply pin of the AMC1311. The output of the AMC 1311 is filtered by using a differential filter. The filtered output of AMC1311 is connected to the OPA320AIDBVR in order to convert differential-end to single-end. In addition, the signal is buffered via OPA4376 before interfacing with the MCU. The combination of the filter can be configured according to the cutoff frequency and time delay. The constructed circuit schematic of AMC1311 to measure the DC link voltage is illustrated in Figure 4.17.

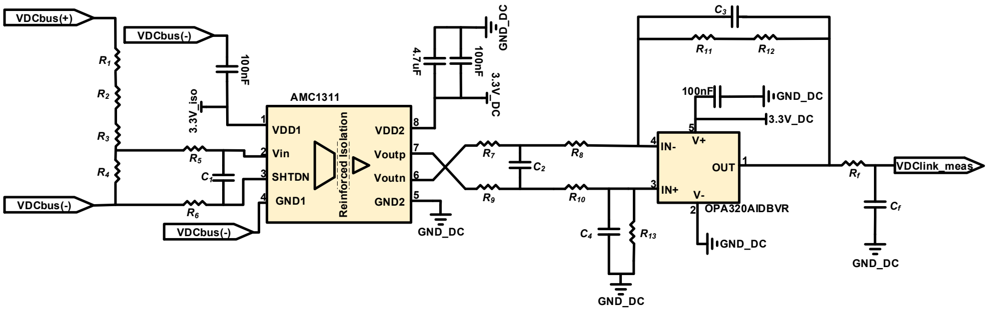

Figure 4.17. The constructed circuit schematic of AMC1311 to measure the DC voltage

In addition, the constructed circuit schematic is simulated by using the TINA-TI-V9 software and different DC link voltage levels are measured to verify the measurement circuit as depicted in Figure 4.18. Figure 4.18 VF1 indicates DC link voltage and VM1 shows the measurement output.

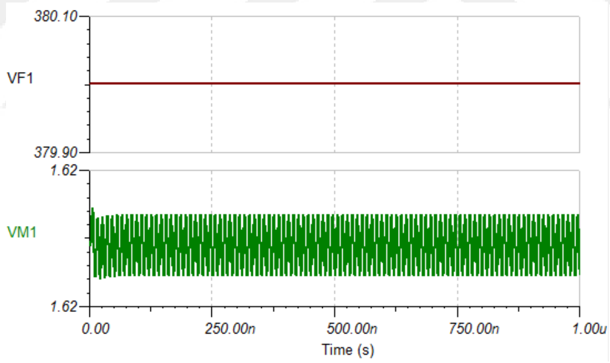

Figure 4.18. AMC1311 DC link voltage measurement circuit simulation result

AMC1301 isolated amplifier from Texas Instrument utilized to measure the grid current and grid voltages. The AMC1301 is also a precision input isolated amplifier with an output isolated from the input circuitry by an isolation barrier that is highly resistant to magnetic interference. AMC1301 isolated amplifiers, which optimized for isolated current sensing are used to measure the grid current & voltage.

It has a ±250 mV input voltage range with an 8.2 fixed gain. The technical specifications of the AMC1311 are given in Table 4.11 (Texas Instrument, 2018).

Table 4.11. Technical specifications of the AMC1301

AMC1301	
Input Voltage Range	$\pm 250\ mV$
Offset Error and Drift	$\pm 200\ \mu V\ at\ 25\ C^{\circ}, \pm 3\ \mu V/C^{\circ}$
Fixed Gain	8.2
Gain Error and Drift	$\pm 0.3\%\ at\ 25\ C^{\circ}, \pm\ 50\ ppm/C^{\circ}$
Nonlinearity and Drift	$\pm 0.03\%, 1\ ppm/C^{\circ}$

The input of the AMC1301 is specialized for direct connection to shunt resistors or other low voltage level signal sources. In addition, it provides an isolated voltage sensing property. The output of the AMC 1301 is filtered by using a differential filter. The filtered output of AMC1301 is connected to the OPA320AIDBVR in order to convert differential-end to single-end. In addition, the signal is buffered via OPA4376 before interfacing with the MCU. The combination of the filter can be configured according to the cut off frequency and time delay. The differential amplifier gain of OPA320 is adjusted to 0.79 V/V. The measurement range of the isolation amplifier is adjusted to ± 5 A by using a 50 mΩ shunt resistor. The power supplies of the AMC1301 are decoupled by employing the capacitors. These decoupling capacitors should be mounted close to the supply pin of the AMC1301. The output of the AMC 1301 is filtered by using a differential filter. The combination of the filter can be configured according to the cut off frequency and time delay. The constructed circuit schematic of AMC1301 to measure the grid current & voltage is illustrated in Figure 4.19.

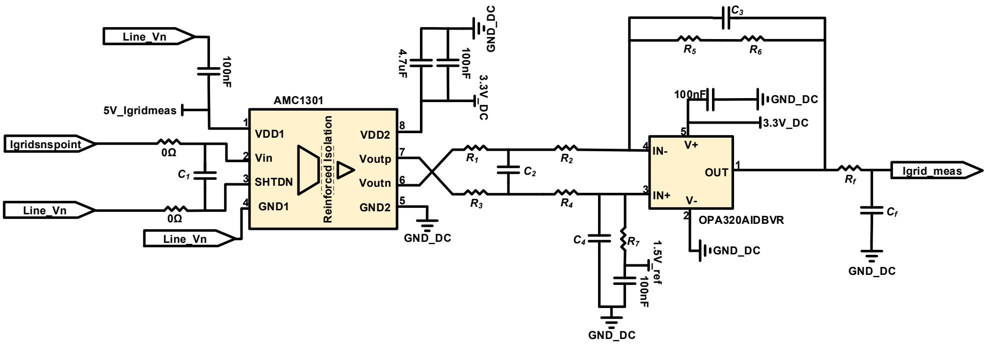

Figure 4.19. The constructed circuit schematic of AMC1301 to measure the grid current & voltage

The grid voltage & current measurement signal is formed in the range of ±1.5 V peak with an operational amplifier. The non-inverting summing amplifier adds the measurement signal obtained from isolation amplifier with 1.5 V offset voltage, V_{off} generated from the offset REF2030 IC. The constructed circuit schematic is simulated by using TINA-TI-V9 software and grid current & voltage are measured to verify the measurement circuit as demonstrated in Figure 4.20. In Figure 4.20 (a) VM3 indicates an input AC voltage, VM2 is the voltage across the shunt resistor, and VM1 shows measurement output. (b) VG1 indicates the grid voltage and VM1 shows measurement output.

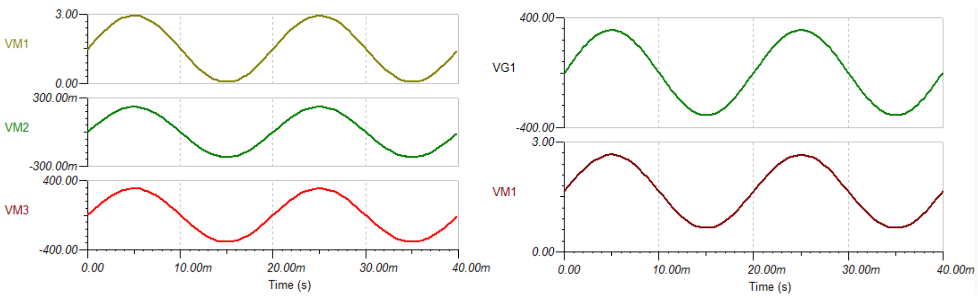

(a) (b)

Figure 4.20. AMC1301 grid (a) current & (b) voltage measurement circuit simulation results

In order to measure the PV current, current transducer LTS 15-NP that using the Hall Effect is utilized. This current transducer proposes galvanic separation between the primary circuit and the secondary circuit. The current measurement process can be conducted with increased linearity with high immunity to external interference. The output of the transducer can be calculated as

$$V_{out} = 2.5 \mp (0.625 * (I_P / I_{PN}))$$

where V_{out} is the output voltage of the transducer, I_{PN} is the primary nominal RMS current and I_P indicates the measured current. The technical specifications of the LTS 15-NP are summarized in Table 4.12 (LEM, 2017).

Table 4.12. Technical specifications of the LTS 15-NP

LTS 15-NP	
Primary nominal RMS Current	$15\ A$
Sensitivity	$41.6\ mV/A$
Load Resistance	≥ 2 kΩ
Accuracy	$\pm\ 0.2\%$
Supply Voltage	$\pm\ 5\ V$

The PV current sensing circuit utilizes a voltage divider circuit. The transducer's output voltage level is scaled down thanks to a voltage divider circuit, and then buffered via OPA320 before interfacing with the MCU as exhibited in Figure 4.21.

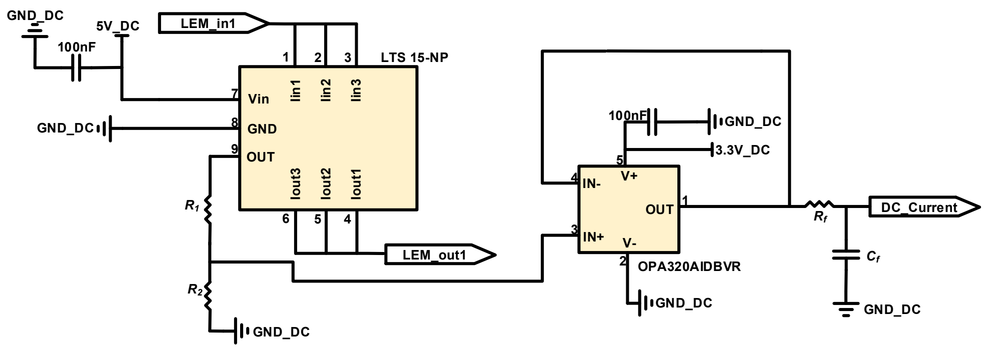

Figure 4.21. The constructed circuit schematic of LTS 15-NP to measure the PV current

4.5.5. Design of FET Driver Circuits

The UCC21520 from Texas Instrument is an isolated dual-channel gate driver with 4 A sources and 6 A sink peak current. It is formed to trigger power MOSFETs, IGBTs, and SiC MOSFETs. The application schematic of the UCC21520 gate driver is shown in Figure 4.22.

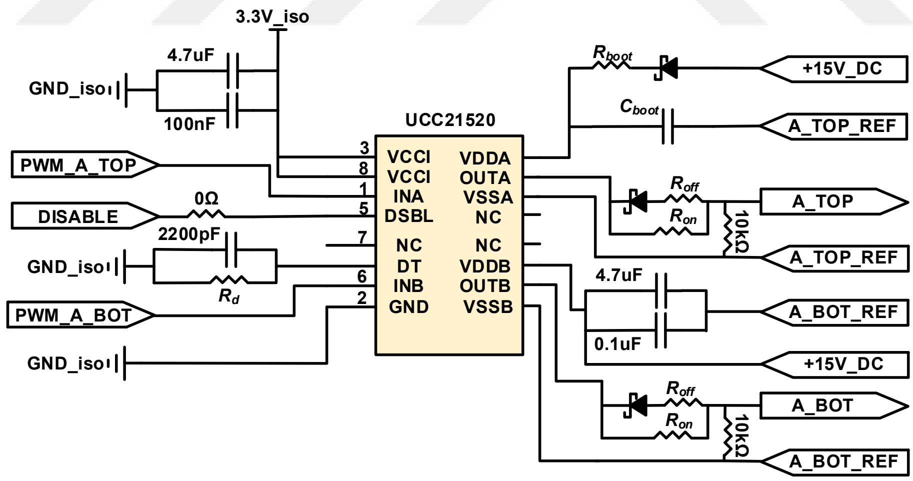

Figure 4.22. The application schematic of the UCC21520 gate driver

Design procedure includes input PWM filter, selecting external bootstrap diode and its series resistors, gate driver output resistor, selecting power supplies capacitors, and selecting a bootstrap capacitor. The design procedure can be attained from the application notes and datasheet of the UCC21520. A proper bootstrap capacitor selection is important in order to provide a stable gate drive voltage for the power transistor. On the other hand, the external gate driver resistors should be selected carefully to limit ringing resulted from parasitic inductances/capacitances, limit ringing caused by high voltage/current switching dv/dt, di/dt, and body diode reverse recovery, optimize the switching loss, and suppress electromagnetic interference (EMI) (Texas Instrument, 2017). The simulation result of the gate drive circuit is demonstrated in Figure 4.23. VG1 and VG2 indicate the input PWM signals and VM1 and VM2 show the high/low side gate drive signals.

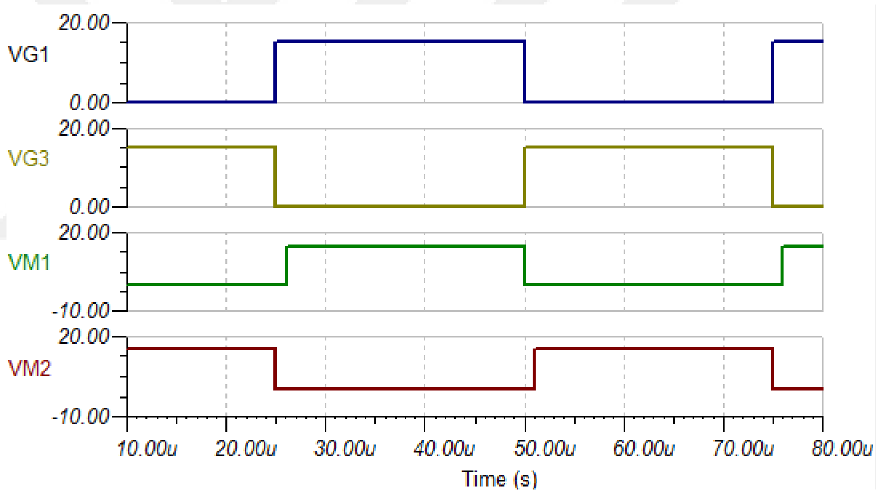

Figure 4.23. Gate drive circuit simulation result

4.5.6. Design of Analog Protection Circuit

The analog protection circuit is performed for the grid current of PV MI. The block diagrams of analog protection and fault management circuit are demonstrated in Figure 4.24. A dual-channel comparator namely TLC372 from Texas Instrument is utilized to perform protection. The signal comes from the output of the grid current measurement circuit is compared with a threshold value set by using the resistor divider circuit. If the measured signal exceeds the threshold value, the output of the TLC becomes low. In this manner, the trip signal is sent to the MCU and processed by control software.

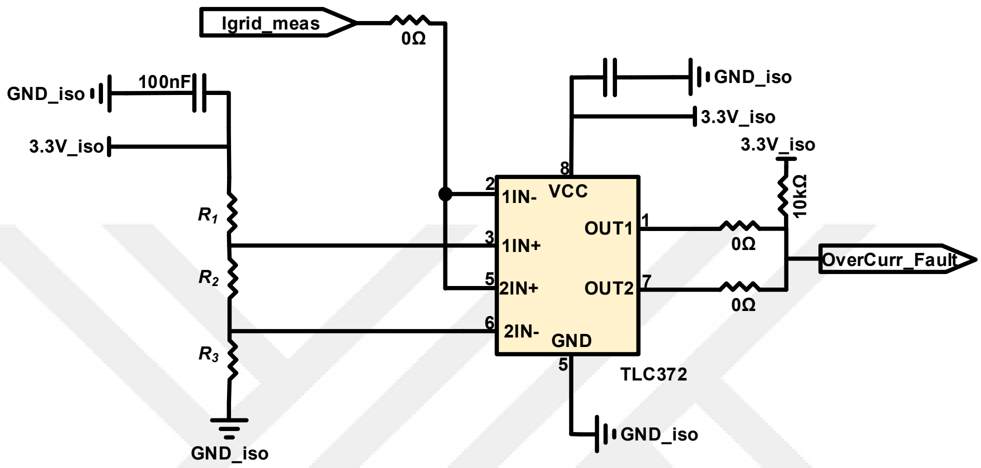

Figure 4.24. Analog protection circuit for

4.5.7. PCB Design of Control System and Power Circuit

The power circuit and control system of the PV MI prototype is implemented with a PCB. The control part includes DSP based MCU, measurement circuits, analog protection circuit, and gate driver circuits. The PCB design of the PV MI board has been performed by utilizing a PCB design software tool. The 2-D layout view and 3-D model of the designed PCB Board attained from PCB design software, which is shown in Figure 4.25 (a)-(c). PV MI board is designed with two layers utilizing surface mount technology.

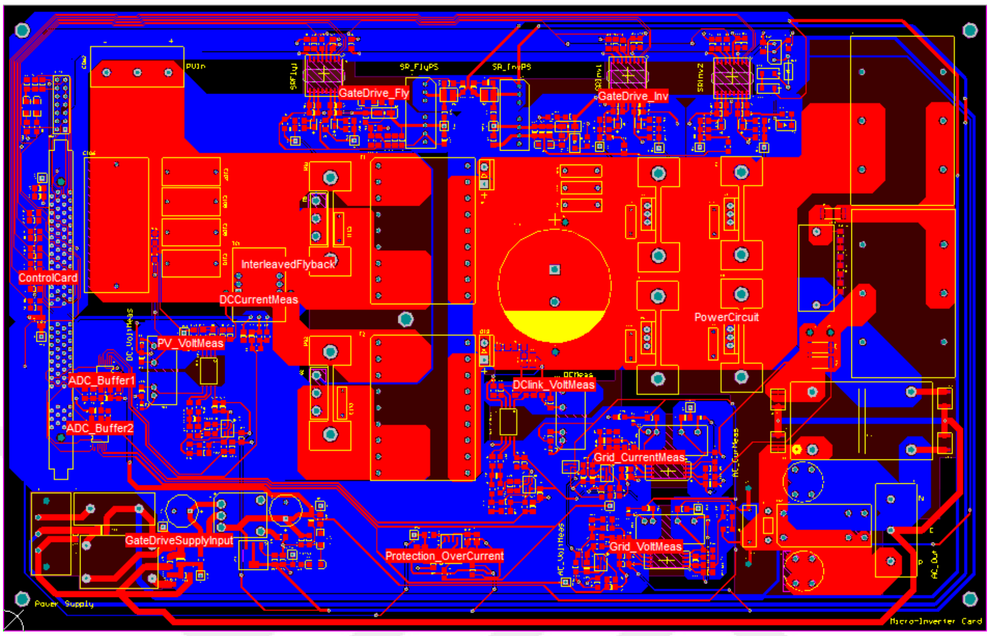
GateDrive_Fly
GateDrive_Inv
ControlCard
InterleavedFlyback
DCCurrentMeas
PV_VoltMeas
PowerCircuit
ADC_Buffer1
DClink_VoltMeas
ADC_Buffer2
Grid_CurrentMeas
GateDriveSupplyInput
Protection_OverCurrent
Grid_VoltMeas
Power Supply
Micro-Inverter Card

(a)

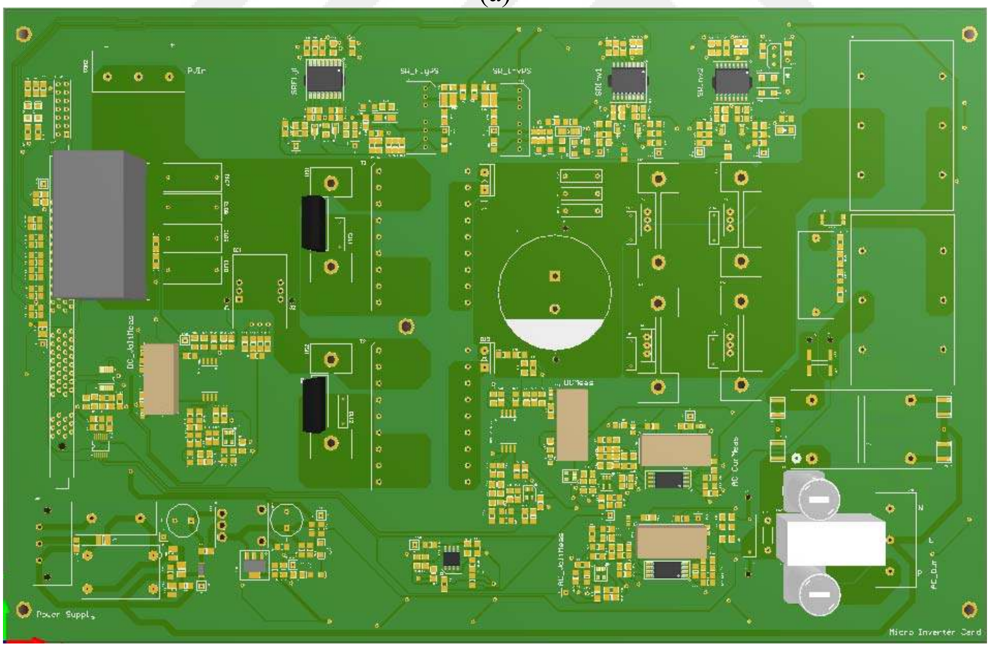

(b)

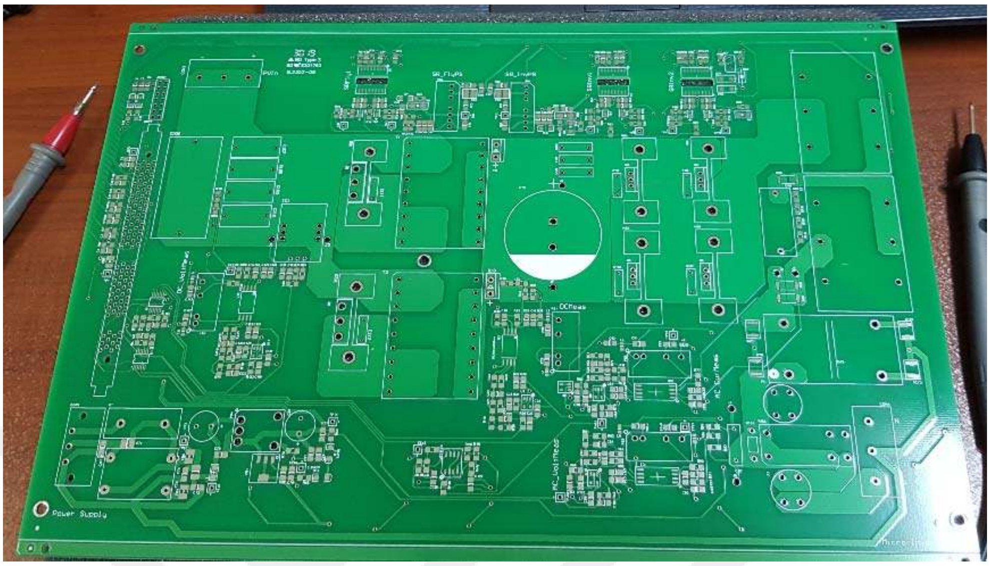

(c)

Figure 4.25. (a) The 2-D layout (b) The 3-D layout (c) The photo of designed PCB board

4.6. Hardware Implementation

After the selection of appropriate components, the power circuit and the control circuit including measurement circuits, gate driver circuits, power supply circuits, and protection circuits, are designed by using the specifications provided by the manufacturers' datasheets. Also, the application notes are utilized to design the required circuits. The hardware implementation procedure is realized by applying the steps given below.

- Power supply circuit components are soldered and the circuit is energized. Output voltages are measured in order to observe the voltage levels.
- The control card connection interface and emulator pins are soldered. After that, the control card energized and connected to the control card by using the emulator.

- The measurement circuits are soldered and then tested by applying voltage & current to the input pins. After that, the coefficients are determined by applying different voltage & current levels through the DSP based control card.
- The gate driver circuits are tested after soldering the circuit elements. The PWM signals, output signals and dead times are observed by using an oscilloscope.
- The power circuit composed of a flyback converter and full-bridge inverter is separately tested after the soldering stage.
- Finally, the system is connected to a load in order to perform the functionalities of the designed controller.
- After these stages, the system is connected to the utility grid through an autotransformer.

The photo of the constructed prototype is provided in Figure 4.26 by enumerating the main components.

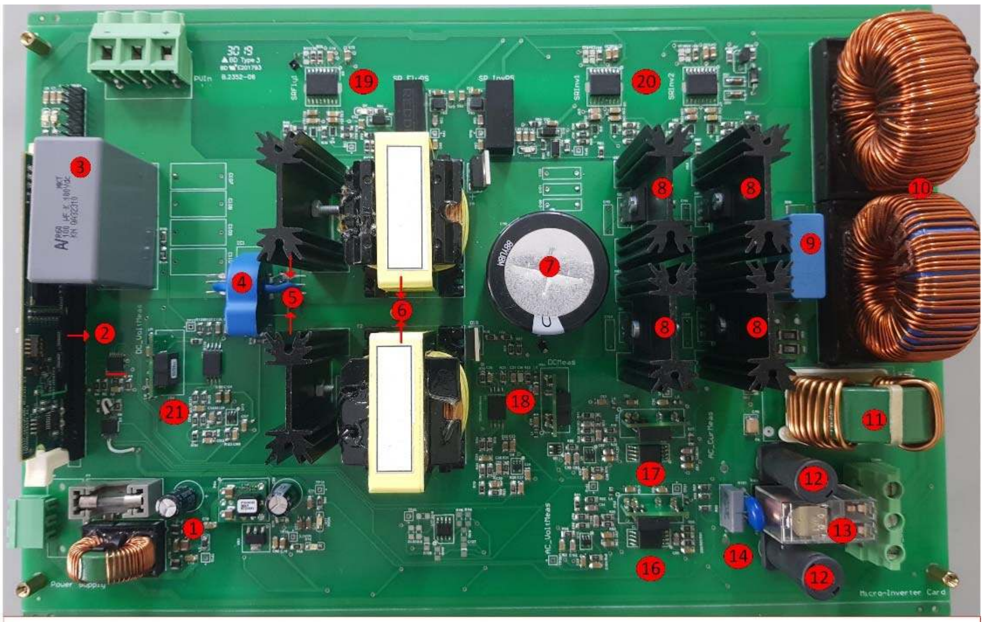

Figure 4.26. The photo of the constructed prototype

For the purpose of protecting the system from unexpected start-up faults, the system is connected to the grid by applying gradual voltage levels. A disconnector with 10 A blade fuse is utilized to connect the utility grid for the protection of the power circuit.

4.7. Development of Grid-Connected MI Software

The software of the system is developed by using the Code Composer Studio in C programming language. The system software fundamentally includes two functions namely main function and interrupt function. The main function configures the CPU and peripheral units. Also, the definition and assignment of initial values of global variables are made in the main function. The interrupt function comprises the control procedure and operational procedure. PWM interrupt is utilized for the interrupt function. The ePWM1 counter number becomes zero in every 50 μs. The interrupt function and ADC conversions are realized by using the ePWM1 counter loop. The clock speed of ADC is adjusted to 25 MHz. The flowchart of the main function of grid-connected PV MI software is demonstrated in Figure 4.27.

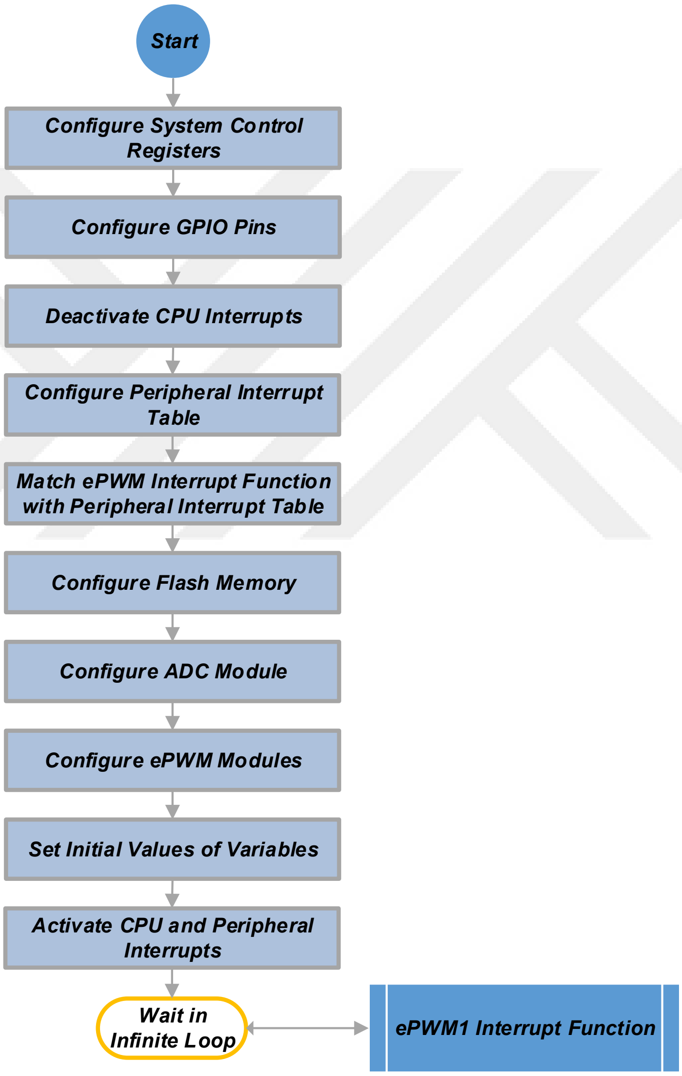

Figure 4.27. The flowchart of the main function of grid-connected PV MI software

ePWM1 is configured as a master module. ePWM2 module is operated as slave modules synchronized with ePWM1. ePWM1 and ePWM2 are configured to generate 20 kHz switching signals. ePWM3 is configured to generate 50 kHz switching signals.

4.8. Summary

Circuit description and operation principles of developed PV MI are explained in this chapter. The proposed MPPT method and improved closed-loop voltage oriented control are also introduced in this chapter. The proposed control strategy of the designed MI expressed in detail with the help of an explanatory flowchart. The experimental design requirements of a laboratory prototype of developed PV MI and preliminaries are given. The design of the power circuit and control system are presented with some mathematical equations. Furthermore, the development of grid-connected MI software is explained. Schematic designs and PCB layout of the overall system is also presented in this chapter.

5. SIMULATION MODEL OF GRID CONNECTED PV MI

Simulation of the improved PV MI is conducted by employing the PSCAD/EMTDC electromagnetic transient software. In order to validate the presented PV MI, various scenarios are executed. The scenarios are determined to measure the performance of PV MI under steady-state conditions and dynamically changing conditions. In addition, it is checked whether the developed PV MI provides the grid requirements. The simulation results exhibited that the presented PV MI is satisfactorily compatible with grid-connection standards. Moreover, performance measurement results illustrate the superiority of the system in terms of efficiency and dynamic response.

5.1. Validation of PV Module

In order to assess the robustness of the developed PV MI system, an accurate PV module model is a fundamental component. In this study, a generalized five parameters model of a PV module is carried out by using the PSCAD/EMTDC software environment with FORTRAN coding. A set of constants related to PV module material, which are supplied by the manufacturer are employed to fulfill the model. The one diode model presents robust stability between validity and convenience.

The nonlinear current/voltage relation of a PV module that extracted by using the single diode model can be analytically described as (Celik and Acikgöz et al., 2007)

$$I_{pv} = I_{ph} - I_o * \left(e^{\frac{V_{pv}+I_{pv}*R_S}{AV_t}} - 1 \right) - \frac{V_{pv}+I_{pv}R_S}{R_{sh}}$$

The five parameters of the model can be expressed by the photogenerated current in standard test conditions (STC) I_{ph}, dark saturation current in STC I_o, series resistance R_s, the shunt resistance R_{sh}, is of the PV module, and diode quality factor A. V_t denotes the junction thermal voltage.

I/V & *P/V* characteristics of the simulated PV module are given in Figure 5.1. The simulated PV module has 260 W maximum power output at standard test conditions (1000 W/m^2 irradiation and 25 ˚C).

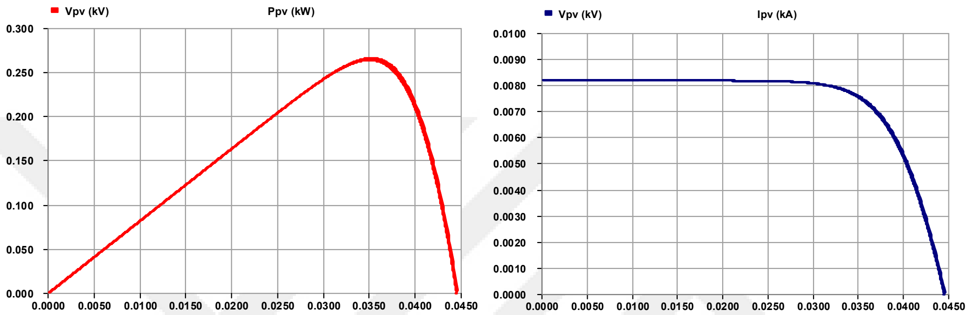

(a) (b)

Figure 5.1. I/V & P/V characteristics of the simulated PV module

I/V & P/V characteristics of the simulated PV module under different irradiation levels are given in Figure 5.2.

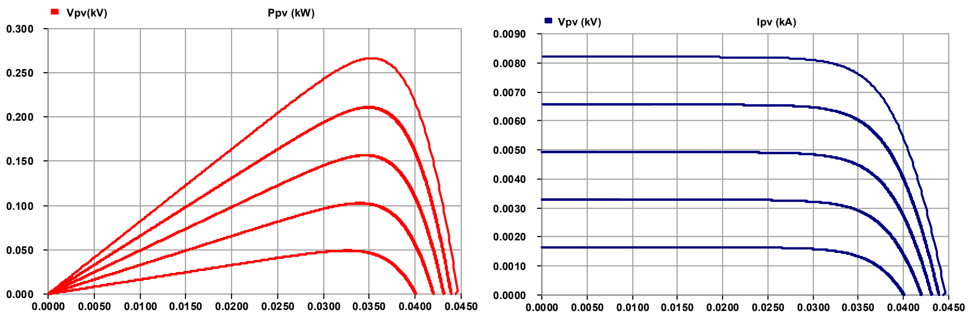

(a) (b)

Figure 5.2. I/V & P/V characteristics of the simulated PV module under different irradiation level

5.2. Different Case Studies for Developed MI System

The presented PV MI system that rated at 250 W (220 V/50 Hz) is simulated in order to carry out the performance evaluation. The power circuit of the simulated model is exhibited in Figure 5.3.

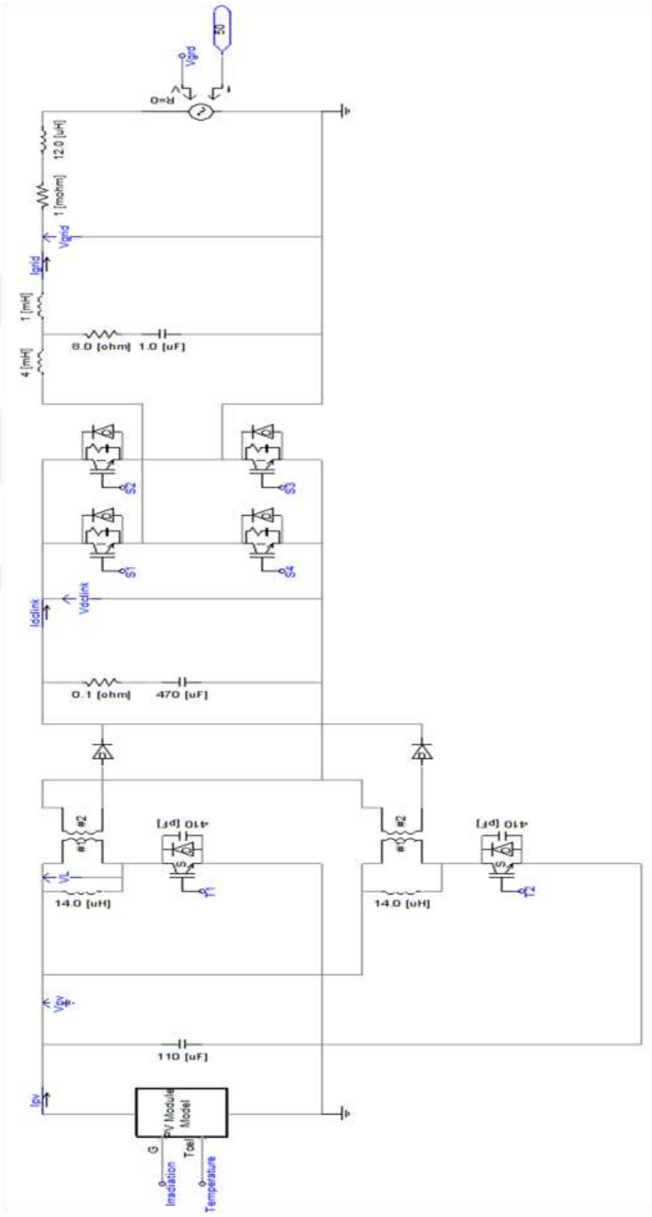

Figure 5.3. The power circuit of the simulated model

The performance of the developed PV-MI system is measured under different load conditions. The main power circuit parameters of the proposed system are tabulated in Table 5.1. The main objective of the simulation study is to assess the dynamic and steady-state response of the developed MI configuration under different operating load conditions. In this manner, different irradiation levels are utilized to evaluate the overall efficiency and robustness of the system. Moreover, the effect of deep radiation changes is analyzed to observe the MPPT and inverter output power injection performance.

Table 5.1. Technical specifications of the system

Flyback Converter	
Input capacitor	110 μF
Magnetizing Inductance	14 μH
Switching Frequency	50 kHz
Inverter	
Rated power	350 VA
DC link voltage	380 V
DC link capacitor	470 μF
Switching frequency	20 kHz
LCL-filter	L_{if} =4 mH, L_g = 1 mH, C_f = 1 μF, R_d = 8 Ω
Grid voltage amplitude	311 V
Grid frequency	ω_o = 2π x 50 rad/s

5.2.1. Steady State Response of Developed MI

The performance of the presented PV MI system for 1000 W/m^2 solar irradiation is given in Figure 5.4. The results at full load operation reveal that the maximum efficiency of the developed MI is 96.92%. The output current distortion level is measured below 2% for proposed MI systems. In addition, it is observed that the power factor value of higher than 0.99 is achieved at full load operation. When the start-up of the system is considered, it takes 0.2 seconds to reach a steady-state operation.

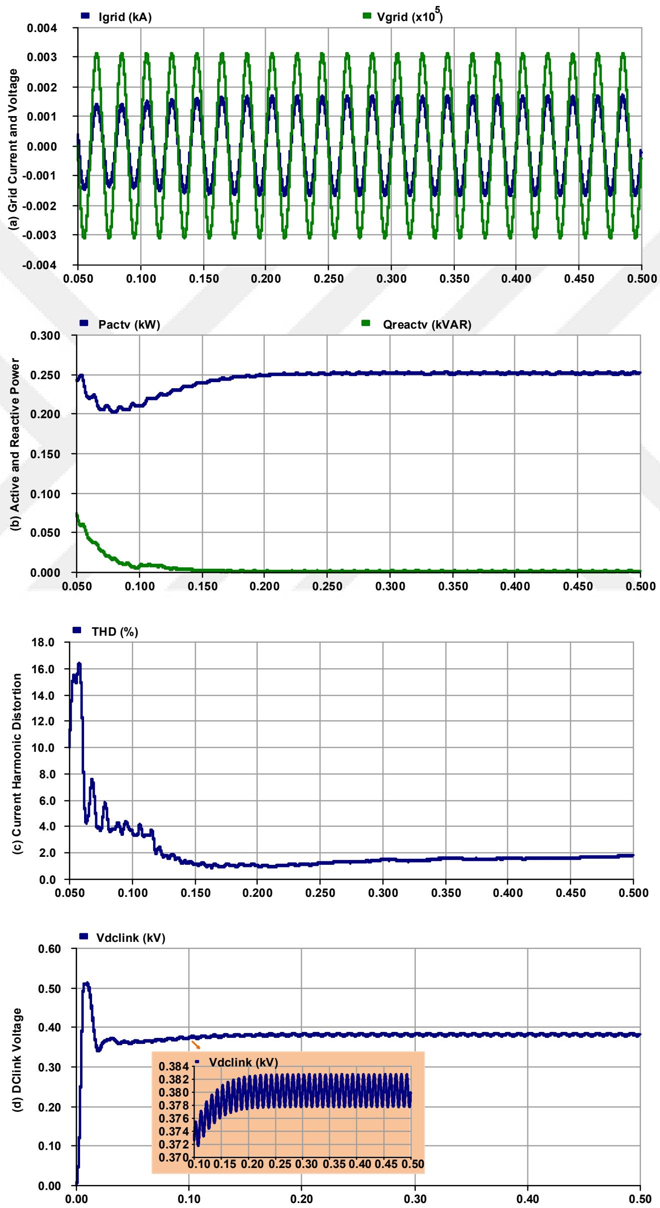

Figure 5.4. Performance of presented MI system under 1000 W/m^2 solar irradiation

The performance of the presented PV MI system is also investigated for 800 W/m^2 solar irradiation as exhibited in Figure 5.5. The results reveal that power factor higher than 0.99, THD under 2.3% and efficiency 96.63% are achieved.

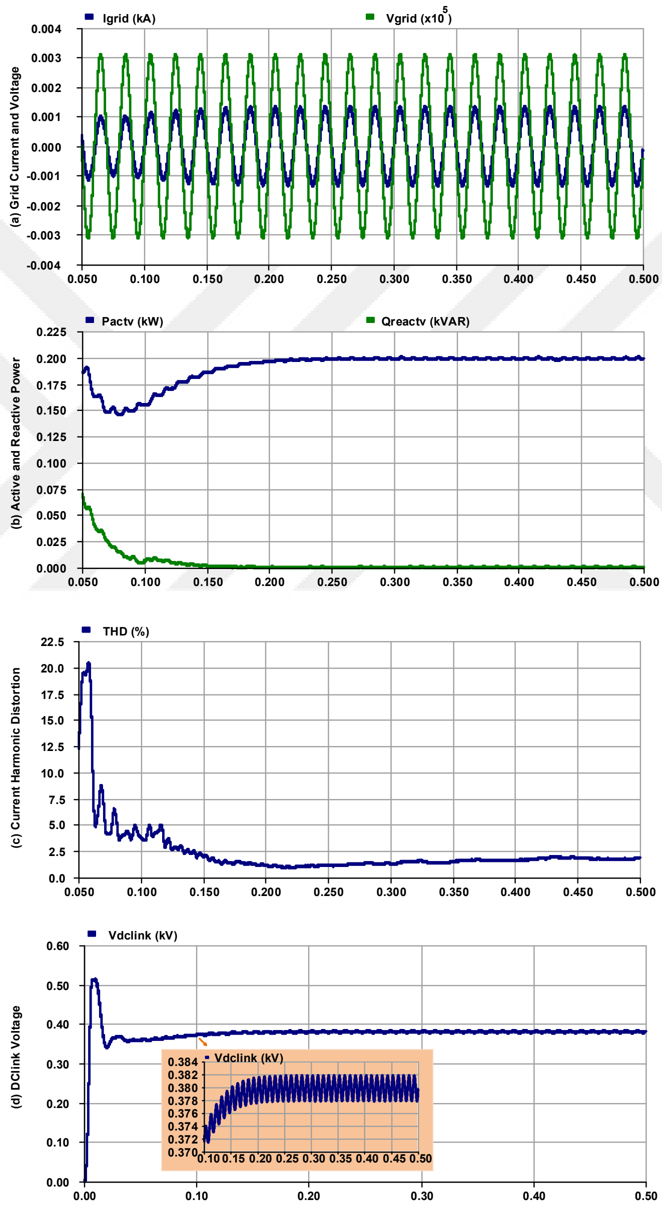

Figure 5.5. Performance of presented MI system under 800 W/m^2 solar irradiation

Additionally, Figure 5.6 illustrates the performance of the presented MI system for 400 W/m^2 solar irradiation.

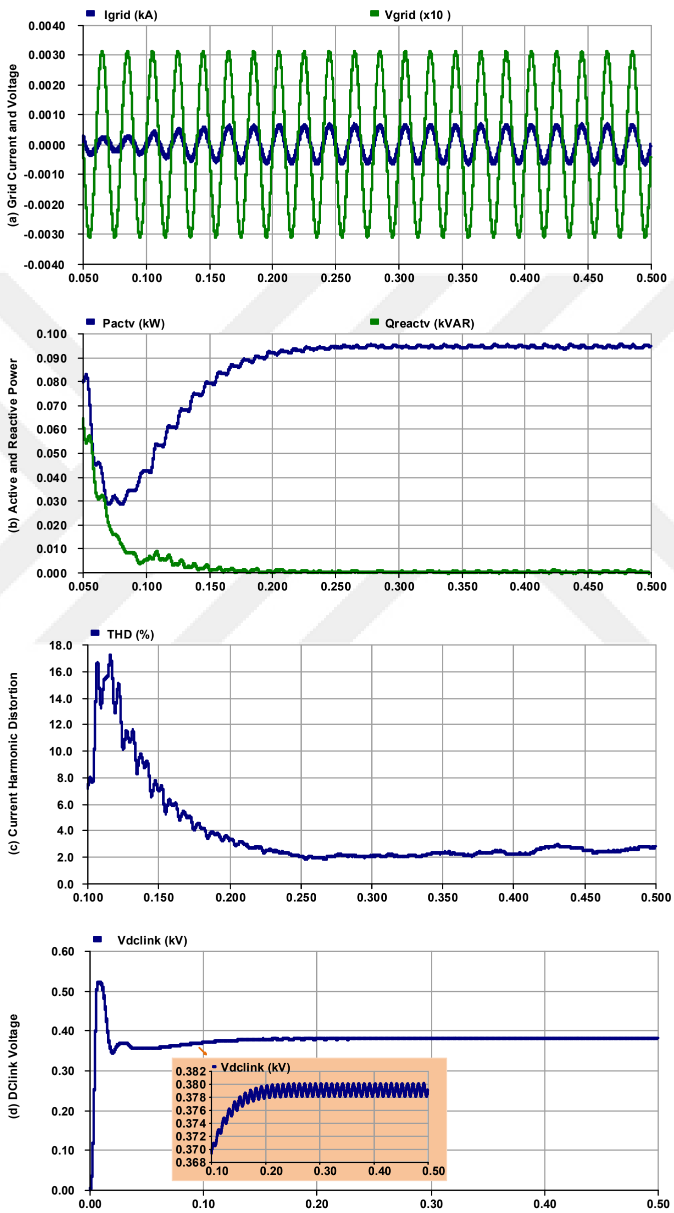

Figure 5.6. Performance of presented MI system under 400 W/m^2 solar irradiation

The presented PV MI system demonstrates high performance even in low load conditions. The results at 40% of load operation reveal that the maximum efficiency of the proposed MI is 91.3%. The output current distortion level is measured below 3% for developed MI systems. In addition, it is observed that the power factor value of higher than 0.97 is achieved at low load operation. When the start-up of the system is considered, it takes 0.2 seconds to reach a steady-state operation.

Selective harmonic compensators are also mentioned for the improved controller structures. In order to obtain a pure reference signal, selective harmonic compensators are utilized for the cancellation of different harmonic levels. The compensators can be basically expressed as the tuned filters different harmonic levels. The signal obtained from the subtraction of generated reference current signal and the actual current signal is analyzed and compensated for the minimization of harmonic levels. The structure can be considered as a dual compensator. The performance of the presented harmonic compensator is demonstrated in Figure 5.6. The selective harmonic compensators are activated at 0.5 seconds and the output current THD level decreased remarkably as shown in Figure 5.7. The harmonic level is diminished from 3.5% to 1%. In order to show the instantaneous change in output current and harmonic level, a small time interval is taken and provided in Figure 5.7.

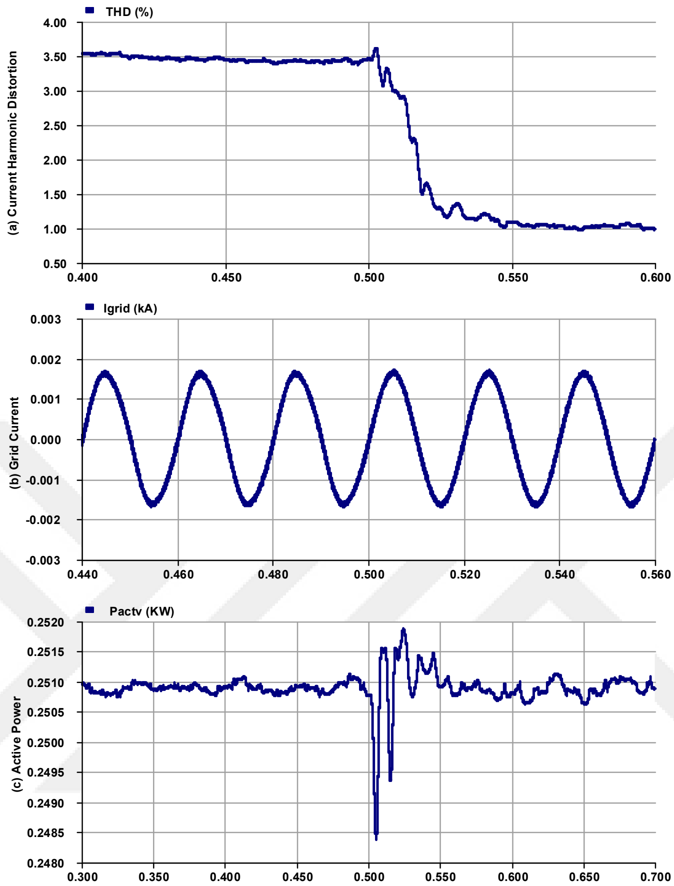

Figure 5.7. The performance of the presented harmonic compensator

5.2.2. Dynamic Response of Developed MI

In order to illustrate the dynamic response of the system, the solar irradiation level is changed from 1000 W/m^2 to 800 W/m^2 and to 600 W/m^2. As shown in Figure 5.8, the developed structure exhibits high performance under varied atmospheric conditions.

The results show that the developed PV MI system demonstrates a remarkable dynamic response even under rapidly changing irradiation levels. It is clearly confirmed that inverter output current is almost pure sine wave in moments of radiation change. During the instantaneous changes of irradiation levels, the value of THD instantly increases to a high value such as 8% and 10%, respectively. However, it can be observed from the figure that the current THD is restored in a cycle.

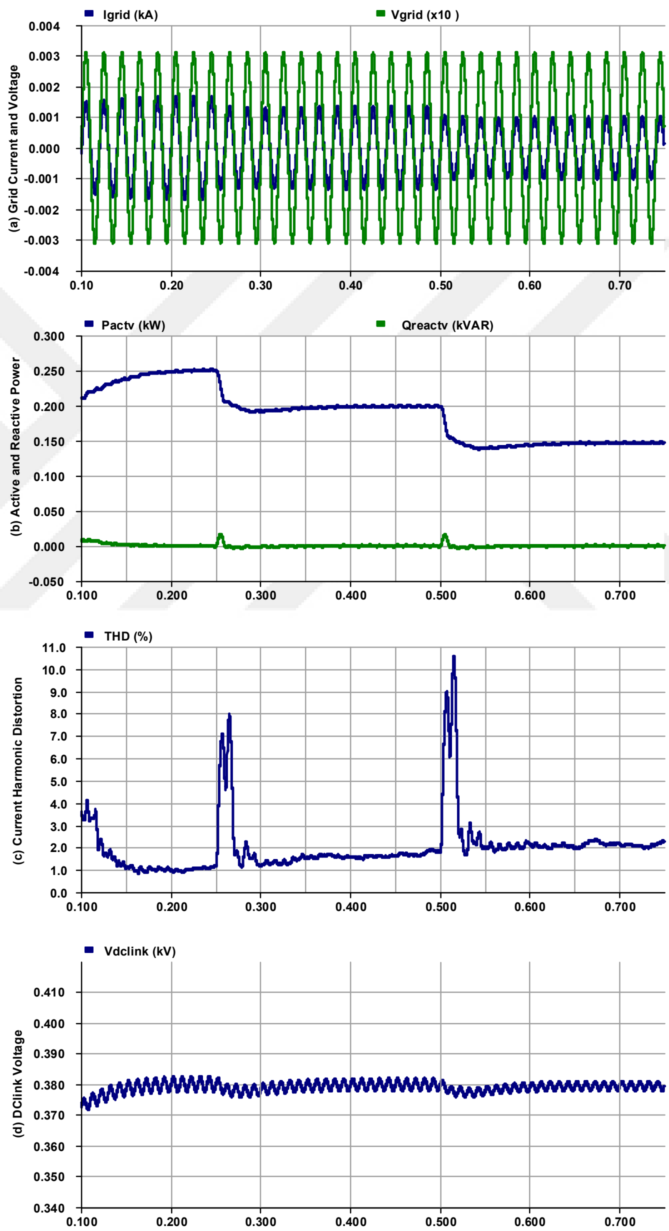

Figure 5.8. Dynamic response of the presented MI under variable conditions

The performance of the proposed MPPT technique is illustrated in Figure 5.9.

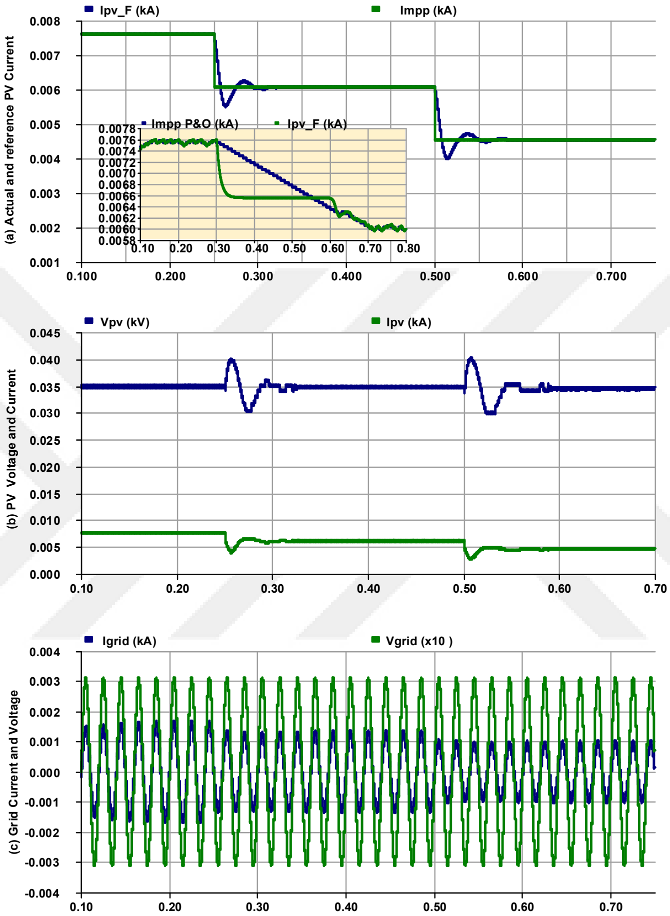

Figure 5.9. The performance of the proposed MPPT technique under rapidly changing conditions

It can be clearly concluded that the proposed MPPT illustrates superiority against the rapidly changing conditions. In addition robustness of the MPPT technique has a positive effect on the dynamic response of the overall system. When the P&O MPPT technique is considered, if the perturbation of the algorithm is adjusted to small scales, it takes much time to reach the maximum operating point.

It can be seen from Figure 5.9, it takes nearly 0.4 seconds to reach the maximum operating point for the P&O MPPT method. Hence it causes instabilities in inverter output current and deteriorate the system operation. On the other hand, the increase in convergence speed, improved tracking accuracy, and reduction of oscillations contribute to the overall system efficiency and reliability.

Furthermore, to prove the performance of the overall system, deep changes are applied to the irradiation level. The solar irradiation level is changed from 1000 W/m^2 to 400 W/m^2 and to 800 W/m^2. As shown in Figure 5.10, developed PV MI exhibits high performance under a deeply changed radiation level. Instantaneous deep changes constitute high THD levels for a short time. For the worst-case recovery time of the system takes 0.1 seconds, and the output current THD level decreased under 5%.

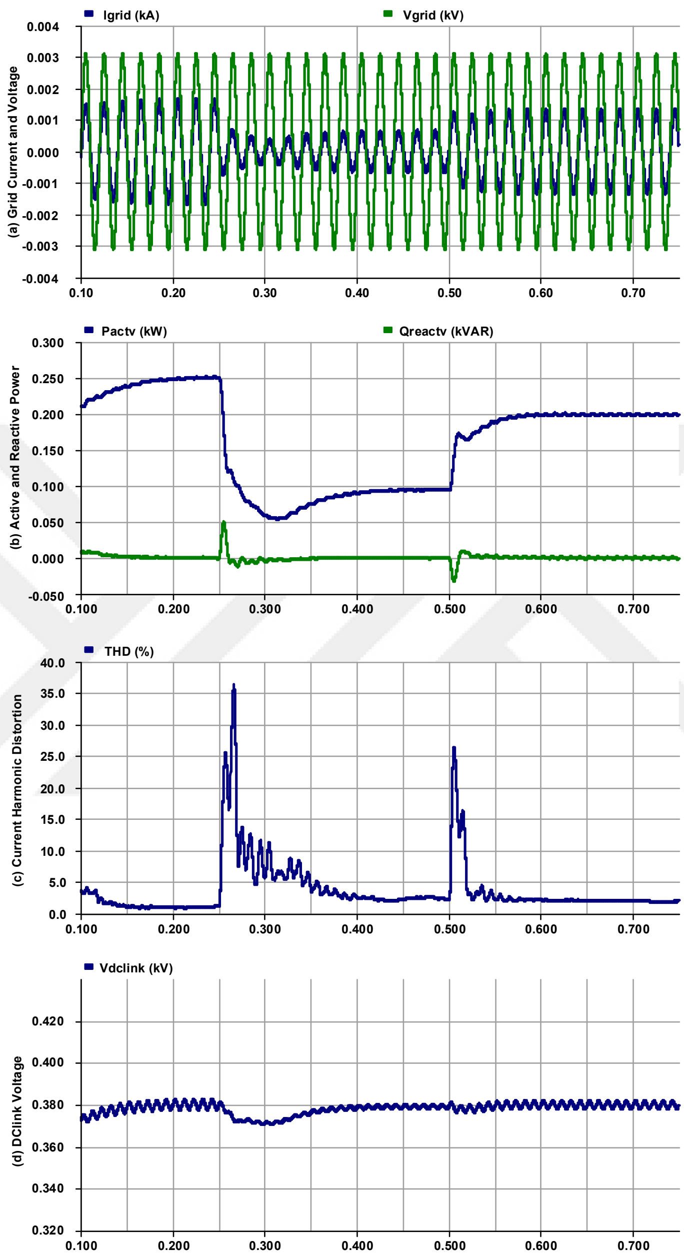

Figure 5.10. Dynamic response of the presented MI under deeply changing conditions

The dynamic response of the proposed MPPT technique under deeply varying conditions is shown in Figure 5.11. The presented MPPT technique exhibits a considerable development with regard to tracking accuracy and dynamic response. When the conventional P&O and INC MPPT techniques are considered, the number of oscillations is substantially reduced. The rates of overshoots are significantly reduced thanks to the proposed MPPT technique.

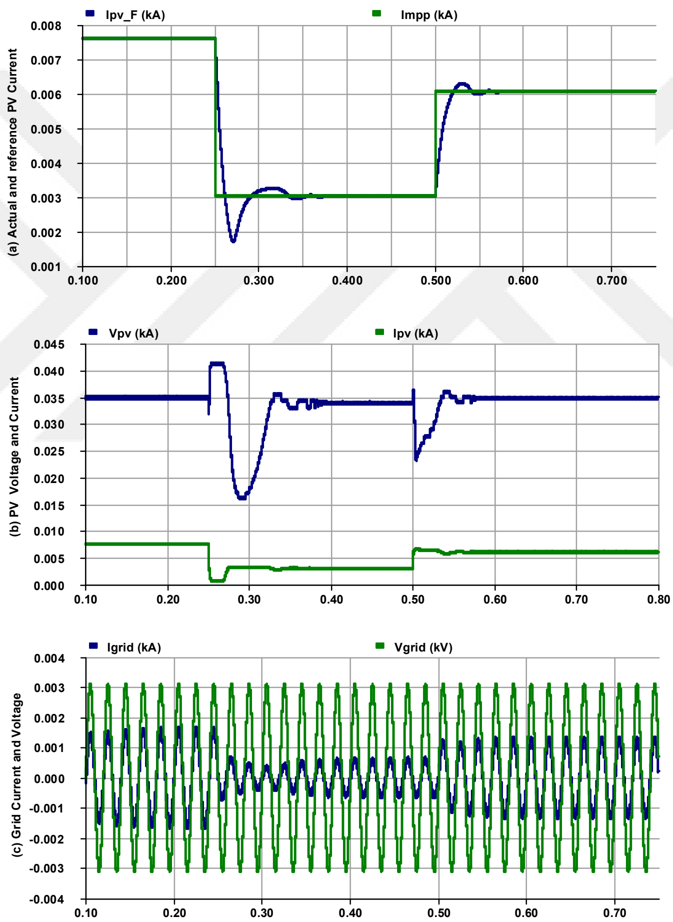

Figure 5.11. The performance of the proposed MPPT technique under deeply changing conditions

5.2.3. Dynamic Grid Support Capability

The presented PV MI system is able to inject reactive current during fault transients with an islanding detection algorithm. The dynamic grid support capability of the developed PV-MI system is tested by changing the desired reactive power amount as shown in Figure 5.12 and Figure 5.13, sequentially.

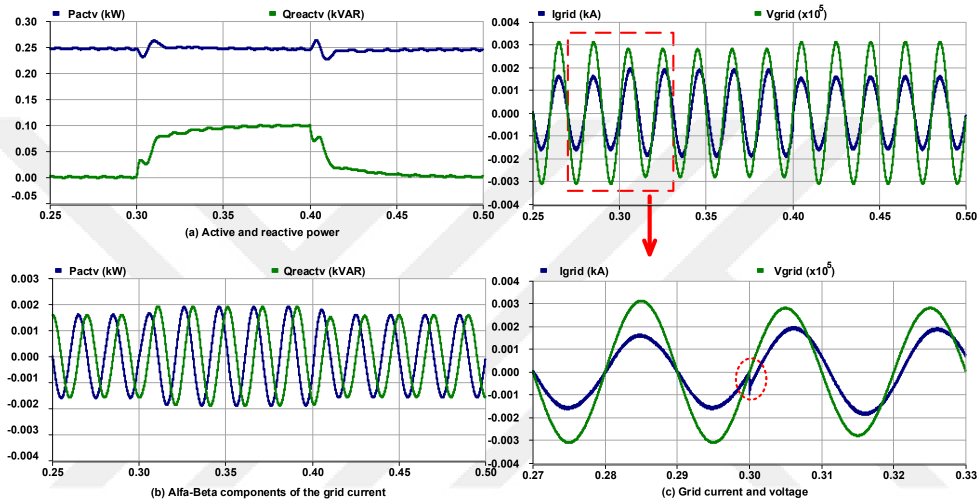

Figure 5.12. 100 VAR reactive power support

Constant active power injection strategy is utilized to fulfill the grid requirements. The required amount of reactive power can be injected to the utility grid with maximum power extracted from PV modules. A peak current protection is also added to the system for the sake of ensuring the safe operation of the inverter. When a voltage fault detected in the utility grid, the system starts to provide reactive power to the grid according to the determined demand. Dynamic grid support capability is ensured for the MI applications with 0.8 leading right through to 0.8 lagging. The maximum active power extracted from the PV module also is injected to the grid at the same time.

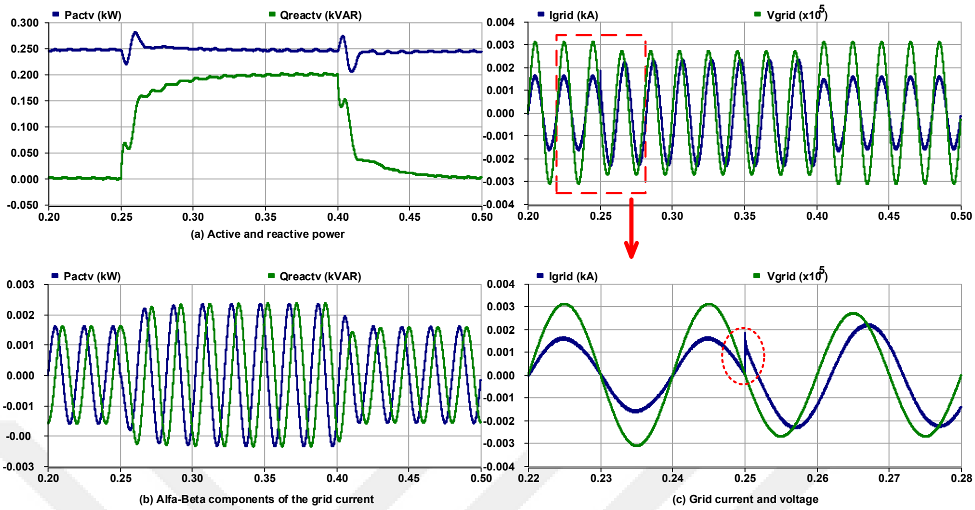

Figure 5.13. 200 VAR reactive power support

In order to assess the LVRT capability of PV MI, the peak value of the grid voltage is derated to nearly 200 V. The response of the presented PV MI is demonstrated in Figure 5.14. The rise in PV MI's output current can be observed from the figure. It took a short transient period to reach the steady-state value for the MI output current.

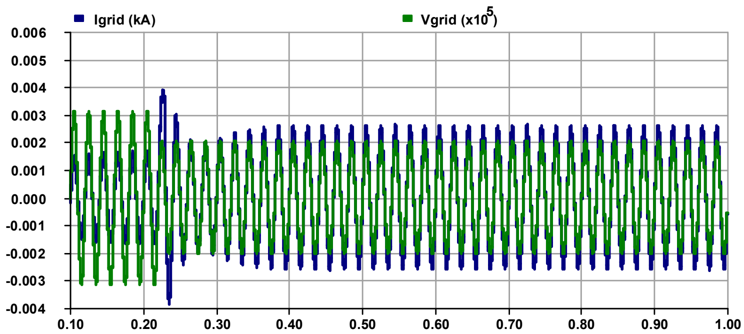

Figure 5.14. The LVRT capability of PV MI

5.3. Summary

In this chapter, the presented PV MI is verified through simulations by conducting different case studies. The system is tested under various irradiation levels. The obtained efficiency rates are given in Figure 5.15.

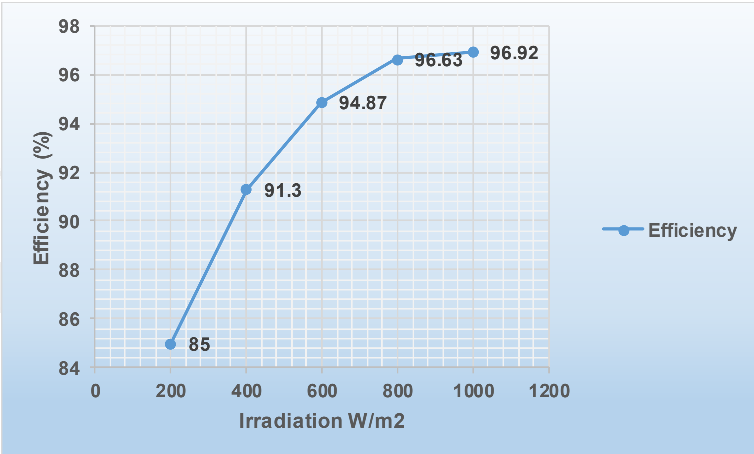

Figure 5.15. Efficiency rates for different irradiation values

The results at 1000 W/m^2 operation reveal that the maximum efficiency of the proposed MI is 96.92%, and the minimum efficiency rate at 200 W/m^2 is achieved as 85%. In addition, the output current THD is almost kept under 3% with PF greater than 0.9. The performance values illustrate that the modeled system can be a promising candidate for implementation. On the other hand, the developed PV MI system has a dynamic grid support capability feature, which is confirmed by ensuring the desired reactive power demand. LVRT capability of the system is also tested by applying a fault to the grid voltage.

The dynamic response of the proposed MPPT technique is also tested. The presented MPPT technique exhibits a considerable enhancement with regard to tracking accuracy and dynamic response. When compared to conventional P&O and INC MPPT techniques, the number of oscillations is substantially reduced. The rates of overshoots are significantly reduced thanks to the proposed MPPT technique.

6. EXPERIMENTAL RESULTS AND DISCUSSION

This section presents the experimental results of implemented PV MI. The constructed prototype is verified under steady-state and dynamic changing atmospheric conditions. The obtained results are also discussed in detail to highlight the promising aspects of the system.

6.1. Overview of Experimental Study

The experimental studies are achieved by using the laboratory facilities of the Çukurova University Electrical and Electronics Engineering Department. In order to assess the functionalities of the constructed prototype, a load group is utilized. In addition, the constructed system is connected to the utility grid through an autotransformer.

The photo of the constructed prototype and the experimental set-up in the laboratory are demonstrated in Figure 6.1 and Figure 6.2, sequentially. In Figure 6.2. The test stage of the constructed system with a resistive load is illustrated. The constructed prototype is connected to a gradually adjustable load group. Firstly, the system is tested for low voltage levels. The controller functions are experienced and the results are observed. This stage is performed to prevent the risk of card damages. Finally, the system is connected to the utility grid by increasing the voltage level step by step.

The experimental results include output current, output voltage, DC-link voltage, and gate drive signals are observed with Tektronix MSO3034 oscilloscope. The active power, reactive power, and harmonic levels are realized by using the Fluke 1760 power quality analyzer that meets the requirements of the IEC 61000-4-30 standards. The measurement results are registered with 200 ms averages. Due to recording with 200 ms averages, the transient responses could not be observed as in the simulation studies. The power and harmonic measurement results are recorded simultaneously by using a program provided by the Fluke. The output voltage is measured with a differential probe namely Tektronix P5200A and the output current is measured with a current transducer namely Fluke 80i-110s.

In order to measure the performance of the MI two parallel-connected DC power supply are utilized which gives the opportunity of providing different power levels. The performance of the MPPT technique can not be measured due to not having a solar array simulator in the laboratory. However, different power levels and transient response of the system can be tested with the constructed experimental set-up. The real-time emulator provides the chance of external adjustment of reference values during the operation of the system.

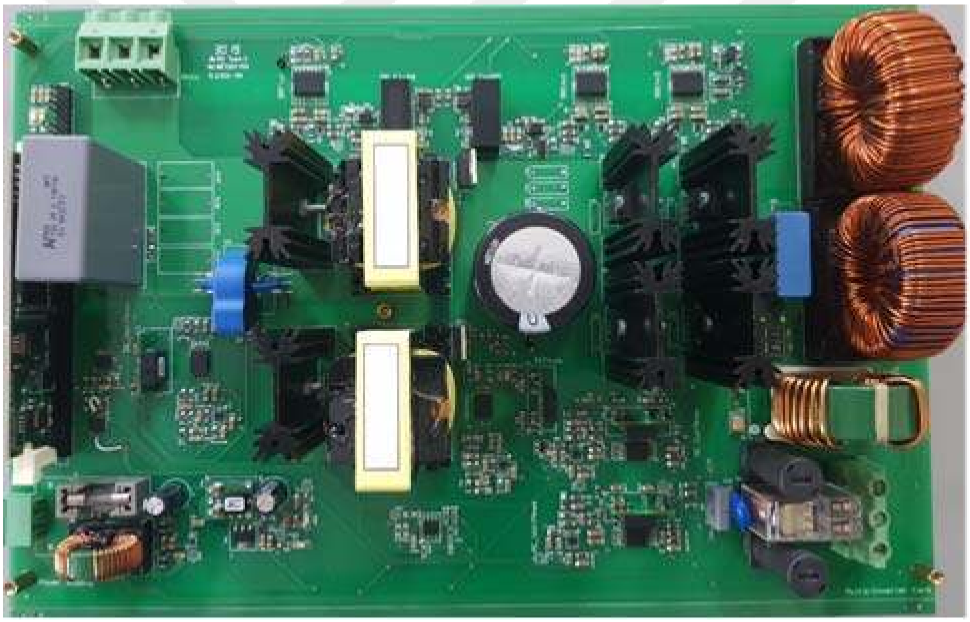

Figure 6.1. The photo of the constructed prototype

Some of the capacitors and other through-hole components are soldered to the bottom side of the card in order to ensure enough space for measurement probes.

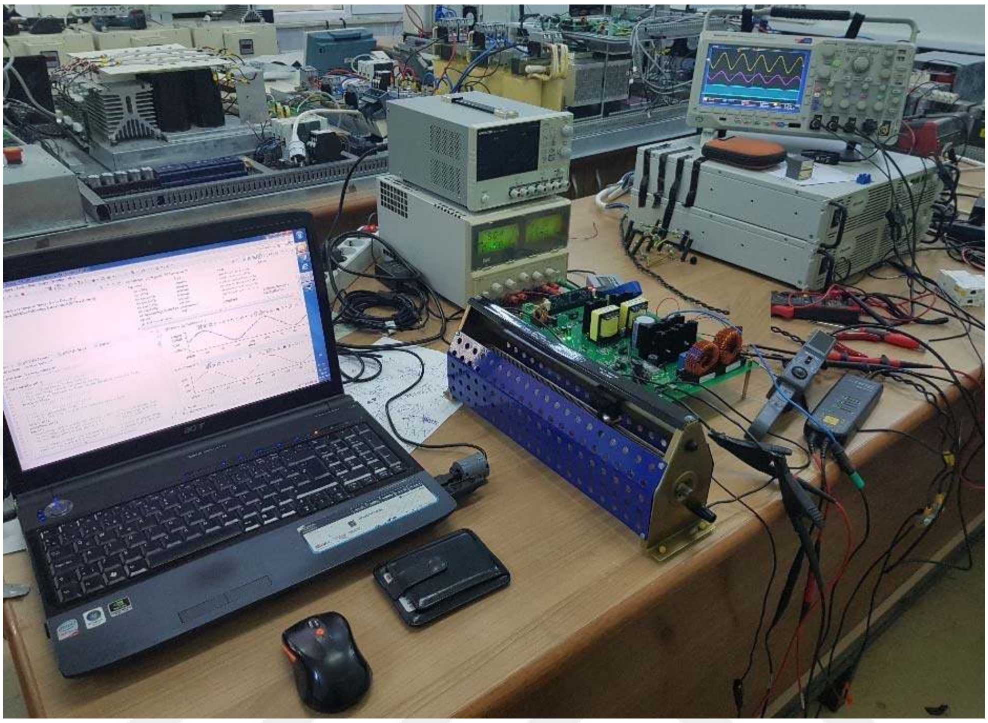

Figure 6.2. The photo of the experimental set-up

The measurement signals are also observed via real-time monitoring through the Code Composer Studio software. All the card signals are monitored and accessed by using a system trace emulator. Hence, the measured signals are compared with the observed waveforms from the oscilloscope in order to perform an accurate analysis.

6.2. System Parameters

The overall experimental system is composed of a power supply, measurement devices, the constructed prototype, and the utility grid. The experimental prototype of the constructed system is demonstrated in Figure 6.3

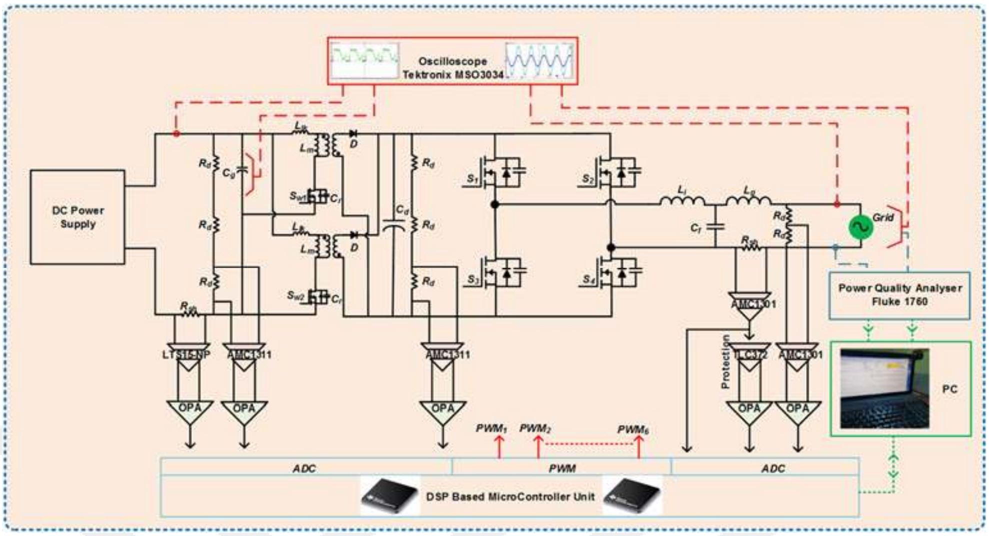

Figure 6.3. The experimental prototype of the constructed system

The pieces of equipment list that utilized for the constructed systems is given in Table 6.1.

Table 6.1. The equipment list that utilized for the constructed system

Oscilloscope	Tektronix MSO3034
Power Quality Analyzer	Fluke 1760
Differential Probe	Tektronix P5200A
Current Probe	Fluke 80i-110s.
Power Supply	TDK
Multimeter	Fluke 28II

The parameters of the constructed experimental set-up are given in Table 6.2.

Table 6.2. The parameters of the constructed system

General PV MI specifications	
Max. DC Power	270 W
Input Voltage	30-50 V
Transformer Parameters	
Core and bobbin	E 42/21/15
Primary magnetizing inductance	14 μH
Primary turns / Secondary turns	8 / 102
Primary wire cross-sections	1.885 mm^2
Secondary wire cross-sections	0.628 mm^2
Capacitor Values	
Input Capacitor	110 μF
DC-link Capacitor	470 μF
LCL Filter Parameters	
Inverter Side Inductance	4 mH
Grid Side Inductance	1 mH
Capacitance	1 μF
Damping Resistance	8 Ω
EMI Filter Parameters	
Coupled Inductor Inductance	1 mH
Capacitance (Ceramic Cap.)	4 * 2200 pF
Protection Components	
Fuses	2 * 5 A
Relay	Gen Purpose DPDT 5 A
Switching Devices Parameters	
STF100N10F7	100 V / 80 A
IPA65R190CFDXKSA1	650 V / 17.5 A

The maximum output power of the MI is designed to be 250 W and the expected efficiency level is determined to be higher than 90%. Hence the input power of the MI can be increased up to 270 W. In both experimental and simulation studies, the input power is increased around the 260 W. The design parameters and accordingly selected circuit elements are specified on the basis of calculations given in chapter 4. In addition, the controller parameters are determined via the simulation studies. However, some control parameters and selected components are manipulated for the sake of performance and reliability improvement. The measurement circuits and gate driver circuit elements are determined with the help of application notes provided by the manufacturers. In these circuits filtering components are modified with regard to noise values seen on the measurement signals. On the other hand, a simple control circuit is designed to control the output relay in order to disconnect the MI from the utility grid in case of a fault. The designed control circuit includes a MOSFET, zener diodes, and resistors. The zener diodes are utilized for protection against the excessive voltage. The resistors are utilized for current limitation. An analog protection circuit is also designed by using a comparator. The output of the analog protection circuit is latched with a trip signal in the MCU and the fault signal is constituted. The fault signal is sent to the disable pins of the gate driver ICs. All of the measurement ICs and gate driver ICs are isolated for providing safe operation.

6.3. Experimental Results of Developed MI System for Different Case Studies

In this part, the constructed prototype of the MI is validated through case studies. The case studies are realized to test the steady-state and transient response of the MI. The drain-source voltage of the flyback converter's switch, flyback converter input voltage and current, DC-link voltage, output current, and voltage of the inverter, injected active and reactive power, and output current THD are measured. It is observed that the simulation results and the experimental results are compatible.

6.3.1. Steady State Response of Developed MI

In this section, the system is tested at different power levels and the steady-state response of the system is observed. The input power of the system is adjusted to 260 W, which corresponds to the 1000 W/m^2 irradiation level. When the results are examined, the drain-source voltage of the flyback converter's switch reaches to 70 V. The duty cycle of the flyback converter is limited to 0.5 to maintain the operation of converter in DCM. This voltage value is compatible with the calculated value, which is proper for the safe operation. The applied input voltage is 34.5 V, with the current value of 7.55 A. The DC-link voltage oscillates around 380 V. The obtained results can be observed from Figure 6.4.

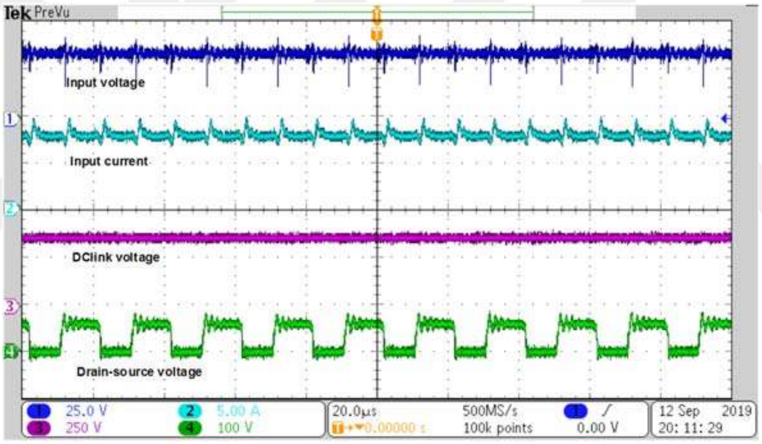

Figure 6.4. The measurement results for input voltage&current, dc-link voltage and drain-source voltage of the switch

When the output current and voltage of the MI is investigated, the output current and voltage RMS value equal to 1.09 A and 224 V, respectively. The power factor is achieved to be higher than 0.99. The waveforms of the current that injected to the grid and the grid voltages are exhibited in Figure 6.5.

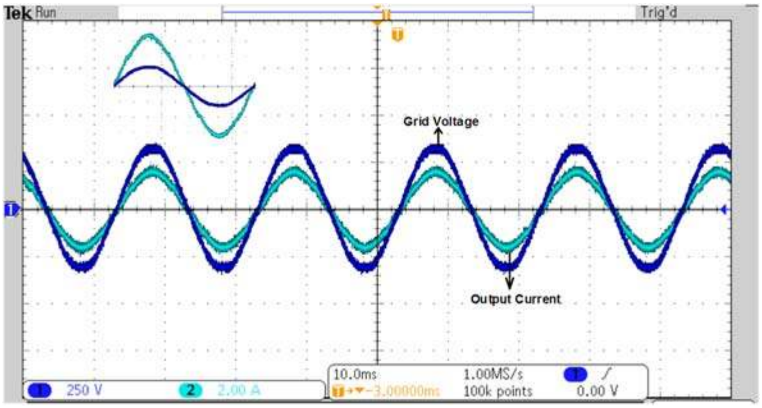

Figure 6.5. The output current and voltage of constructed MI

Also, the amount of active power that injected to the utility grid is simultaneously measured by using the power quality analyzer. The results show that the amount of the injected power reaches 243 W for full load operation as demonstrated in Figure 6.6.

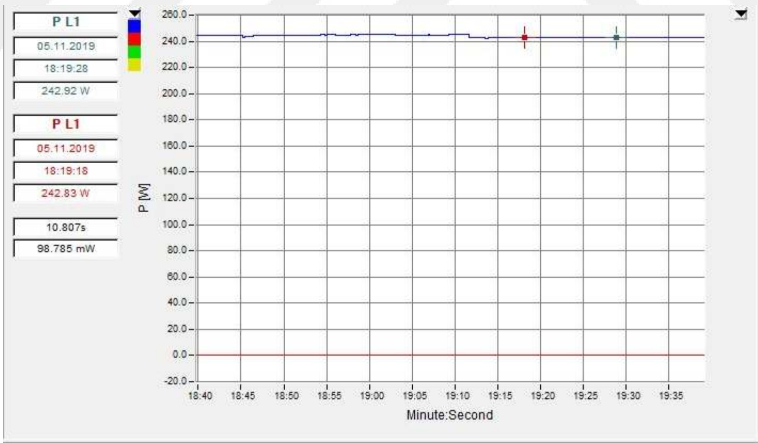

Figure 6.6. Amount of the injected active power

The output current distortion level is also measured via the power quality analyzer, the results demonstrate that the harmonic level is 2%, which is compatible with the rates specified in the grid standards. The output current THD is demonstrated in Figure 6.7.

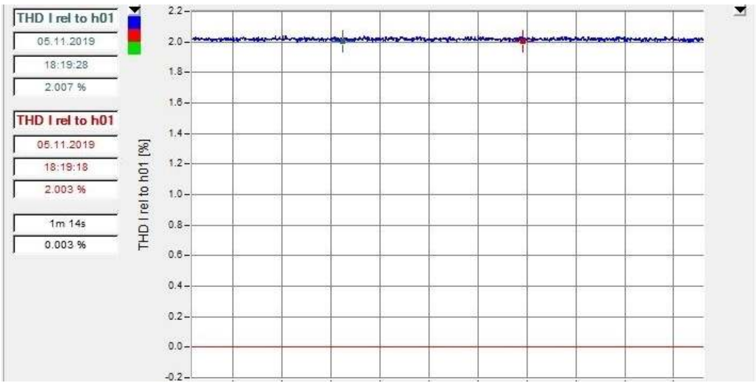

Figure 6.7. The output current THD

The system is also tested for 800 W/m^2, the input power of the system is nearly 208 W. When the results are investigated, the drain-source voltage of the flyback converter's switch reaches to 70 V. This voltage value is compatible with the calculated value, which is proper for the safe operation. The applied input voltage is 34.5 V, with the current value of 6.03 A. The DC-link voltage oscillates around 380 V. The obtained results can be observed from Figure 6. 8.

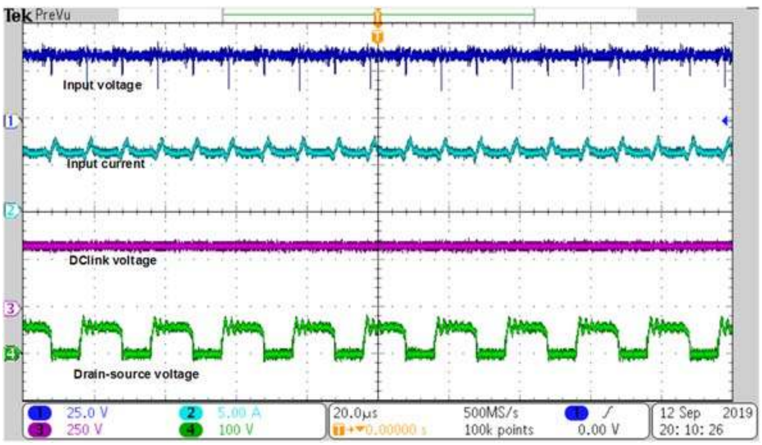

Figure 6.8. The measurement results for input voltage&current, dc-link voltage and drain-source voltage of the switch

For the input DC power level of 208 W, the output current and voltage RMS value equal to 0.87 A and 224 V, respectively. The power factor is achieved to be higher than 0.99. The waveforms of the current that injected to the grid and the grid voltages are demonstrated in Figure 6.9.

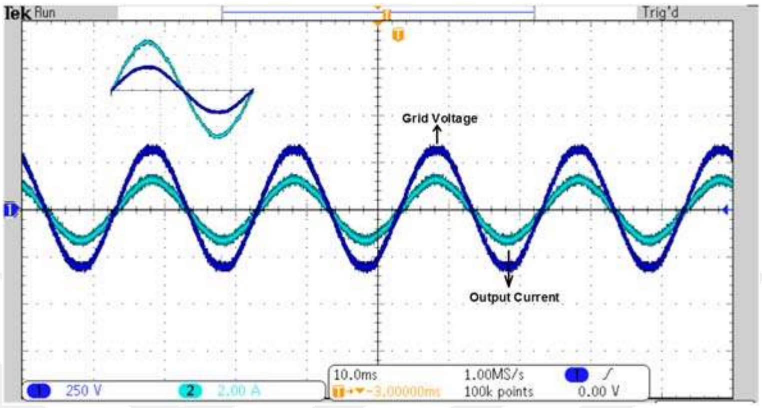

Figure 6.9. The output current and voltage of constructed MI

The injected active power level to the utility grid is simultaneously measured by using the power quality analyzer. The results show that the amount of the injected power reaches 193 W for 800 W/m^2 operation as depicted in Figure 6.10. It can be observed that the performance of the MI is almost the same as the operation at 1000 W/m^2.

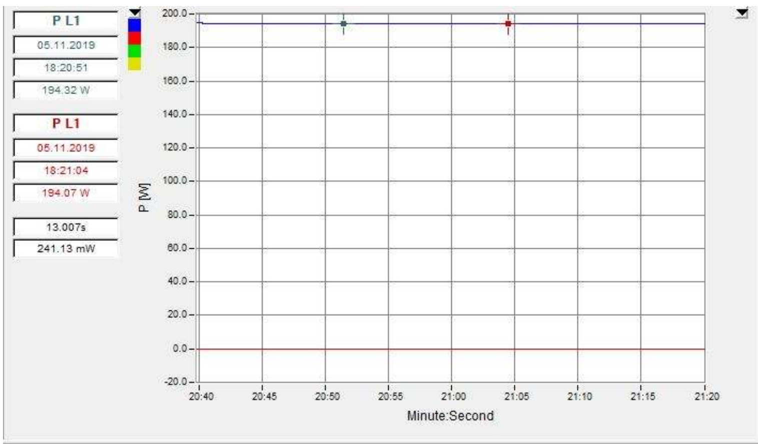

Figure 6.10. Amount of the injected active power

The output current THD is also measured by utilizing the power quality analyzer, the results show that the harmonic level is around 2.4%, which is compatible with the rates specified in the grid standards. The output current THD is depicted in Figure 6.11.

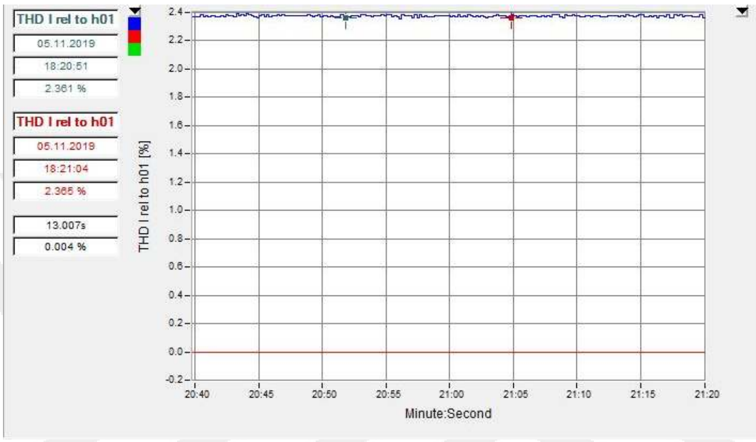

Figure 6.11. The output current THD

Finally, the system is tested for 115 W input DC power. When the results are investigated, the drain-source voltage of the flyback converter's switch reaches 65 V. This voltage value is compatible with the calculated value, which is proper for the safe operation. The obtained results can be observed in Figure 6.12.

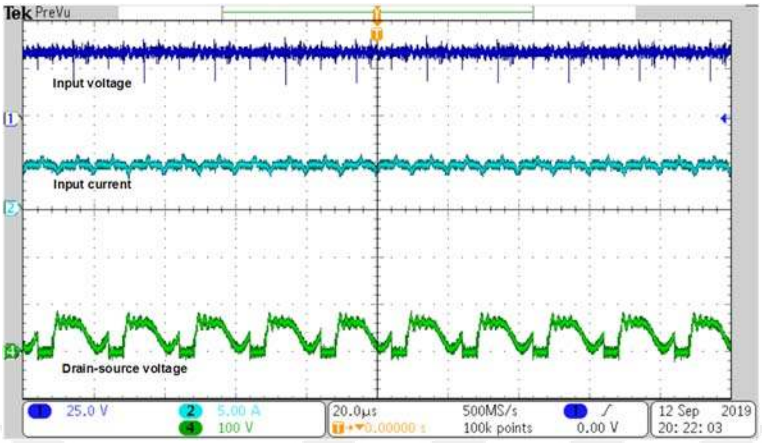

Figure 6.12. The measurement results for input voltage&current, and drain-source voltage of the switch

When the output current and voltage of the MI is investigated, the output current and voltage RMS value equal to 0.44 A and 224 V, respectively. The power factor is achieved to be greater than 0.96. The waveforms of the current that injected to the grid and the grid voltages are exhibited in Figure 6.13.

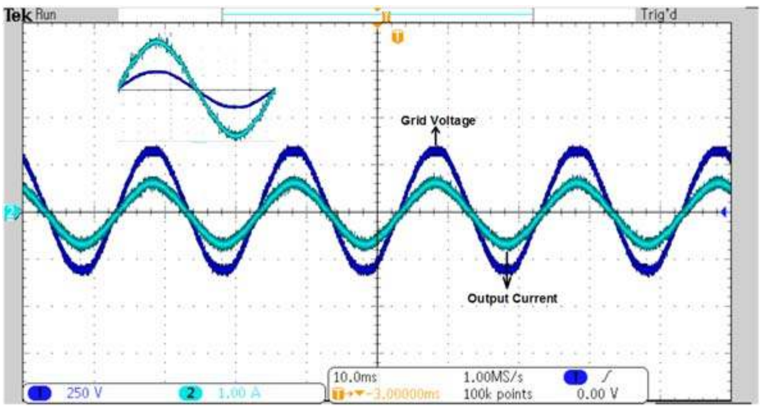

Figure 6.13. The output current and voltage of constructed MI

The injected active power level to the utility grid is simultaneously measured by utilizing the power quality analyzer. The results show that the amount of the injected power reaches 99 W for low power operation as demonstrated in Figure

6.14. It can be observed that the performance of the MI reduces as the power level decreases.

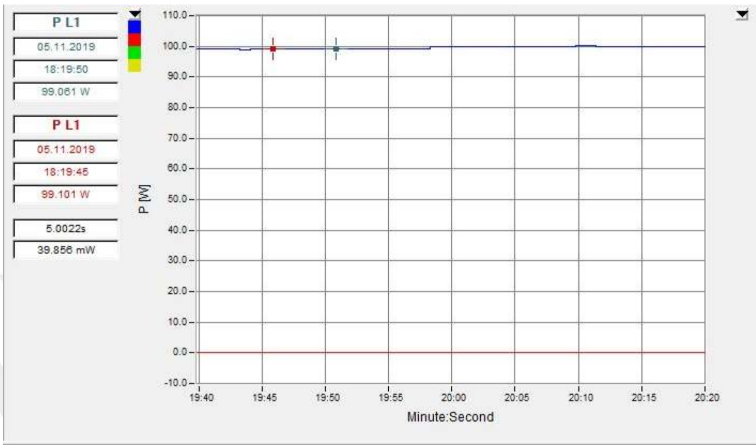

Figure 6.14. Amount of the injected active power

The form of the output current also deteriorates as can be observed from Figure 6.13. The measurement results that taken demonstrates that the harmonic level is around 2.8%. The output current THD is illustrated in Figure 6.15.

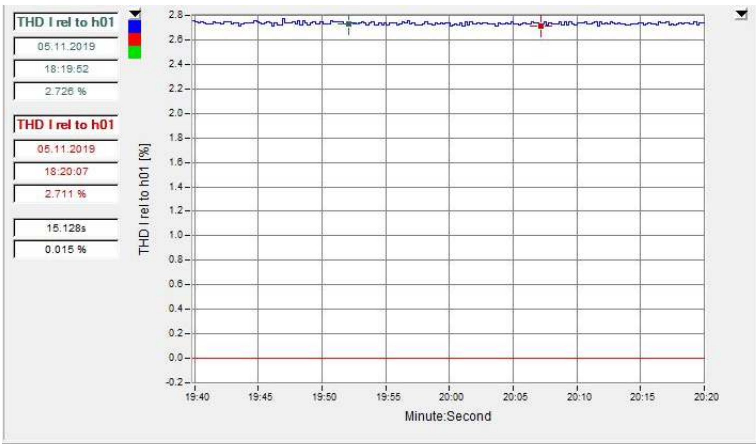

Figure 6.15. The output current THD

It can be concluded that the output current is distorted as the power level decreases. The THD level of the output current increases by nearly 1% for the 40% load operation when compared to full load operation. In addition, a decrement in the efficiency level is observed for the low load condition. The efficiency rate decreases to 83% when the MI is operated at 20% of input DC power. Especially the THD level of the output current increased noticeably. Also, the power factor decreased to 0.9. In view of this, the low input power operating performance of the designed prototype should be increased. The results obviously demonstrate that the system introduces high power quality in the output electrical characteristic. This is crucial for mitigating the impact of distributed generation on the utility grid. The operation above 40% of the input DC power provides almost pure sine output current. The amount of reactive power injected to the grid is also kept almost zero. The attained efficiency level is greater than 90% for the operation above 40% of the input DC power.

6.3.2. Dynamic Response of Developed MI

A start-up procedure for the system is adjusted. Firstly, the output relay is closed and the grid voltage value is measured. The grid voltage value must be between the specified limits. Input voltage is also measured to control if it is higher than the minimum specified value. After that, the phase locked loop (PLL) is checked for synchronization. The SOGI PLL generates the quadrature signals used in power calculations. During the start-up of the converter, the PWM signals are sent to FET drivers. A sequence is carried out in order to activate the low-side MOSFET turn on first. This sequence is constituted for the proper operation of the bootstrap configuration.

In order to illustrate the dynamic response of the system, the input DC power level is changed from full rated power to 40% of rated power and then 80% of rated power. The reference control parameters including reference current for flyback converter and reference power for inverter controller are manipulated externally by using the software. The response of the system is observed via the power quality analyzer and the oscilloscope. The output current and voltage waveforms can be seen from Figure 6.16 when the full rated input power reduced to 40%.

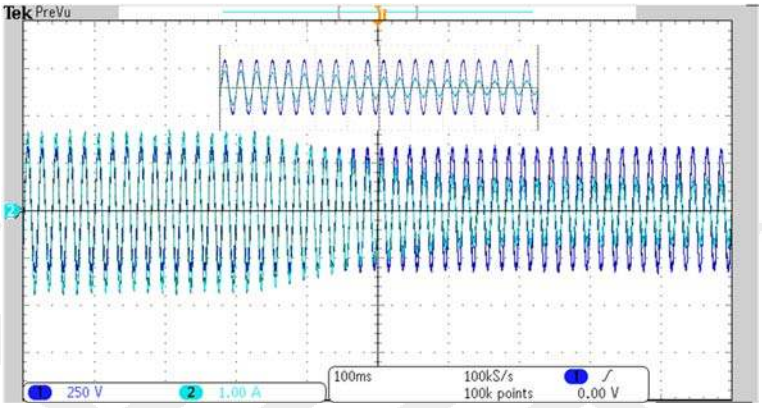

Figure 6.16. The output current and voltage waveforms when the full rated input power reduced to 40%

When the input DC power increased from 40% of rated power to 80% of rated power the output current and voltage waveforms are varied as illustrated in Figure 6.17.

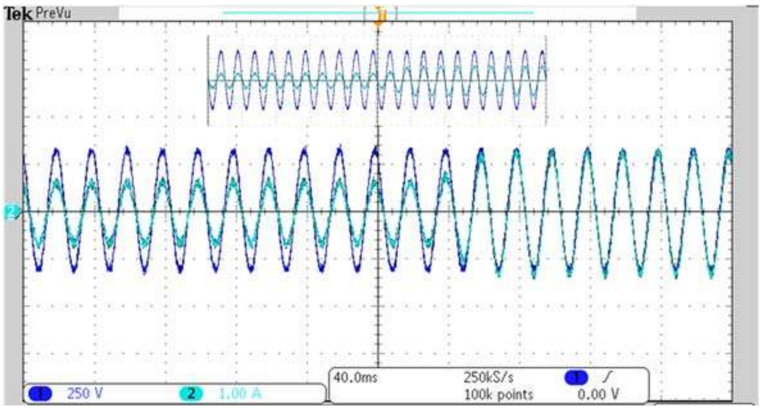

Figure 6.17. Variation of output current and voltage of MI for the input DC power increased from 40% of rated power to 80% of rated power

The output active power of the system is changed as demonstrated in Figure 6.18 when the input DC power level is changed from full rated power to 40% of rated power and then 80% of rated power.

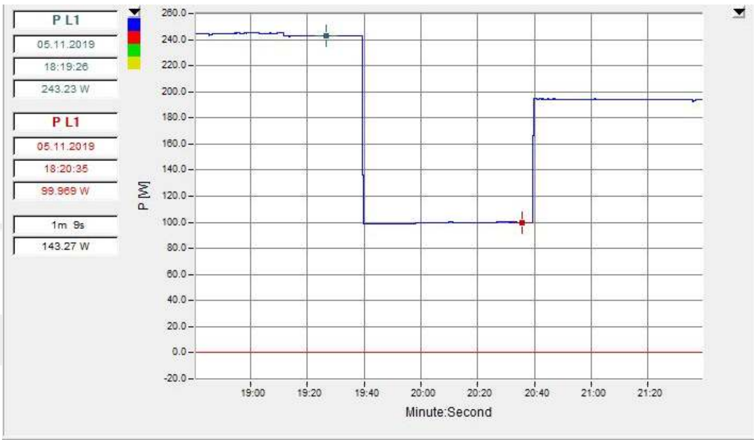

Figure 6.18. The injected active power for the different input DC power levels

The instantaneous peak values cannot be observed as seen in simulation studies due to recording the results with 200 ms averages. It can be reported that the dynamic response of the constructed prototype is considerably improved. The developed structure exhibits high performance under varied load conditions. The results show that the developed PV MI system demonstrates a remarkable dynamic response even under rapidly changing conditions. It is clearly confirmed that inverter output current is almost pure sine wave in moments of radiation change. The reference active power rate is updated instantaneously and the system can provide proper output power for the new reference value.

It should be noted that the dynamic response of the system can be checked more accurately by utilizing a solar array simulator as input DC power supply. The MPPT performance will directly affect the overall performance of the system. The small perturbations cause a delay in creating a constant reference active power value for the inverter side controller. This will slow down the response of the controller.

Moreover, the stability of the converter will be negatively affected. Hence, the controller does not correspond to the instantaneous power level changes immediately and not able to transfer the same amount of energy to the grid. This situation results in shut down the system and loss of available energy. The proposed MPPT technique eliminates the slow response of the conventional methods and provides a fast dynamic response for the utilized controller structure. The proposed MPPT technique is tested for several case studies in simulation studies.

6.3.3. Dynamic Grid Support Capability

The dynamic grid support capability of the developed PV-MI system is tested by changing the desired reactive power amount. The aim is determined to keep connected to the utility-grid during faults and feed-in of reactive power. In Figure 6.19, the reference value of the reactive power is adjusted to inject 200 VAR.

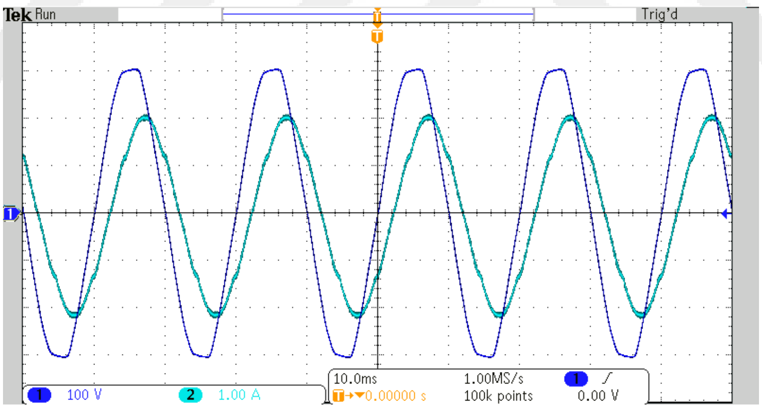

Figure 6.19. Grid current and voltage for 200 VAR reactive power injection

The injected amount of reactive power is also measured with the power quality analyzer. The results demonstrate that the system can inject the desired reactive power amount with the generated active power as shown in Figure 6.20.

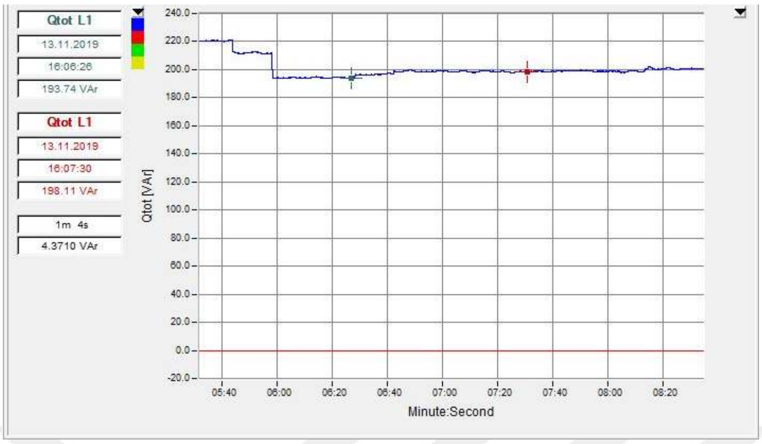

Figure 6.20. The injected amount of reactive power

In Figure 6.21, the reference value of the reactive power is adjusted to inject 100 VAR and output voltage and current waveforms are demonstrated.

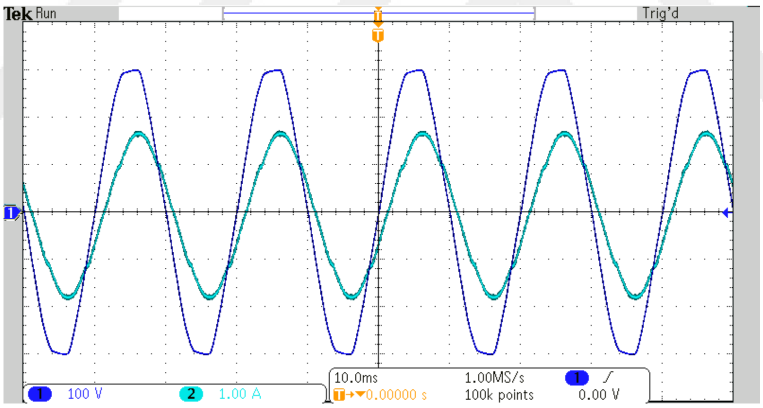

Figure 6.21. Grid current and voltage for 100 VAR reactive power injection

The amount of injected reactive power is verified by using the power quality analyzer and the obtained result is shown in Figure 6.22.

Figure 6.22. The injected amount of reactive power

Constant power reactive power injection strategy is utilized to fulfill the grid requirements. Dynamic grid support capability is ensured for the MI applications with 0.8 leading right through to 0.8 lagging. The required amount of reactive power can be injected to the utility grid with maximum power extracted from PV modules. When considering the state-of-the-art, there is no requirement for the low voltage level. However, the dynamic grid support in low voltage grids becomes necessary, when the high penetration of distributed generation to the low voltage grid is considered.

6.4. Summary

In this chapter, an experimental set-up of designed PV MI is constructed to verify the performance of the system by conducting different case studies. The system is tested under various irradiation levels. The obtained efficiency rates are given in Figure 6.23.

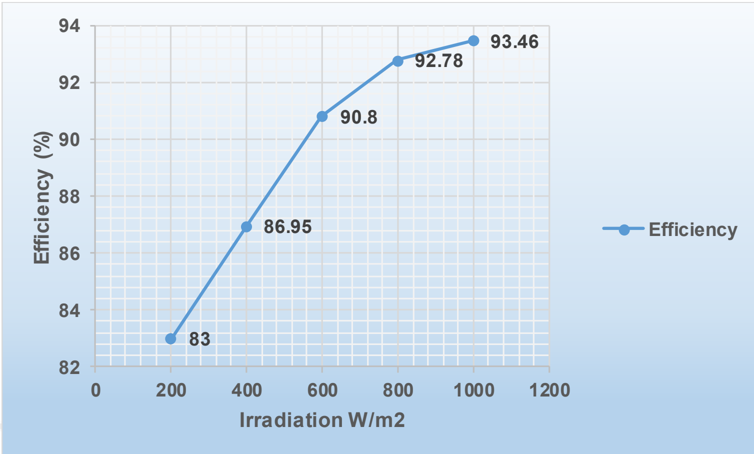

Figure 6.23. Efficiency rates for different irradiation values

It can be concluded that the obtained efficiency rates under different operating conditions are a bit different from the results obtained in simulation studies. The difference between the efficiency level that obtained simulation studies and experimental studies is nearly 3%. It is also worth noting that the output current THD is almost kept under 3.5% with PF greater than 0.9. In view of this, the low input power operating performance of the designed prototype can be increased. The results obviously demonstrate that the system introduces high power quality in the output electrical characteristic. Furthermore, the developed PV MI system has a dynamic grid support capability feature, which is confirmed by ensuring the desired reactive power demand as shown in section 6.3.3.

7. CONCLUSION AND FUTURE WORK

This section presents some concluding remarks, summarizes the main contributions, and discusses future directions of the thesis.

7.1. Concluding Remarks and Discussion

PV technology is demonstrating significant improvement in efficiency and cost reduction. In addition, the governments generate policy to support financial incentives for PV and make the PV systems more attractive in terms of energy investments. Hereby global power generating capacity of installed PV systems growing quickly. It can appear in the market report forecasts via research, PV-based power generation capacity will increase with an accelerated rate. The increased use of distributed generation related to installed PV systems could result in some problems in the utility grid. In order to eliminate these issues, inverters attract great attention, owing to their function as being an operative interface between the PV and the utility grid. Furthermore, inverters having a significant effect on the improvement of efficiency, power quality, and reliability.

This research study focuses to achieve robust output power injection capabilities with lesser design complexity in terms of the controller part and power circuit topology. In addition reduction of cost by achieving some grid requirements without using any hardware modification is determined as one of the primary objectives. Therefore control strategy of developed PV MI mainly covers the solutions of problems related to technical challenges in connecting PV sources to the utility grid and satisfies the MPPT performance criteria such as accuracy, precision, speed, robustness and handling the rapidly changing atmospheric conditions. The increasing integration of PV systems into the utility grid, creates challenges in various technical aspects such as power quality, reliability, and protection. Hence, the grid connection requirements are taken as a guide for the design and performances of the PV inverter. It is possible to foresee expanded penetration of grid-connected PV systems in low voltage grids, so dynamic grid support features might be required also for PV MIs in the future. Moreover, the rate of the injected current harmonics arouses potential problems for the low voltage utility grid. In addition, the controller of the MI should cope with the frequency fluctuations, and voltage flickers due to power fluctuations from PV in order to maintain the grid's stability.

In this thesis, a rigorous model of the two-stage grid-connected PV MI system with a novel MPPT method, which is not available in today's PV MI market, is developed and presented in detail. A 250 W experimental prototype is also implemented. The design stages of the proposed system and utilized controller structure are meticulously highlighted. The feasibility of the proposed PV MI system is analyzed for a variety of load conditions. It is clearly confirmed that the presented PV MI system achieves promising results even in low power operating conditions with regard to weighted efficiency and output current THD.

The comprehensive power circuit design approach is presented for the PV MI prototype in this thesis work. According to the design specifications of the prototype system, the design of PV MI is performed with using the theoretical calculations and the simulation studies accomplished in PSCAD/EMTDC & MATLAB. A control system including DSP (TMS320F28335) based MCU controller circuit, measurement circuit, a gate driver circuit, and analog protection are also designed for the MI prototype in the scope of this thesis work. In the design stages of the control system, the selection of DSP based MCU, the design of measurement and gate driver circuits and the PCB design of the control system are performed. The prototype of PV MI is completed with the power circuit and the control system implementation with the embedded software development studies.

The controller performance of the MI enhanced to provide better system reliability and promote overall efficiency. In order to realize these goals, a novel MPPT method is developed to obtain maximum power from the PV modules under both partially shading conditions and rapidly changing atmospheric conditions. A detailed benchmark study is realized between the proposed and existing MPPT methods in terms of the control variable, PV array dependency, convergence speed, complexity level, analog or digital, periodic tuning and financial outgoings. A mathematical model, which provides a maximum operating point of the PV module, is derived by using GEP. The symbolic regression analysis is performed to find the best proper mathematical function. The modeled system has been examined with conventional MPPT techniques and proposed MPPT technique under different atmospheric conditions. In order to evaluate the robustness of the proposed MPPT method the system is tested in terms of overshoot, convergence speed, tracking accuracy, and the number of oscillations. Simulation results in different cases demonstrate that a considerable enhancement of convergence speed, tracking accuracy, and dynamic response can be accomplished by using the developed model. The proposed technique reaches very quickly to the operating point under rapidly changing weather conditions. The complexity level of the control algorithm is also significantly reduced.

The dynamic grid support and anti-islanding detection capabilities are provided through the improved controller structure without the use of any extra hardware to fulfill grid codes. The presented PV MI system is able to inject reactive current during fault transients with an improved hybrid islanding detection algorithm. The dynamic grid support capability of the developed MI system is tested by changing the desired reactive power amount. According to the measured sag/swell rate, the improved inverter topology can provide inductive/capacitive reactive power to the grid during grid faults without the need to reduce the active power. The dynamic grid support capability is ensured to fulfill the grid-connection demands of the PV systems.

The rate of injected harmonics is reduced by incorporating the selective harmonic compensators to the controller. According to the different load conditions injected current harmonic limits are derived and compensated by the harmonic compensators.

Thus, the proposed PV MI system is satisfactorily compatible with grid-connection standards and performance requirements of PV converters. The THD value of the output current is maintained less than 3%, which is within grid codes. In addition, weighted efficiency and peak efficiency of the developed MI is obtained as 93.73% and 96.92%, respectively. Realization of high efficiency over a wide range of operations, which is a challenge of MI configuration, is achieved. The obtained results indicate that the proposed system provides a promising performance even in low and rapidly changing load conditions. This topology provides many advantages such as higher efficiency, increased reliability, and enhanced controller functionality. It can be clearly concluded that the proposed topology can be a considerable alternative to the traditional PV MI systems in terms of increased dynamic performance and efficiency, reduced output current distortion, meeting grid requirements, and reasonable cost.

7.2. Future Work

As future work, the following studies are planned to be performed

- The power circuit of the PV MI will be modified to reduce the size and number of components,
- The experimental prototype will be improved in order to decrease the EMI,
- In order to increase the dynamic response of the PV MI prototype system, different control methods will be applied,
- The switching frequencies for pulse width modulation will be decreased by utilizing improved switching modulation techniques in order to increase the efficiency,
- PCB design of the system will be improved to realize a more compact structure for future applications.

REFERENCES

Adams J., 2001. Flyback Transformer Design For the IRIS40xx Series. URL: https://www.infineon.com/dgdl/an1024.pdf?fileId=5546d462533600a401535591115e0f6d.

Ahmad R., Murtaza A. F., Sher H. A., 2019. Power tracking techniques for efficient operation of photovoltaic array in solar applications – A review. Renew Sustain Energy Rev 101: 82-102.

Ahmed J. and Salam Z., 2015. A critical evaluation on maximum power point tracking methods for partial shading in PV systems. Renew Sustain Energy Rev 47: 933–53.

Ahmed J. and Salam Z., 2015. An improved perturb and observe (P&O) maximum power point tracking (MPPT) algorithm for higher efficiency. Appl. Energy 150: 97–108.

Ahmed ME-S., Orabi M., AbdelRahim O. M., 2013. Two-stage micro-grid inverter wit highvoltage gain for photovoltaic applications. IET Power Electron 6(9): 1812–21.

Akagi H., Watanabe E., Aredes M., (2007) High Voltage Direct Current Transmission : Converters, Systems, and DC Grids. Wiley–IEEE Press.

Arab M., Zegaoui A., Allouache H., Kellal M., Petit P., Aillerie M., 2014. Micro-controlled pulse width modulator inverter for renewable energy generators. Energy Procedia 50: 832–840.

Arshadi S. A., Poorali B., Adib E., Farzanehfard H., 2016. High Step-Up DC-AC Inverter Suitable for AC Module Applications. IEEE Trans Ind Electron 63(2): 832–839.

Arya, Y., 2017. AGC of restructured multi-area multi-source hydrothermal power systems incorporating energy storage units via optimal fractional-order fuzzy PID controller. Neural Computing and Applications. 31(3): 851-872.

Belhachat F., Larbes C., 2019. Comprehensive review on global maximum power point tracking techniques for PV systems subjected to partial shading conditions. Solar Energy 183: 476-500.

Bower W., West R., Dickerson A., 2007. Innovative PV micro-inverter topology eliminates electrolytic capacitors for longer lifetime. IEEE Proceedings of the 4th World Conference Photovolt. Energy Conversion, WCPEC-4, 2; 2038–2041.

Celik A. N., Acikgoz N., 2007. Modelling and experimental verification of the operating current of mono-crystalline photovoltaic modules using four- and five-parameter models. Appl. Energy 84 (1): 1–15.

Çelik Ö, Teke A, Tan A., 2018. Overview of micro-inverters as a challenging technology in photovoltaic applications. Renew Sustain Energy Rev 82: 3191–206.

Çelik Ö., 2015. A Novel Hybrid MPPT Method for Grid Connected Photovoltaic Systems with Partial Shading Conditions." MSc Thesis, Department of Electrical and Electronic Engineering, Çukurova University, Institute of Natural and Applied Sciences, Adana.

Çelik Ö., Teke A., 2017. Hybrid MPPT method for grid connected photovoltaic systems under rapidly changing atmospheric conditions. Electric Power System Research, 152: 194-210.

Cha W-J., Kwon J-M., Kwon B-H., 2016. Highly efficient step-up dc–dc converter for photovoltaic micro-inverter. Sol Energy 135: 14–21.

Chakraborty S., Chattopadhyay S., 2014. Topology variations and design improvements of a single-stage flyback PV microinverter. Apec 3026–33.

Chen L., Amirahmadi A., Zhang Q., Kutkut N., Batarseh I., 2014. Design and implementation of three-phase two-stage grid-connected module integrated converter. IEEE Trans Power Electron 29(8): 3881–92.

Chiu H. J., Lo Y. K., Chuang C. C., Yang C. Y., Cheng S. J., Kuo M. C., Huang Y. M., Jean Y. B., Huang Y. C., 2014. A module-integrated isolated solar micro-inverter without electrolytic capacitors. Int J Circuit Theory Appl 42(6): 572–83.

Chiu H-J., Lo Y-K., Yang C-Y., Cheng S-J., Huang C-M., Chuang C-C., Kuo M-C., Huang Y-M., Jean Y-B., Huang Y-C., 2013. A module-integrated isolated solar microinverter. IEEE Trans Ind Electron 60(2): 781–8.

Choi W. Y., 2013. High-efficiency DC-DC converter with fast dynamic response for low voltage photovoltaic sources. IEEE Trans Power Electron 28(2): 706–16.

Ciobotaru M., Teodorescu R., Blaabjerg F., 2006. A new single-phase PLL structure based on second order generalized integrator. PESC Rec - IEEE Annu Power Electron Spec Conf, 1–6.

Dhimish M., 2019. Assessing MPPT Techniques on Hot-Spotted and Partially Shaded Photovoltaic Modules: Comprehensive Review Based on Experimental Data. IEEE Transactions on Electron Devices, 66(3): 1132-1144.

Edwin F. F., Xiao W., Khadkikar V., 2014. Dynamic modeling and control of interleaved flyback module-integrated converter for PV power applications. IEEE Trans Ind Electron 61(3): 1377–88.

EN 50438, 2007. Requirements for the connection of micro-generators in parallel with public low-voltage distribution networks. European Committee for electro-technical standardization-CENELEC.

Enrique J.M., Andujar J.M., Bohorquez M.A., 2010. A reliable, fast and low cost maximum power point tracker for photovoltaic applications, Sol. Energy 84: 79–89.

Enslin J. H. R., Wolf M., Swiegers W., 1997. Integrated photovoltaic maximum power point tracking converter. IEEE Trans. Ind. Electron. 44 (6): 769–773.

Evran F., 2017. Plug-in repetitive control of single-phase grid-connected inverter for AC module applications. IET Power Electron, 10(1): 47–58.

Fang X., Hu H., Chen F., Somani U., Auadisian E., Shen J., Batarseh I., 2013. Efficiency oriented optimal design of the LLC resonant converter based on peak gain placement. IEEE Trans Power Electron 28(5): 2285–96.

Fang Y., Ma X., 2010. A novel PV microinverter with coupled inductors and double-boost topology. IEEE Trans Power Electron 25(12): 3139–47.

Ferreira, C., 2001. Gene Expression Programming: A new adaptive algorithm for solving problems. Complex Systems, 13(2): 87-129.

Foster R., Ghasseni M., Cota A., 2010. Solar Energy Renewable Energy and the Environment. CRC Press. ISBN: 978-1-4200-7566-3

Fraunhofer, 2019. Fraunhofer Institute "Photovoltaics Report". URL: https://www.ise.fraunhofer.de/content/dam/ise/de/documents/publications/studies/Photovoltaics-Report.pdf.

Gao M., Chen M., Zhang C., Qian Z., 2014. Analysis and implementation of an improved flyback inverter for photovoltaic AC module applications. IEEE Trans Power Electron 29(7): 3428–44.

George J., Shafeeq M., 2014. Continuous operation of micro-inverter for constant supply in grid connected and off grid operation. 2014 International Conference on Computation of Power, Energy, Information and Communication (ICCPEIC), Chennai, 224-228.

Harb S., Balog R. S., 2013. Reliability of candidate photovoltaic topologies — A usage model approach. IEEE Trans Power Electron 28(6): 3019–27.

Harb S., Kedia M., Zhang H., Balog R. S., 2013. Microinverter and string inverter grid connected photovoltaic system - A comprehensive study, Conference Rec. IEEE Photovolt. Spec. Conference; 2885–2890.

Hasan R, Mekhilef S, Seyedmahmoudian M, Horan B., 2017. Grid-connected isolated PV microinverters: A review. Renew Sustain Energy Rev 67: 1065–80.

Hasan R., Mekhilef S., 2017. Highly efficient flyback microinverter for grid-connected rooftop PV system. Sol Energy 146: 511–22.

Hassaine L, Olias E, Quintero J, Salas V., 2014. Overview of power inverter topologies and control structures for grid connected photovoltaic systems. Renew Sustain Energy Rev 30: 796–807.

Hu H., Harb S., Fang X., Zhang D., Zhang Q., Shen Z. J., Batarseh I., 2012. A three-port flyback for PV microinverter applications with power pulsation decoupling capability. IEEE Trans Power Electron 27(9): 3953–3964.

Hu H., Harb S., Kutkut N. H., Shen Z. J., Batarseh I., 2013. A single-stage microinverter without using eletrolytic capacitors. IEEE Trans Power Electron 28(6): 2677–87.

Hu H., Harb S., Kutkut N., Batarseh I., Shen Z. J., 2010. Power decoupling techniques for micro-inverters in PV systems-A review. IEEE Energy Convers. Congr. Expo. ECCE, 3235–3240.

Hu H., Harb S., Kutkut N., Batarseh I., Shen Z. J., 2013. A review of power decoupling techniques for microinverters with three different decoupling capacitor locations in PV systems. IEEE Trans Power Electron 28(6): 2711–26.

Hu H., Zhang Q., Fang X., Shen Z. J., Batarseh I., 2011. A single stage micro-inverter based on a three-port flyback with power decoupling capability. IEEE Energy Convers. Congr. Expo. Energy Convers. Innov. a Clean Energy Futur. ECCE, 1411–1416.

Hurley W. G. and Wölfle W. H., 2013. Transformers and Inductors for Power Electronics Theory, Design and Applications. Wiley, ISBN: 978-1-119-95057-8.

IEA, Renewables 2019. IEA's Renewables 2019 market report. URL: https://www.iea.org/renewables2019/.

IEC 61000-3-2, 2009. Electromagnetic compatibility (EMC)- Part 3-2: Limits - Limits for harmonic current emissions (equipment input current ≤ 16A per phase). International Electro-technical Commission-IEC.

IEC 61000-3-3, 2013. Electromagnetic compatibility (EMC) - Part 3-3: Limits - Limitation of voltage changes, voltage fluctuations and flicker in public low voltage supply systems, for equipment with rated current ≤ 16 A per phase and not subject to conditional connection. International Electro-technical Commission-IEC.

IEC 61000-6-1, 2016. Electromagnetic compatibility (EMC) - Part 6-1: Generic standards -Immunity standard for residential, commercial and light-industrial environments. International Electro-technical Commission-IEC..

IEC 61000-6-2, 2019. Electromagnetic compatibility (EMC). Generic standards. Immunity standard for industrial environments. International Electro-technical Commission-IEC.

IEC 61000-6-3, 2006. Electromagnetic compatibility (EMC) - Part 6-3: Generic standards - Emission standard for residential, commercial and light-industrial environments. International Electro-technical Commission-IEC.

IEC 61000-6-4, 2018. Electromagnetic compatibility (EMC) – Part 6-4: Generic standards – Emission standard for industrial environments. International Electro-technical Commission-IEC.

IEC 61727, 2004. Photovoltaic (PV) systems - characteristics of the utility interface. International Electro-technical Commission-IEC.

IEC 62109-1, 2010. Safety of power converters for use in photovoltaic power systems - Part 1: General requirements. International Electro-technical Commission-IEC.

IEC 62109-2, 2011. Safety of power converters for use in photovoltaic power systems - Part 2: Particular requirements for inverters. International Electro-technical Commission-IEC.

IEC 62116, 2014. Utility-interconnected photovoltaic inverters - Test procedure of islanding prevention measures. International Electro-technical Commission-IEC.

IEEE 1547-2018, 2018. Standard for Interconnection and Interoperability of Distributed Energy Resources with Associated Electric Power Systems Interfaces. IEEE.

Islam M., Mekhilef S., Hasan M., 2015. Single phase transformerless inverter topologies for grid-tied photovoltaic system: a review. Renew Sustain Energy Rev 45: 69–86.

Jiang S., Cao D., Li Y., Peng F. Z., 2012. Grid-connected boost-half-bridge photovoltaic microinverter system using repetitive current control and maximum power point tracking. IEEE Trans Power Electron 27(11):4711–4722.

Kan J., Wu Y., Tang Y., Xie S., 2019. Flexible topology converter used in photovoltaic micro-inverter for higher weighted-efficiency. IET Power Electronics, 12(9): 2361-2371.

Kavurucu S., 2014. Design and Implementation of a 200 W Microinverter for Grid Connected Photovoltaic Energy Conversion System. MSc Thesis, Electrical and Electronics Engineering Department, Middle East Technical University, Graduate School of Natural and Applied Sciences, Ankara, 1-183.

Kazimierczuk M. K., 2008. Pulse-width Modulated DC – DC Power Converters. Wiley. ISBN: 9780470694657

Khan A., Ben-brahim L., Gastli A., Benammar M., 2017. Review and simulation of leakage current in transformerless microinverters for PV applications. Renew Sustain Energy Rev 74: 1240–56.

Khosrogorji S., Ahmadian M., Torkaman H., Soori S., 2016. Multi-input DC / DC converters in connection with distributed generation units – A review. Renew Sustain Energy Rev 66: 360–79.

Kim Y. H., Jang J. W., Shin S. C., Won C. Y., 2014. Weighted-efficiency enhancement control for a photovoltaic AC module interleaved flyback inverter using a synchronous rectifier. IEEE Trans Power Electron 29(12): 6481–6493.

Kim Y. H., Ji Y. H., Kim J. G., Jung Y. C., Won C. Y., 2013. A new control strategy for improving weighted efficiency in photovoltaic AC module-type interleaved flyback inverters. IEEE Trans Power Electron 28(6): 2688–99.

Kjaer S. B., Pedersen J. K., Blaabjerg F., 2002. Power inverter topologies for photovoltaic modules-a review. Conference Rec IEEE Ind. Appl. Conference 37th IAS Annu. Meet. (Cat. No.02CH37344), 2, 91; 782–788.

Kjaer S. B., Pedersen J. K., Blaabjerg F., 2005. A review of single-phase grid-connected inverters for photovoltaic modules. IEEE Trans Ind Appl 41: 1292–306.

Kwak R., Lee J. H., Lee K. B., 2016. Active frequency drift method for islanding detection applied to micro-inverter with uncontrollable reactive power. J Power Electron 16(5): 1918–27.

Lai C. M., 2014. A single-stage grid-connected PV micro-inverter based on interleaved flyback converter topology. Proceedings – 2014 International Symp. Comput. Consum. Control. IS3C 187–190.

Lai C-M., Lee D., Cheng Y-H., 2016. An isolated AC module for photovoltaic energy conversion. Int J Green Energy 13(14):1460–6.

Lee S., Cha W., Kwon J., Kwon B., 2016. Control strategy of flyback microinverter with hybrid mode for PV AC modules. IEEE Trans Ind Electron 63(2): 995-1002.

Liao C., Lin W., Chen Y., C. Chou, 2017. A PV Micro-inverter With PV Current Decoupling Strategy. IEEE Transactions on Power Electronics,32(8),. 6544-6557,. 2017.

Liu L., Meng X., Liu C., 2016. A review of maximum power point tracking methods of PV power system at uniform and partial shading. Renew Sustain Energy Rev 53: 1500–7.

Mammano R., 1995. Switching power supply topology voltage mode vs. current mode. Unitrode Prod Appl Handb 96:587–589.

Mazumder S. K. and Mehrnami S., 2012. A low-device-count single-stage direct-power conversion solar microinverter for microgrid. Proceedings − 2012 3rd IEEE International Symp. Power Electron. Distrib. Gener. Syst. PEDG 3: 725–730.

Meneses D., Garcia O., Alou P., Oliver J. A., Cobos J. A., 2015. Grid-connected forward microinverter with primary-parallel secondary-series transformer. IEEE Trans Power Electron 30(9): 4819–4830.

Mirza A. F., Ling Q., Javed M. Y., Mansoor M., 2019. Novel MPPT techniques for photovoltaic systems under uniform irradiance and Partial shading. Solar Energy 184: 628-648.

Morais J. C. d. S. de, Morais J. L. d. S. de, Gules R., 2019. Photovoltaic AC Module Based on a Cuk Converter With a Switched-Inductor Structure. IEEE Transactions on Industrial Electronics, 66(5): 3881-3890.

Motahhir S., El Hammoumi A. El Ghzizal A., 2019. The most used MPPT algorithms: Review and the suitable low-cost embedded board for each algorithm. Journal of Cleaner Production (In press)

Nanakos A. C., Christidis G. C., Member S., Tatakis E. C., 2015. Weighted Efficiency Optimization of Flyback Microinverter Under Improved Boundary Conduction Mode (i-BCM). IEEE Transactions on Power Electronics, 30(10): 5548-5564.

Nanou S., Papathanassiou S., 2014. Modeling of a PV System with Grid Code Compatibility. Electric Power Systems Research, 116: 301-310.

Nayanasiri D. R., Vilathgamuwa D. M., Maskell D. L., 2013. Half-wave cycloconverter-based photovoltaic microinverter topology with phase-shift power modulation. IEEE Trans Power Electron 28(6): 2700–2710.

Nema, R. K., Bhatnagar, P., 2013. Maximum power point tracking control techniques:state of-the-art in photovoltaic applications. Renew. Sustain. Energy Rev. 23: 224–241.

Neshaastegaran P., Karshenas H. R., 2013. Investigation of single-stage flyback inverter under different operating modes. PEDSTC 2013 - 4th Annu Int Power Electron Drive Syst Technol Conf, 288–293.

Noguchi T., Togashi S., Nakamoto R., 2002. Short-current pulse-basedmaximum-power-point tracking method for multiple photovoltaic-and-converter module system. IEEE Trans. Ind. Electron. 49 (1): 217–223.

Oldenkamp H., S.W.H. de Haan, I.J. de Jong, Baltus C. W. A., Frumau C. F. A., Verhoeven S. A. M., 1995. Competitive implementation of multi-kilowatts grid connected PV-systems with OKE4 AC modules. 13th European Photovoltaic Solar Energy Conference, Nice, France. 23-27 October. URL: http://www.oke-services.nl/downloads/199510_ok4_paper_epvsec13.pdf

Patidar K., Umarikar A. C., 2015. High step-up converters based on quadratic boost converter for micro-inverter. Electr Power Syst Res 119: 168–77.

Petreuş D., Daraban S., Ciocan I., Patarau T., Morel C., Machmoum M., 2013. Low cost single stage micro-inverter with MPPT for grid connected applications. Sol Energy 92: 241–255.

Pragallapati N., Agarwal V., 2014. Single phase solar PV module integrated flyback based micro-inverter with novel active power decoupling. Proceedings of the 7th IET International Conference Power Electron. Mach. Drives, PEMD 1; 1–6.

Pragallapati N., Member S., Lodh T., Agarwal V., 2015. Parallel-Input Series-Output Interleaved Flyback based Solar PV Module Integrated Micro-Inverter. International Conference on Renewable Energy Research and Applications (ICRERA) 716-720.

Rambo C. E. B., Dos Reis F. B., Pedrollo G. R., Dos, Reis F. S., 2014. Improving performance of the P&O MPPT using derivative of photovoltaic panel voltage. Proceedings, IECON 2014 – 40th Annu. Conference IEEE Ind. Electron. Soc; 5546–5551.

Reisi A. R., Moradi M. H., Jamasb S., 2013. Classification and comparison of maximumpower point tracking techniques for photovoltaic system: a review. Renew.Sustain. Energy Rev., 19: 433–443.

REN, (2019). "Renewables 2019 Global Status Report." URL: https://www.ren21.net/gsr-2019

Roy J., Xia Y., Ayyanar R., 2019. High Step-Up Transformerless Inverter for AC Module Applications With Active Power Decoupling. IEEE Transactions on Industrial Electronics, 66(5): 3891-3901.

Safari A., Mekhilef S., 2011. Simulation and hardware implementation of incremental conductance MPPT with direct control method using Cuk converter. IEEE Trans. Ind. Electron. 58 (4): 1154–1161.

Sahu P. K., Shaw P., Maity S., 2015. Modeling and Control of Grid-Connected DC/AC Converters for Single-Phase Micro-inverter Application. India Conference (INDICON) Annual IEEE; 1–6.

Salam Z., Ahmed J., Merugu B. S., (2013). “The application of soft computing methods for MPPT of PV system: A technological and status review.” Appl Energy 107: 135–148.

Salameh Z., Dagher F., Lynch W., 1991. Step-down maximum power point tracker for photovoltaic systems. Sol. Energy 46: 279–282.

Salas V., Olias E., Barrado A., Lazaro A., 2006. Review of the maximum power point tracking algorithms for stand-alone photovoltaic systems. Sol. Energy Mater. Sol. Cells 90: 1555–1578.

Schimpf F., Norum L. E., 2008. Grid connected converters for photovoltaic, state of the art, Ideas for improvement of transformerless Inverters. Proc Nord Work Power Ind Electron 6.

Sher H. A., Addoweesh K. E., 2012. Micro-inverters - Promising solutions in solar photovoltaics. Energy Sustain Dev 16: 389–400.

Shimizu T, Wada K, Nakamura N., 2006. Flyback-type single-phase utility interactive inverter with power pulsation decoupling on the DC input for an

AC photovoltaic module system. IEEE Trans Power Electron 21: 1264–1272.

Subudhi B., Pradhan R., 2013. A comparative study on maximum power point tracking techniques for photovoltaic power systems. IEEE Trans. Sustain. Energy 4 (1): 89–98.

Sukesh N., Pahlevaninezhad M., Jain P. K., 2014. Analysis and implementation of a single stage flyback PV microinverter with soft switching. IEEE Trans Ind Electron 61(4): 1819–33.

Surapaneni R. K., Rathore A. K., 2015. A single-stage CCM zeta Microinverter for solar photovoltaic AC module. IEEE J Emerg Sel Top Power Electron 2015;3(4):892–900.

Surapaneni R. K., Yelaverthi D. B., Rathore A. K., 2016. Cycloconverter-based double-ended Microinverter topologies for solar photovoltaic AC module. IEEE J Emerg Sel Top Power Electron 4(4): 1354–61.

Teodorescu, R., Blaabjerg F., Liserre, M., Loh P. C., 2006. Proportional-resonant controllers and filters for grid-connected voltage source converters. IEEE Proc.-Eletr. Power Appl., 153(5): 750-762.

Teodorescu, R., Liserre, M., Rodriguez, P., 2011. Grid Converters for Photovoltaic and Wind Power Systems. Wiley-IEEE Press.

Texas Instruments, 2015. TMS320F28335 Delfino Microcontroller. URL: http://www.ti.com/product/tms320f28335.

Texas Instruments, 2017. UCC21520, UCC21520A 4-A, 6-A, 5.7-kVRMS Isolated Dual-Channel Gate Driver. URL: http://www.ti.com/lit/ds/symlink/ucc21520.pdf.

Texas Instruments, 2018. AMC1301 Precision, ±250-mV Input, 3-µs Delay, Reinforced Isolated Amplifier. URL: http://www.ti.com/lit/ds/symlink/amc1301.pdf.

Texas Instruments, 2018. AMC1311x High-Impedance, 2-V Input, Reinforced Isolated Amplifiers. URL: http://www.ti.com/lit/ds/symlink/amc1311.pdf.

Texas Instruments, 2018. High-Bandwidth Phase Current and DC-Link Voltage Sensing Reference Design for Three-Phase Inverters. URL: http://www.ti.com/lit/ug/tidudk0a/tidudk0a.pdf.

Texas Instruments, 2019. Voltage Source Inverter Reference Design. URL: http://www.ti.com/lit/ug/tiduay6d/tiduay6d.pdf

Trujillo C. L., Santamaría F., Gaona E. E., 2016. Modeling and testing of two-stage grid-connected photovoltaic micro-inverters. Renewable Energy 99: 533-542.

Trujillo C. L., Velasco D., Figueres E., Garcer G., Ortega R., 2011. Modeling and control of a push-pull converter for photovoltaic microinverters operating in island mode. Appl Energy 88(8):2824–2834.

Trujillo C. L., Velasco D., Figueres E., Garcera G., 2010. Analysis of active islanding detection methods for grid-connected microinverters for renewable energy processing. Appl Energy 87(11): 3591–3605.

Trujillo C. L., Velasco D., Figueres E., Garcera G., Ortega R., 2011. Modeling and control of a push-pull converter for photovoltaic microinverters operating in island mode. Appl Energy 88(8): 2824–2834.

Trujillo Rodriguez C., La Fuente De Velasco D., Garcera G., Figueres E., Moreno J.A.G., 2013. Reconfigurable control scheme for a PV microinverter working in both grid-connected and Island modes. IEEE Trans Ind Electron 60(4): 1582–95.

Tsai M. T., Chu C. L., Lin J. Y., 2013. Single-stage controlled PV micro-inverter with symmetrical phase-shift modulation. Proc. Int. Conf. Power Electron. Drive Syst.; 887–892.

Verma D., Nema S., Shandilya A. M., Dash S. K., 2016. Maximum power point tracking (MPPT) techniques: recapitulation in solar photovoltaic systems. Renew Sustain Energy Rev 54: 1018–34.

Yang Y., Blaabjerg F., 2015. Overview of Single-phase Grid connected Photovoltaic Systems. Electric Power Components and Systems, 43:12, 1352-1363.

Yang Y., Kim K. A., Blaabjerg F., Sangwongwanich A., 2019. Advances in Grid-Connected Photovoltaic Power Conversion Systems. Elsevier.

Yang Y., Wang H., Blaabjerg F., 2014 Reactive power injection strategies for single-phase photovoltaic systems considering grid requirements. IEEE Trans Ind Appl 50: 4065–76.

Yang, Y., Blaabjerg, B., Zou, Z., 2013. Benchmarking of Grid Fault odes in Single-Phase Grid-Connected Photovoltaic Systems. IEEE Trans on Indus Appl, 49(5): 2167-2176.

Zeb K., Uddin W., Khan M. A., Ali Z., Ali M. U., Christofides N., Kim H.J., 2015. A comprehensive review on inverter topologies and control strategies for grid connected photovoltaic system. Renew Sustain Energy Rev 94: 1120–1141.

Zengin S., Deveci F., Boztepe M., 2012. Decoupling capacitor selection in DCM flyback PV microinverters considering harmonic distortion. IEEE Trans Power Electron 28(2) :816–25.

Zhang Z., Chen M., Gao M., Mo Q., Qian Z., 2011. An optimal control method for grid connected photovoltaic micro-inverter to improve the efficiency at light-load condition. IEEE Energy Convers. Congr. Expo. Energy Convers. Innov. a Clean Energy Futur. ECCE 2011, Proceedings; 219–224.

Zhang Z., He X. F., Liu Y. F., 2013. An optimal control method for photovoltaic grid-tied interleaved flyback microinverters to achieve high efficiency in wide load range. IEEE Trans Power Electron 28(11): 5074–5087.

Zhong, J., Feng, L., Ong, Y. S., 2017. Gene Expression Programming: A Survey. IEEE Computational Intelligence Magazine, 12(3): 54-72.

CURRICULUM VITAE

Özgür ÇELİK was born in Ankara, Turkey in 1990. He graduated from Sincan Süleyman Demirel Anatolian High School in 2008. He received his BSc degree in Electrical and Electronics Engineering from Çukurova University in 2013. After graduation, he has specialized in transmission and distribution systems in the private sector for 1-year. In 2015, he received his M.Sc. degree in Electrical and Electronics Engineering at Çukurova University. He has been working as a research assistant in the Electrical and Electronic Engineering Department of the Adana Alparslan Türkeş Science and Technology University since 2014.

His research interests include renewable energy systems, generation, transmission, and distribution of electrical energy, power electronic converters, and energy efficiency applications.

He is a member of the Institute of Electrical and Electronics Engineer (IEEE) and the Turkish Chamber of Electrical Engineers (UCTEA).